Quantifying Land Surface Temperature Changes Associated with Land Cover Changes

GEO 511 Master's Thesis

Author
Lou Lerren Curacha
22-747-786

Supervised by
Dr. Hendrik Wulf
Dr. Jennifer Susan Adams

Faculty representative
Prof. Dr. Livia Piermattei

30.01.2025
Department of Geography, University of Zurich

Abstract

Significant transformations are being observed globally across ecosystems driven by natural processes and human activities. Using moderate resolution imaging spectroradiometer (MODIS) land surface temperature (LST) product: MOD21A1 and European Space Agency Climate Change Initiative (ESA CCI) land cover (LC) product, this study provides a comprehensive analysis of global land cover change (LCC) since 2000 and their impacts on LST. Using a systematic approach, the overall mean and its annual LST variations were quantified for 484 LCC transitions derived from the 22 x 22 LC classifications, revealing distinct cooling and warming patterns. Transitions that increased vegetation cover such as bare areas to grasslands, and bare areas to sparse vegetation consistently resulted in cooling effects, with temperature decreases up to $-0.45°C$ at a rate of $-0.030°C/year$ and $-0.20°C$ at a rate of $-0.017°C/year$ respectively. Conversely, warming effects were linked to deforestation, urbanization, and water loss. Transitions such as flooded vegetation to needleleaf forests ($+0.84°C$) at a rate of $+0.076°C/year$ and cropland to urban areas ($+0.39°C$) at a rate of $+0.019°C/year$ highlighted the critical role of land use in amplifying surface temperatures. Regional analysis revealed cooling trends in northern areas, such as Canada and Greenland, driven by vegetation recovery, while warming was prominent in tundra regions, where forest loss and snow cover reduction amplified surface heating. The largest global transitions included the conversion of bare areas to sparse vegetation, indicating ecological recovery in degraded regions, and the shift from sparse vegetation to grasslands, highlighting changes within the "Grass & Shrubs" classification, which experienced the highest levels of disturbance. Although many findings aligned with established patterns, anomalies such as unexpected cooling in evergreen needleleaf forest transitions and warming in tundra regions involving deciduous needleleaf forests underscored the complexities of LCC and their localized impacts on LST. The anomalies emphasize the need for further investigation into factors such as neighboring pixel effects, data accuracy, and climatic influences. By improving data accuracy and alignment, addressing resolution mismatches, and adopting regionalized analysis, future research can improve the understanding of the LCC-LST dynamics. Despite the challenges, these findings highlight the importance of sustainable land management practices, including reforestation and urban greening programs to mitigate the adverse effects of LCC on global and regional LST.

Contents

Abbreviations

AOI	Area of Interest
CCI	Climate Change Initiative
CGLS	Copernicus Global Land Service
ECV	Essential Climate Variables
EROS	Earth Resources Observation and Science
ESA	European Space Agency
ESA CCI	European Space Agency Climate Change Initiative
GeoTIFF	Georeferenced Tagged Image File
GEE	Google Earth Engine
IGBP	International Geosphere-Biosphere Programme
LC	Land Cover
LCC	Land Cover Change
LCCS	Land Cover Classification System
LCS	Land Cover Science
LST	Land Surface Temperature
LULC	Land Use Land Cover
MODIS	Moderate Resolution Imaging Spectroradiometer
MBE	Mean Bias Error
NASA	National Aeronautics and Space Administration
NDVI	Normalized Difference Vegetation Index
NOAA	National Oceanic and Atmospheric Administration
OLS	Ordinary Least Squares
RMSD	Root Mean Square Difference
RMSE	Root Mean Square Error
SLC	Scan Line Corrector
TES	Temperature/Emissivity Separation
TIR	Thermal Infrared
UN FAO	United Nations Food and Agriculture Organization
USGS	U.S. Geological Survey

List of Figures

List of Tables

1 Introduction

1.1 Background and motivation

The Earth's surface is a dynamic and interconnected system comprising various types of land cover (LC) such as vegetation, soil, ice, and water, all of which play a vital role in regulating global climate systems and sustaining the ecological balance of the planet (Bechtel, 2015; Nicholson, 2015). The earth's surface influences the global climate by contributing approximately two-thirds of atmospheric warming through the surface of the earth (Nicholson, 2015). The land surface temperature (LST) represents the Earth's surface heat radiating outwards as measured by its radiative temperature which influences the energy balance exchange between the land surface and the atmosphere (Bastiaanssen et al., 1998; Bechtel, 2015; Ma et al., 2020). Land cover changes (LCC) such as deforestation, afforestation, urbanization are known to alter land surface temperatures through evapotranspiration, albedo, and land emissivity, which are key factors in retrieving the LST (Li et al., 2016b; Liu et al., 2020; Peng et al., 2014; Sekertekin and Bonafoni, 2020). A sample LC conversion effect on the LST would be the conversion of forests to cropland or pasture which reduces the precipitation capture on the canopy and soil moisture extraction of root resulting in decreased evaporation and heat transfer from the surface to the atmosphere, causing a rise in near-surface temperature (Betts et al., 2007; Li et al., 2016b). Additionally, another sample study that was conducted in China emphasized the effect of afforestation on the LST cooling through increased evapotranspiration (Peng et al., 2014).

LC changes such as urban expansion, agricultural intensification, deforestation, and natural disasters are just a few examples of processes that modify the Earth's surface, each leaving a distinct thermal footprint detectable through changes in LST (Bokaie et al., 2016; Hashim et al., 2022; Imran et al., 2021; Li et al., 2016b; Peng et al., 2014). The urgency to study these dynamics is amplified by the alarming rise in global temperatures. According to the National Aeronautics and Space Administration (NASA) and National Oceanic and Atmospheric Administration (NOAA), the Earth's average global surface temperature in 2023 set a new record, surpassing previous highs with a record of 1.18 to 1.2 degrees Celsius which was above NOAA's 1850-2023 climate record and NASA's baseline period (1951-1980) respectively (Bardan, 2024; Bateman, 2024). Furthermore, 2023 also exceeded the previous record holder in 2016 by 0.15 degrees Celsius (Bateman, 2024). LST is crucial in controlling most physical, chemical and biological processes of the Earth (Avdan and Jovanovska, 2016; BECKER and LI, 1990). The rise in global land surface temperatures poses a significant threat to the environment, agriculture, water resources, and human health by disrupting natural processes and increasing the need to assess the impacts of climate change (Abdullah-Al-Faisal et al., 2021; Huang et al., 2022; Mentaschi et al., 2022). Understanding and quantifying these LCC is critical to developing effective mitigation and adaptation strategies (Abdullah-Al-Faisal et al., 2021; Mentaschi et al., 2022).

This research is motivated by the need to quantify the impacts of LCC on LST on both a regional and global scale and to identify how specific land transitions influence temperature dynamics. Although prior studies have highlighted localized LCC impacts, there is a pressing need to systematically assess these changes at a broader spatial and temporal scale, enabling the identification of global patterns essential for environmental mitigation strategies.

1.2 Research gaps

Despite extensive research on LCC and its environmental impacts, research gaps still remain in understanding the global scale interactions between LCC and LST. Many existing studies focus on specific regions or ecosystems such as urban heat islands (Clinton and Gong, 2013; Bokaie et al., 2016) or afforestation or deforestation in tropical forests (Peng et al., 2014; Li et al., 2016b), leaving unexplored global patterns. Furthermore, the influence of specific land cover transitions such as water loss, afforestation, or urbanization on LST at a global scale has received limited attention.

This study aims to address key knowledge gaps by providing a comprehensive global scale analysis of how different LCC transitions influence LST patterns. The major research gaps that this study seeks to bridge include limitations in global coverage research, assessment of major LC transitions globally, distinguishing climate driven and LCC driven temperature changes, and integrating long-term LST trends.

Although many regional studies have explored the relationship between LC transitions and LST, few comprehensive global-scale assessments exist that account for the spatial heterogeneity of these interactions. This research fills this gap by systematically analyzing all the LC transitions globally, highlighting spatial patterns of warming and cooling across multiple ecosystems. Furthermore, while previous research has examined specific LC transitions, such as deforestation and urbanization, there is limited research that systematically evaluates the full range of transitions and their influence on LST at a global scale. This study takes a holistic approach, considering multiple types of land cover transitions to understand their diverse thermal impacts.

A fundamental challenge in LST studies is separating LC-driven temperature changes from overarching climate change trends. This research develops a robust comparative framework by analyzing disturbed and undisturbed areas globally, helping to isolate the direct effects of LCC from broader climatic influences. Furthermore, this study overcomes the limitations of studies involving short-term LST changes by analyzing LST trends over two decades (2000–2020), allowing a more consistent temporal analysis to assess long-term trends and their implications for climate change.

By addressing these critical research gaps, this study aims to improve the scientific understanding of the interactions between LCC and LST and to contribute to a more comprehensive framework to assess how LC dynamics affect LST, ultimately supporting more informed climate adaptation and land management strategies.

1.3 Research objectives

This research MSc thesis aims to explore the complex relationship between LCC and LST on a global scale, addressing gaps in understanding how large-scale LC transitions influence surface temperatures. By analyzing LCC and its associated LST thermal impacts, this study aims to achieve the following key objectives:

Quantify dominant land cover transitions: Identify and quantify the major LC transitions occurring globally between 2000 and 2020, emphasizing the most significant drivers of change. This involves measuring the extent of transitions across different LC classes and mapping their global distribution to highlight the most substantial LCC.

Analyze LST variations: Evaluate the overall increase in LST and the mean annual LST variations resulting from LCC by comparing disturbed areas (those undergoing LC transitions) with undisturbed regions (areas without LCC). This approach isolates the direct thermal effects of LCC from external factors such as climate trends, providing a clearer picture of how specific LCC influence surface temperatures.

Identify regions with significant LST impact: Determine the geographic regions that have experienced notable warming or cooling due to LCC. Through spatial analysis, this objective aims to identify areas most affected by specific transitions, providing insight into the regions where LCC have had the greatest thermal impact.

Examine common LC change effects: Investigate how the most frequent LC transitions, such as deforestation, urbanization, and afforestation, influence LST dynamics. This requires analyzing the relationship between the major LC type transitions and their corresponding thermal responses, shedding light on the broader implications of human-induced and natural LC changes.

These objectives should address the following research questions (RQs):

- **RQ1:** Which large-scale LC changes happened globally since 2000?

- **RQ2:** How can we quantify the mean annual LST variations resulting from changes in LC?

- **RQ3:** Which regions around the world experienced significant warming or cooling as a result of LC changes?

- **RQ4:** How do the most common changes in LC affect LST?

By addressing these objectives, this study contributes to a more comprehensive understanding of the interplay between LCC and LST, enhance our understanding of the relationship between LCC and LST, offering insights into both localized and global climate dynamics.

2 Data

LST is widely applied in various fields and plays a vital role in the surface energy budget and the water cycle processes on regional and global scales (Duan et al., 2014; Duan et al., 2017; Duan et al., 2021; Li et al., 2013; Sobrino et al., 2016; Wang et al., 2020; Zhao et al., 2019). The analysis of temporal LST data for environmental and climate change monitoring relies on the multi-temporal availability of time series data which is often a challenge especially in maintaining the temporal consistency of thermal data (Duguay-Tetzlaff et al., 2015; Hulley and Hook, 2011; Gök et al., 2024; Kuenzer and Dech, 2013). The LC dataset used in the study is the European Space Agency Climate Change Initiative (ESA CCI) LC and the moderate resolution imaging spectroradiometer (MODIS) LST, where both are temporally consistent (Hulley and Hook, 2011; Mousivand and Arsanjani, 2019) and where the LST trends are recently made available globally (Gök et al., 2024; Sobrino et al., 2020). In addition, over the last few decades, the estimation of LST from satellite thermal infrared (TIR) data has advanced and many algorithms were developed in order to retrieve the LST (Li et al., 2013).

The thermal products taken from satellite have proven to be a reliable tool for monitoring LST at a local, regional, and global scale, with about 99% of the studies using TIR, 76% being the use of MODIS terra/aqua observations (Ahmed et al., 2023; Ghaderpour et al., 2024). There are numerous satellite sensors that can collect LST data; however, cloud cover is still an issue that can result in significant data gaps (Ahmed et al., 2023; Ghaderpour et al., 2024; Yu et al., 2022; Pan et al., 2024). MODIS with its terra and aqua satellites can provide day and night LST measurements with an accuracy of up to 1 K under clear-sky conditions, with both satellites operating at a sun-synchronous orbit and operating at an altitude of about 705 km (Yu et al., 2022; Wan et al., 2002; Ghaderpour et al., 2024; Hulley and Hook, 2017; Wang et al., 2020). On the other hand, land change science (LCS) is an emerging interdisciplinary field that focuses on studying global environmental changes and sustainability through analysis of the land use land cover (LULC) dynamics and their interaction with the human-environmental processes across spatial and temporal scales (Mousivand and Arsanjani, 2019; Rindfuss et al., 2004; Turner et al., 2007). The European Space Agency (ESA) launched the Climate Change Initiative (CCI) program in 2009 to deliver high-quality satellite-derived products for essential climate variables (ECV), including LC (Li et al., 2016a; ESA—European Space Agency, 2014; Defourny P. et al., 2017; Defourny, 2019). As part of this effort, the ESA CCI LC project provides stable and comprehensive LC datasets for the climate modeling community with a spatial resolution of 300 m and a continuous temporal coverage of 24 years, covering a complete range of LC types (Mousivand and Arsanjani, 2019; Liu et al., 2018; Jiang and Yu, 2019; Li et al., 2016a; ESA—European Space Agency, 2014; Defourny P. et al., 2017; Defourny, 2019). The ESA CCI LC maps have an overall accuracy of 75.6% for the 1992–2015 period, while the 2016–2022 period shows a slightly lower average overall accuracy of 70.77% (std = 0.28), based on 1,344 samples (Copernicus Climate Change Service, 2019. The LC product ESA CCI LC was downloaded directly through their website.

The download of LST datasets were carried out using the Google Earth Engine (GEE) platform, which was released in 2010 as a cloud computing platform with substantial computational capabilities (Amani et al., 2020; Ahmed et al., 2023). The GEE platform is used mainly by the remote sensing community for various applications, including analysis of global geospatial data (Zhao et al., 2021). Furthermore, GEE supports different types of datasets in the catalog such as sentinel, landsat, and MODIS, which were made available since 2015 (Gorelick et al., 2017). These satellite missions and sensors such as the sentinel, landsat, and MODIS have different temporal resolutions and are equipped with different thermal infrared sensors which allow the measurement of the LST. (Barnes et al., 2003; Donlon et al., 2012; Neinavaz et al., 2021; Wulder et al., 2019; Ghaderpour et al., 2024). Finally, post-processing of the datasets was done in Python (version 3.11.15).

The timeline and datasets used in the study are:

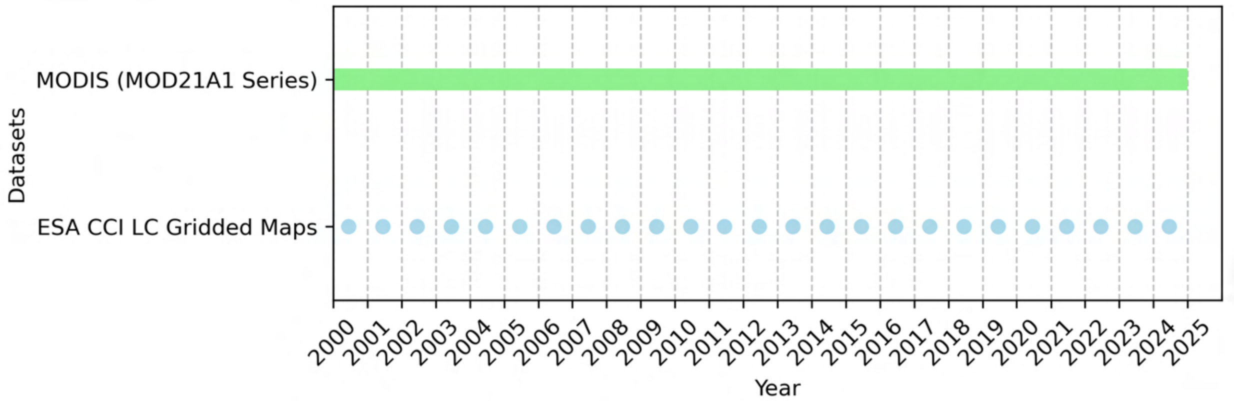

Figure 2.1: Data availability timeline histogram of MODIS MOD21A1 LST and Copernicus ESA CCI LC gridded maps starting in 2000. This histogram was created by the author to represent the data availability timeline of MODIS MOD21A1 LST (represented by green, continuous) and Copernicus ESA CCI LC (represented by blue, yearly – circles) starting in 2000. Data source: Hulley and Hook, 2017; ESA—European Space Agency, 2014.

2.1 Land surface temperature: MODIS (MOD21A1 series)

Table 2.1: MOD21A1 land surface temperature product data attributes. Adapted from source: Hulley and Hook, 2017.

Name	Start	End	Resolution	Frequency
MOD21A1	February 02, 2000	Present	1,000 meters	16 Days

MODIS is operating on the terra and aqua satellites that captures data across 36 high-resolution spectral bands ranging from (0.415 to 14.235 μm), with spatial resolutions of 250 m (2 bands), 500 m (5 bands), and 1000 m (29 bands) and are designed to operate in complementary orbits, allowing observations in the late morning and early afternoon to ensure near-complete global coverage within a single day, which is ideal for climate and global change research (Barnes et al., 1998; Salomonson et al., 2001; Savtchenko et al., 2004; Hulley and Hook, 2017; Ghaderpour et al., 2024; Zhao et al., 2020; Yu et al., 2022; Zhang et al., 2003; Wan et al., 2002). Furthermore, MODIS-derived products such as MOD21 and MYD21 have demonstrated impressive accuracy in LST measurements. According to a study by Xu et al. (2023), the MOD21 and MYD21 products had the lowest root mean square error (RMSE) among all skin temperature products, with an RMSE of 3.35 K (Xu et al., 2023. However, these products also exhibited a relatively high percentage of missing values (48.4%) in certain regions, such as the Heihe River Basin, indicating some limitations in the completeness of the data (Xu et al., 2023. In addition, Yao et al. (2020) found that the RMSE of the MYD21 product ranged from 0.5–1.5°C over barren land and from 0.9–1.3°C over water and vegetated surfaces, further demonstrating its high accuracy across diverse surface types (Yao et al., 2020). The variability in performance across land types reflects the instrument's ability to adapt to a wide range of surface conditions, making it suitable for detailed and accurate LST assessments.

The MODIS terra and aqua satellites provide daytime and nighttime LST products (Savtchenko et al., 2004; Hulley and Hook, 2017; Ghaderpour et al., 2024) that have been widely utilized in a wide range of studies. These include estimating air temperatures (Sun et al., 2014; Marzban et al., 2018), analyzing surface energy balance (Hain and Anderson, 2017; Guzinski et al., 2013), developing drought monitoring indices (Sun et al., 2013), investigating urban heating (Nichol, 2005; Clinton and Gong, 2013; Abou Samra, 2023), and exploring the relationship between LC and LST trends (Gök et al., 2024; Shawky et al., 2023; Ghaderpour et al., 2024). The versatility of MODIS products has solidified their role as essential datasets to address environmental and climatic challenges.

There are four MODIS LST products used in the study: MODIS Terra Day (MOD21A1D), MODIS Terra Night (MOD21A1N), MODIS Aqua Day (MYD21A1D), MODIS Aqua Night (MYD21A1N) (Savtchenko et al., 2004; Hulley and Hook, 2017; Ghaderpour et al., 2024). In order to utilize the MODIS terra and aqua, day and night LST Products, the researcher has used a harmonic model to estimate parameters with fewer coefficients and clear observations while effectively mitigating the effects of short-term data fluctuations and inherent noise such as clouds, cloud shadow, snow cover and other image artifacts (Zhu and Woodcock, 2014). By using the MODIS LST products, the harmonic model enables the integration of temporal observations to capture an accurate global annual mean LST.

2.2 Land cover: ESA CCI LC product

Table 2.2: ESA CCI LC gridded maps product information data attributes. Adapted from source: ESA—European Space Agency, 2014.

Name	Start	End	Resolution	Frequency	Classes
CCCS LCGRID	1992	Present	300 meters	Yearly	22

	Class 10	Cropland rainfed	Agriculture
	Class 20	Cropland irrigated or post-flooding	
	Class 30	Mosaic cropland (>50%) / natural vegetation (tree, shrub, herbaceous cover) (<50%)	
	Class 40	Mosaic natural vegetation (tree, shrub, herbaceous cover) (>50%) / cropland (<50%)	
	Class 50	Tree cover, broadleaved, evergreen, closed to open (>15%)	Forest
	Class 60	Tree cover, broadleaved, deciduous, closed to open (>15%)	
	Class 70	Tree cover, needleleaved, evergreen, closed to open (>15%)	
	Class 80	Tree cover, needleleaved, deciduous, closed to open (>15%)	
	Class 90	Tree cover, mixed leaf type (broadleaved and needleleaved)	
	Class 100	Mosaic tree and shrub (>50%) / herbaceous cover (<50%)	
	Class 110	Mosaic herbaceous cover (>50%) / tree and shrub (<50%)	Grass & Shrubs
	Class 120	Shrubland	
	Class 130	Grassland	
	Class 140	Lichens and mosses	
	Class 150	Sparse vegetation (tree, shrub, herbaceous cover) (<15%)	
	Class 160	Tree cover, flooded, fresh or brackish water	Flooded Vegetation
	Class 170	Tree cover, flooded, saline water	
	Class 180	Shrub or herbaceous cover, flooded, fresh/saline/brackish water	
	Class 190	Urban areas	Bare & Built-up
	Class 200	Bare areas	
	Class 210	Water bodies	Water & Snow
	Class 220	Permanent snow and ice	

Figure 2.2: ESA CCI LC gridded map classifications and aggregated sub-classification. The table contains the 22 classifications offered by the ESA CCI LC and the aggregated sub-classifications created by the author. Adapted from source: Copernicus Climate Change Service, 2019; ESA—European Space Agency, 2014.

The ESA CCI LC gridded maps contain 22 LC classifications defined using the United Nations Food and Agriculture Organization (UN FAO) LC classification system (Copernicus Climate Change Service, 2019). The ESA CCI LC gridded maps have a resolution of 300 meters and a coverage starting from 1992 until the present; the overall accuracy is 70.7% for the period 1992 to 2015, while the latter period has a lower accuracy of 70.77% (ESA—European Space Agency, 2014; Copernicus Climate Change Service, 2019). These LC classifications represent a standardized approach to identifying global LC types, providing a reliable dataset to analye LCC and their relationship with LST. In this study, the 22 classifications were used to comprehensively evaluate how changes in LC influence LST. Figure 3.2 summarizes the ESA CCI LC classifications and their corresponding subcategories, offering a clear overview of the aggregated types.

To allow for a clearer interpretation, the 22 classifications were aggregated into six sub-categories: Agriculture, Forest, Grass & Shrubs, Flooded Vegetation, Bare & Built-up, and Water & Snow. This aggregation was based on the intrinsic characteristics of the LC types. For example, classes 10 to

40, which include various cropland types, were grouped under "Agriculture". Classes 50 to 100, comprising tree cover and mosaic tree and shrubs (>50%), were classified as "Forest". Classes 110 to 150, representing trees and shrubs (<50%), shrubs, grass, lichens, and sparse vegetation, were grouped into "Grass & Shrubs". Classes 160 to 180, consisting of trees and shrubs flooded with water, were classified as "Flooded Vegetation". Bare areas and urban or built-up environments, corresponding to classes 190 and 200, were grouped as "Bare & Built-up". Lastly, water bodies and permanent snow and ice, corresponding to classes 210 and 220, were classified under "Water & Snow". The aggregation into six different categories not only simplifies the dataset but also facilitates a focused assessment of the overall status and transitions within each category type.

The ESA CCI LC data is provided in NetCDF-4 format and was sourced from the Copernicus CCI service's climate data store. Two versions of the dataset were utilized in this study: v2.0.7cds which covers the period from 1992 to 2015, and v2.1.1 covering 2016 to 2022 (ESA—European Space Agency, 2014) The two different versions ensure temporal continuity and offer a long-term perspective on global LCC. To maintain consistency with the LST data format, all ESA CCI LC data downloaded were converted to Georeferenced Tagged Image File (GeoTIFF) format. Furthermore, their coordinate systems were standardized to the WGS 84 projection (EPSG 4326) for processing tasks, ensuring that the coordinate systems are similar to ensure compatibility during the analysis while providing an accurate projection. On the other hand, the equal-earth projection (EPSG 8857) was used for visualization purposes, which is aesthetically appropriate for global-scale mapping to ensure that the regions are representing their most accurate size possible.

2.3 Other datasets considered

Table 2.3: Compiled summary of the LC datasets considered for the study. The LC datasets considered include MODIS (MCD12Q1.061), Dynamic World (Sentinel-2), and Copernicus Global (CGLS-LC100). Adapted from source: Friedl et al., 2022; Brown et al., 2022; Buchhorn et al., 2020.

Name / Satellite	Start	End	Resolution	Frequency	Classes
MODIS (MCD12Q1.061)	January 01, 2001	January 01, 2022	500 meters	Yearly	17
Dynamic World (Sentinel-2)	June 27, 2015	Present	10 meters	2-5 Days	9
Copernicus Global (CGLS-LC100)	January 01, 2015	January 01, 2019	100 meters	Yearly	23

The study also considered and tested a variety of datasets. MODIS LC was initially selected due to its consistent format, metadata, and resolution, which were expected to reduce uncertainties (Popp et al., 2020). However, there are studies that have shown that MODIS LC is less accurate compared to those obtained using ESA CCI LC. MODIS LC Type 1 International Geosphere-Biosphere Programme (IGBP) reportedly has a global accuracy of 73.6% (Sulla-Menashe et al., 2019), while MODIS LC Type 3 demonstrates a spatial similarity of only 58.17% which was largely attributed to misclassification issues (Liang et al., 2015). Further studies revealed significant regional discrepancies in accuracy between the two datasets. In the Loess Plateau of China, MODIS LC showed an overall accuracy ranging from 55.3% to 58.2%, whereas ESA CCI LC achieved a higher accuracy of 73.9% to 74.2% (Sun et al., 2022). In the Arctic regions, ESA CCI LC exhibited an accuracy of 63.5%, compared to just 29.5% for MODIS, likely due to substantial variances in classification (Liang et al., 2019). Similarly, in the Yellow River Basin, ESA CCI LC achieved an impressive accuracy of 85%, while MODIS accuracy was only 21% (Liu et al., 2023). On the other hand, datasets such as the dynamic world and copernicus global LC may have a higher resolution but the timespan was deemed insufficient for the study.

Table 2.4: Overview of the Landsat satellite observation data attributes. The LST datasets that were considered by the author are the combination of all the available Landsat satellites. Adapted from source: Hemati et al., 2021; Wulder et al., 2022.

Satellite	Start	End	Resolution	Frequency
Landsat 5	March 1984	June 2013	Visible: 30 meters Thermal: 120 meters (resampled to 30 meters)	16 Days
Landsat 7	April 1999	June 2003 (SLC Error)	Visible: 30 meters Thermal: 60 meters (resampled to 30 meters)	16 Days
Landsat 8	February 2013	Present	Visible: 30 meters Thermal: 100 meters (resampled to 30 meters)	16 Days

Landsat was introduced in the 1970s by the U.S. Geological Survey (USGS), with the Earth Resources Observation and Science (EROS) Center managing the reception, processing, distribution, and archiving of Landsat imagery, a program that continues today with Landsat-8 and 9 in operation (Goward et al., 2006; Williams et al., 2006; Wulder et al., 2008b; Masek et al., 2020). The Landsat products applicable to this study include Landsat 5 (March 1984 to June 2013), Landsat 7 (April 1999 to June 2003, before the Scan Line Corrector (SLC) failure), and Landsat 8 (February 2013 to present) offers thermal resolutions of 120, 60, and 100 meters, respectively (Hemati et al., 2021; Wulder et al., 2022), which are higher than the thermal resolution of MODIS. Although landsat data has a higher resolution, the researcher decided to use MODIS for the following reasons: (i) landsat datasets have a higher resolution but would require a higher data storage requirement, (ii) Landsat 7 data would require SLC corrections (Wang et al., 2024; Wulder et al., 2008b; Chen et al., 2011), (iii) images were occasionally collected repeatedly in areas with minimal seasonal variation or during the wrong season, leading to low coverage (Arvidson et al., 2006; Wulder et al., 2008b), (iv) multiple Landsat images need to be composited to address data gaps and cloud cover (Wijedasa et al., 2012; Wulder et al., 2011; Wulder et al., 2008a), (v) combining datasets with different spatial resolutions can lead to scale issues (Johnson, 2015; Sun and Schulz, 2015), and lastly (vi) orbital drift in Landsat 7 is noticed after 2018 and the irregularities in Landsat 5's orbit caused significant variations in acquisition times (Gök et al., 2024; Qiu et al., 2021; Zhang and Roy, 2016)

3 Methodology

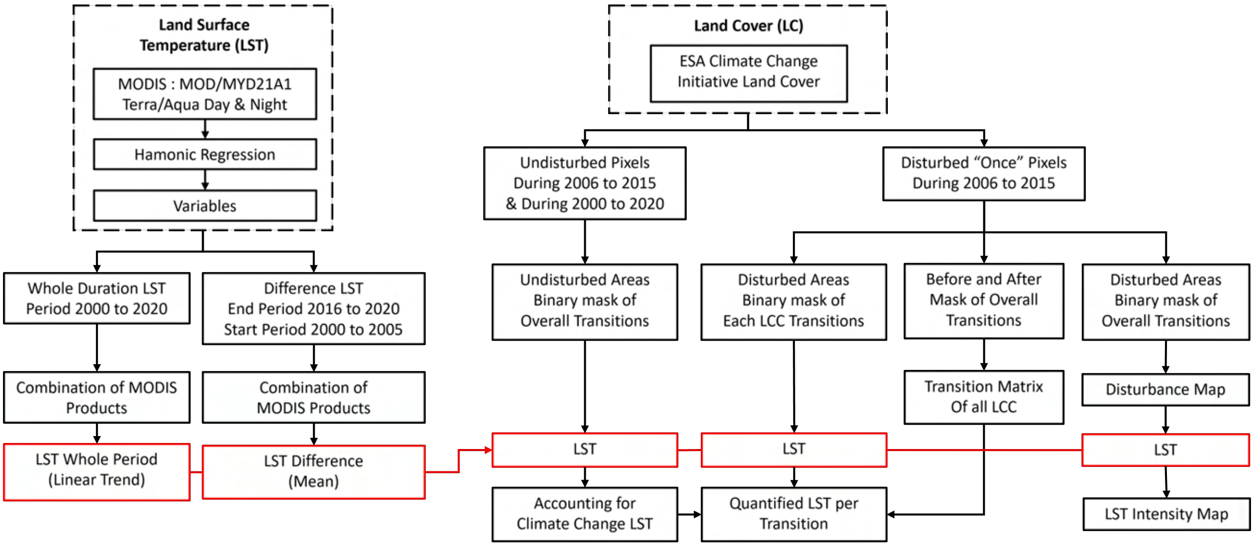

Figure 3.1: General workflow methodology for quantifying land surface temperature associated with land cover changes. The methodology is divided into two parts: (i) processing of the land surface temperature (left), and (ii) processing of the land cover (right), both of which are integrated together through the red highlight.

The methodology workflow of the study is designed to comprehensively analyze the relationship between LST and LC changes on a global scale. The approach integrates advanced models, datasets, and analytical techniques to capture both the temporal and spatial dynamics of this relationship. Using the capabilities of the harmonic model and the MODIS LST products, alongside the ESA CCI LC dataset, the study constructs a robust pipeline for detecting and interpreting patterns of LST variation across different LC transitions.

The first part of the process begins with the application of the harmonic model to the LST data as seen on the left side of Figure 3.1, which employs a single harmonic term to capture the dominant annual cycle of temperature variations. This model effectively disentangles long-term trends from seasonal patterns, generating key outputs such as linear trends, amplitude, and phase. The harmonic model coefficients are processed using the GEE platform, enabling the efficient handling of large-scale datasets and facilitating the generation of insights on LST variations over time ((Amani et al., 2020; Ahmed et al., 2023; Zhao et al., 2021).

The second part of the process is seen on the right side of Figure 3.1, which aims to analyze LC changes using the ESA CCI LC dataset, providing a globally consistent classification system. The LC dataset is processed to create the undisturbed and disturbed area masks. The undisturbed mask identifies regions where the LC has remained constant, serving as a baseline to isolate the influence of external factors such as climate change. On the other hand, the disturbed mask highlights areas where LC transitions have occurred and was used as a foundation for quantifying the thermal impact of these changes. Both undisturbed and disturbed areas enabled a precise examination of the interplay between LC and LST, with adjustments made to account for external influences.

A critical component of the analysis is the integration of MODIS LST products towards the LC changes, this is highlighted in Figure 3.1 in red. Three distinct combinations of the MODIS LST products are evaluated to derive the most accurate LST estimates. These combinations balance the strengths and limitations of daytime and nighttime observations from the Aqua and Terra satellites, ensuring a refined representation of LST for both global and regional analyses. The adjusted LST values for disturbed areas are normalized against undisturbed values, enhancing the reliability of the findings by excluding the effects of non-LC related variations.

Finally, the methodology workflow incorporates visual tools such as transition matrices and bubble plots to represent the spatial and thermal dynamics of the LC transitions. These visualizations provide an intuitive means to understand the magnitude, spatial extent, and thermal impacts of LC changes. Combined with statistical techniques such as inter-quartile range (IQR) filtering, the methodology ensures that the analysis can address the complexities of global LST-LC interactions.

By systematically integrating these processes, the study delivers a comprehensive and nuanced understanding of how LC changes influence LST. The findings not only highlight key patterns and trends, but also underscore the importance of addressing LC changes as a critical aspect of climate dynamics on a global scale.

3.1 Timeline and study area

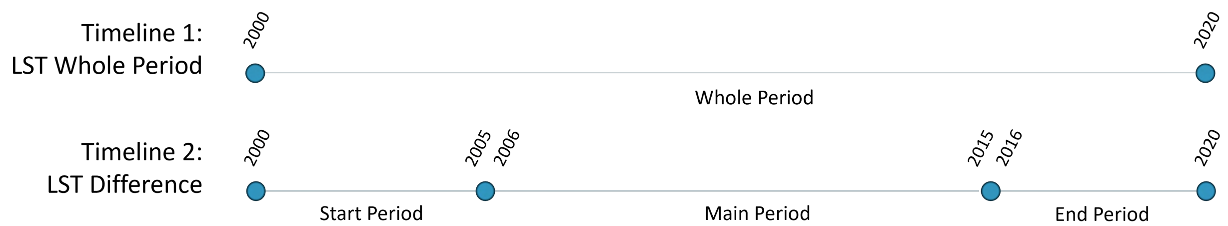

Figure 3.2: Visualization of the two LST timelines used for the the study. The figure emphasizes the two different timelines used in the study namely: (i) Timeline 1: LST Whole Period (top) and (ii) Timeline 2: LST Difference (bottom).

The study is divided into two timelines that span from 2000 until the year 2020. Timeline 1, referred to as "LST Whole Period", spans the entire 2000–2020 period and focuses on the linear trend

LST (β) to analyze long-term changes. While Timeline 2, referred to as "LST Difference", divides the study period into three intervals: the start period (2000–2005), the main period (2006–2015), and the end period (2016–2020). For Timeline 2, the mean LST ($L\bar{S}T$) is calculated for each of these intervals, with the difference between the end and the start periods used to assess the overall changes in LST over time.

The decision to limit the study up until 2020 takes into account findings from the study by Feng et al. (2024) that highlights the influence of orbital drift on Terra MODIS snow albedo (Feng et al., 2024). Although the effect of the orbital drift starting in 2020 (+0.01 Degrees) is minimal (Feng et al., 2024), it can potentially introduce biases in temporal studies, making 2020 an appropriate cutoff for ensuring data reliability. Additionally, research by Gök et al. (2024) reveals that LST trends related to deforestation were more consistent during the 2006–2015 period, underscoring the importance of focusing on this interval for analyzing LCC (Gök et al., 2024). Since the LST is consistent from 2006 to 2015, the disturbance on the LCC is selected only within this period.

MODIS datasets are actively available; however, according to a study conducted by Feng et al. (2024), the effect of orbital drift on the snow albedo of the MODIS terra was +0.01 starting in 2020 due to the apparent effect of orbital drift on the MODIS data(Feng et al., 2024). Results of their study show that although the increase is negligible, it could be a potentially biasing influence on temporal studies, thus in consideration, the timeline of the study is only until 2020. Furthermore, according to a study conducted by Gök et al. (2024), the LST Trends on the influence of deforestation are consistent starting from the year 2006 to 2015 (Gök et al., 2024). Since the LST is consistent from 2006 to 2015, the LCC is only selected within this period, and the mean LST is taken from the start period, main period, and the end period.

Four MODIS datasets are utilized in this study: MODIS terra day, MODIS terra night, MODIS aqua day, and MODIS aqua night (see Section 2.1: Land surface temperature - MODIS (MOD21A1 series)). These products are processed using the harmonic model (Section 3.1.2: Harmonic model), which captures both seasonal and long-term variations. The analysis leverages MODIS data for robust and scalable processing, ensuring accurate insights into global LST dynamics.

To fully understand the relationships between LC and LST, a global area of interest (AOI) is used to include all available pixels for each LCC transition enabling a comprehensive analysis of how LC changes influence LST across diverse geographic regions. By adopting a global perspective, this study minimizes the variability caused by localized anomalies and emphasizes the importance of addressing LCC as a global challenge. While regional studies provide localized insights, this broader approach delivers a holistic understanding of how LC changes impact climate dynamics on a global scale.

3.2 Land surface temperature analysis

3.2.1 Harmonic model

The harmonic model applies linear regression using Ordinary Least Squares (OLS) to estimate the coefficients for a combination of linear and harmonic terms, providing a robust framework for analyzing data with long-term trends and periodic variations (Gök et al., 2024; Polasek, 2013; Peng Fu and Qihao Weng, 2015). In this study, a single harmonic term (N=1) is used, which is particularly effective for the LST analysis, as it captures the dominant annual cycle of temperature variations(Gök et al., 2024; Polasek, 2013; Peng Fu and Qihao Weng, 2015). Including just one harmonic term strikes a balance between model complexity and interpretability, ensuring that the dominant cycle is represented without overfitting or introducing unnecessary computational overhead(Gök et al., 2024; Polasek, 2013; Peng Fu and Qihao Weng, 2015).

The harmonic model equation is:

$$LST(t) = C + \beta \cdot t + \sum_{n=1}^{N} [a_n \cdot \sin(2\pi n \cdot t) + b_n \cdot \cos(2\pi n \cdot t)]$$

The harmonic model provides key outputs including (i) the linear trend (β) to capture long-term changes, (ii) data count for the number of valid observations, (iii) constant (C) representing the baseline LST value, (iv) amplitude (A) for the magnitude of seasonal variations, (v) phase (ϕ) indicating the timing of seasonal peaks, (vi) RMSE (Root Mean Square Error) to measure model accuracy, and (vii) mean ($L\bar{S}T$) for the average fitted value over the time period (Gök et al., 2024; Zhu and Woodcock, 2014; Polasek, 2013; Peng Fu and Qihao Weng, 2015; Fu and Weng, 2016). By utilizing GEE's cloud-based computational capabilities, the harmonic model coefficients were efficiently generated, enabling large-scale processing and analysis of LST data while facilitating the examination of global or regional temperature trends and variations with unprecedented speed and scalability.

3.2.2 Combination of the MODIS products

Numerous studies are being conducted to deepen the understanding of the behavior, trends, and the accuracy of the relationships associated with the different MODIS LST products taken during the day and night. For instance, Bala et al. (2020) conducted a comparative analysis of day and night LST in two semi-arid Indian cities, demonstrating the effectiveness of various models across seasons and highlighting the importance of day-night differences in semi-arid urban areas (Bala et al., 2020). Eleftheriou et al. (2018) investigated day and night trends in MODIS LST values over Greece and their implications for environmental monitoring and climate studies (Eleftheriou et al., 2018). Sun et al. (2014) estimated mean air temperatures using MODIS day and night LST (Sun et al., 2014). Xing et al. (2021) furthered this understanding by focusing on estimation methods for daily mean LST using MODIS daytime and nighttime observations, highlighting the potential for improved temporal resolution and data accuracy (Xing et al., 2021). Luintel et al. (2019) analyzed spatial variations in LST across Nepal, comparing MODIS daytime and nighttime products to provide critical insights into regional heat patterns and their environmental impacts (LUINTEL et al., 2019). Collectively, these studies contribute to the refinement of the accuracy of MODIS LST products by addressing the various aspects of MODIS LST data, such as diurnal temperature variations, seasonal effects, and regional-specific dynamics, enhancing their reliability for applications such as urban heat island analysis, agricultural monitoring, and climate change assessment.

In a study conducted by Zhang et al. (2016), the root mean square difference (RMSD) of 15 combinations of MODIS aqua, terra, day and night products was analyzed to evaluate their accuracy in estimating LST (Zhang et al., 2016). The study revealed several key findings: (i) the RMSD of terra and aqua day combinations was higher than that of terra and aqua night, suggesting that nighttime observations tend to be more consistent; (ii) the RMSD of day combinations was consistently higher than night combinations, indicating greater variability in daytime data; (iii) combinations of day and night products from terra and aqua yielded similar RMSD values, suggesting a limited added benefit in combining day and night data; (iv) combinations of three MODIS products showed negligible improvements in RMSD compared to using two products; and (v) the combination of all four MODIS products: aqua day, aqua night, terra day and terra night resulted in the lowest RMSD, demonstrating that integrating all available observations improves the accuracy of the estimation of LST (Zhang et al., 2016). These results emphasize the importance of leveraging the full range of MODIS products to improve the reliability and precision of LST data for environmental and climate studies.

The study would require the most accurate representation of LST to effectively quantify its relationship between LCC. Accurate LST data are critical to capture subtle temperature variations influenced by LC transitions and to ensure that the findings are precise and meaningful. Although combining all four MODIS products: aqua day, aqua night, terra day and terra night has been proven to produce the lowest RMSD (Zhang et al., 2016), the challenge lies in identifying the most effective method to combine these products. The integration must accurately account for variability of MODIS LST products to minimize errors and improve the overall reliability of LST estimates. To address these challenges, Xing et al. (2021) conducted a global study focusing on the estimation of the daily mean LST using the MODIS MOD11A1 products where they employed a multiple linear regression analysis to integrate the MODIS products, assigning weights to each based on their contributions to the overall accuracy (Xing et al., 2021). By leveraging this approach, Xing et al. (2021) achieved the highest reported accuracy, with a root mean square error (RMSE) of 0.80 K (Xing et al., 2021). This level of precision underscores the effectiveness of weighting individual products to account for their unique strengths and limitations, leading to a more refined representation of the daily mean LST. By adopting similar strategies, this research can ensure that the temperature data used for the analysis reflect the highest possible accuracy, paving the way for more reliable conclusions about the relationship between LST and LCC. The equation used in the study of Xing et al. (2021) is as follows:

$$\begin{aligned}\mathrm{dm\,LST}_g = {} & K_1 \cdot \mathrm{LST}_g(Terra^{\mathrm{day}}) + K_2 \cdot \mathrm{LST}_g(Terra^{\mathrm{night}}) \\ & + K_3 \cdot \mathrm{LST}_g(Aqua^{\mathrm{day}}) + K_4 \cdot \mathrm{LST}_g(Aqua^{\mathrm{night}}) + b\end{aligned}$$

Although the MOD21A1 MODIS LST products exhibit higher accuracy over barren surfaces and comparable accuracy over water and vegetated surfaces, notable differences persist between MOD 21A1 and MOD11A1 due to variations in the algorithms used: MOD21A1 employs the temperature emissivity separation (TES) algorithm for improved emissivity estimates, particularly over barren regions, while MOD11A1 uses the split-window algorithm known for its simplicity and robustness but with slightly less accurate emissivity estimates under certain conditions (Yao et al., 2020). Given these inherent differences between the two products, the equation employed in this study would only require the individual influence of each MOD11A1 product. Specifically, the equation requires only the weights, also referred to as fitting coefficients. By carefully calibrating the fitting coefficients, the equation aligns the datasets for seamless integration to facilitate accurate temperature analysis for LCC studies. The equation along with the adopted weights by the study done by Xing et al. is as follows:

$$\begin{aligned}\mathrm{dm\,LST}_g = {} & 0.1807 \cdot \mathrm{LST}_g(Terra^{\mathrm{day}}) + 0.3210 \cdot \mathrm{LST}_g(Terra^{\mathrm{night}}) \\ & + 0.1907 \cdot \mathrm{LST}_g(Aqua^{\mathrm{day}}) + 0.3241 \cdot \mathrm{LST}_g(Aqua^{\mathrm{night}})\end{aligned}$$

In this study, three distinct combinations of MODIS LST products were used to evaluate their effectiveness in estimating the relationship on LST with LCC. These combinations are as follows:

Combination 1: Linear Regression Equation
Combination 2: Average of Terra and Aqua Day
Combination 3: Average of Terra and Aqua Night

Combination 1 refers to the linear regression equation proposed by Xing et al. (2021), which integrates multiple MODIS products by assigning specific weights or fitting coefficients to each variable (Xing et al., 2021). This method takes advantage of the strength or weight of each MODIS product to accurately estimate the LST. Combinations 2 and 3, on the other hand, are based on simple averaging. Combination 2 involves averaging the terra and aqua day products, while Combination 3 averages the terra and aqua night products. These approaches are designed to account for the significant variability observed between the day and night LST values derived from terra and aqua (Zhang et al., 2016). These combinations provide insights into the overall behavior of daytime and nighttime LSTs and their potential influence on LC dynamics.

3.3 Land cover analysis

3.3.1 Undisturbed areas

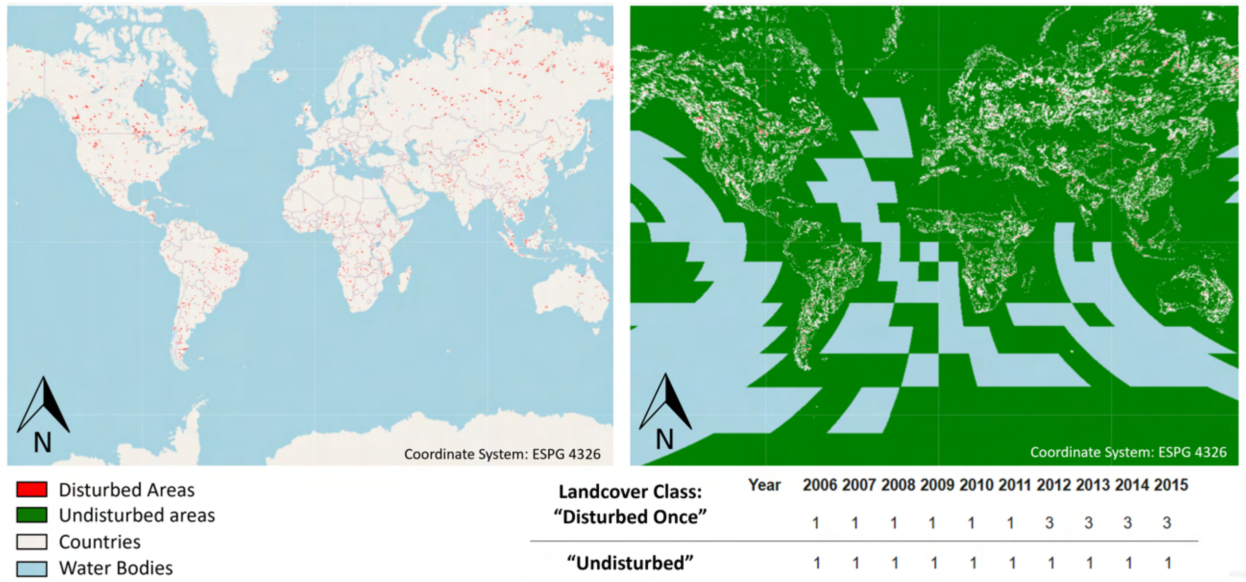

Figure 3.3: Sample representation of the disturbed and undisturbed areas. The image visualizes on how the disturbed mask (left, with pixels shown in red) and the undisturbed mask (right, with pixels shown in green) are selected globally. The basemap source is from Leaflet (https://leafletjs.com).

The undisturbed areas are defined using a global undisturbed mask, which identifies pixels where LC remained unchanged from the start period to the end period. The undisturbed mask is essential to isolate regions unaffected by LCC, providing a stable baseline for analyzing the relationship between LST and LC. There are distinct periods that were used to create the undisturbed mask: (i) 2006 to 2015 representing the "Main Period" from timeline 2, and (ii) 2000 to 2020 which represents the "Whole Period" from timeline 1. The discussion and exploration between the said two timelines is detailed in Section 3.1: Timeline and study area.

By selecting pixels that remained consistent or undisturbed during these periods, the analysis can better account for factors such as climate change, environmental factors, and other factors that may influence LST changes independently of LC transitions. Adjusting the values by accounting for undisturbed areas ensures that the analysis focuses solely on the LST caused by the transitions in the LC. Moreover, the undisturbed mask may also mitigate the influence of other external factors such as orbital drift that can artificially affect LST readings and lead to inaccurate results.

The calculated undisturbed LST values are applied and deducted on the two timelines to address specific analytical needs. For timeline 1: LST whole period, the mask for 2000 to 2020 is used and deducted from the calculated LST, providing a comprehensive and accurate results of the LST trends over the entire period. On the other hand, timeline 2: LST difference would utilize the undisturbed mask for 2006 to 2015 to isolate the external effect during the "Main Period" where the disturbances related to LCC are analyzed.

The undisturbed mask is a binary mask with values of 1 representing undisturbed pixels and 0 indicating disturbed pixels. All LST pixels corresponding to undisturbed areas with binary value 1 from timeline 1: LST whole period and timeline 2: LST difference within their corresponding undisturbed mask periods: (i) 2006 to 2015, and (ii) 2000 to 2020 was subjected to the IQR filtering. This statistical method reduces variability and isolates outliers ensuring that extreme values do not skew the results (Vinutha et al., 2018; Wan et al., 2014). IQR filtering is particularly critical in Timeline 2, where extreme-valued pixels often arise due to the calculated LST difference between the start and end periods. These anomalies that are caused by data gaps or missing pixels resulting in extreme values require the use of this statistical filter to ensure accuracy.

Once the IQR filtering is applied, the mean LST values are calculated for each period. Calculating the mean provides a clear and reliable measure of the average LST in undisturbed areas, serving as a reference to assess the impact of LST in these regions. The approach and analysis ensure that the observed trends accurately reflect the influence of LST through LCC, while excluding the effects of climate-induced variations, artifacts, or other factors that could skew the results. By eliminating such external influences, this comprehensive method establishes a foundation for understanding the interplay between LST and LC dynamics.

3.3.2 Disturbed areas

The disturbed areas is represented by a global disturbance mask, identifying regions where the LC of the ESA CCI has changed once from one classification to another during the main period: between 2006 and 2015 as highlighted in Figure 3.3.

Three main processes were performed using this disturbance mask:

1. Before and After Mask of Overall Transitions
2. Disturbed Areas Binary Mask of Each LCC Transitions
3. Disturbed Areas of the Overall Transitions

3.3.2.1 Before and after mask of overall transitions

This part of the workflow is the first component of the methodology in the LCC analysis consisting of two distinct LC images. The "Before Mask" captures the global distribution of LC classifications prior to any transitions, while the "After Mask" reflects the LC classifications following the transitions. The before and after masks served as input to generate the transitions from one class to another. Furthermore, it is used for understanding how LC has changed over time on a global scale, providing a detailed overview of the pre- and post-transition states.

These masks are utilized to generate a transition matrix that is a vital tool for quantifying LCC. The transition matrix calculates the area size in square kilometers by counting the number of pixels associated with each before and after LC classification (Gallego, 2004; Waldner and Defourny, 2017 and multiplying these counts by the pixel resolution of 300 meters (Copernicus Climate Change Service, 2019). Creating the transition matrix of the area coverage allows for precise estimation of the spatial extent of transitions capturing the magnitude of changes and transitions across different LC classifications. The calculated area sizes within the transition matrix play a vital role in the subsequent analysis, especially in Section 3.3.2.2: Disturbed areas binary mask of each LCC transition, to identify and assess relevant global LC pixels. By distinguishing between significant and insignificant changes, the matrix helps refine the analysis, ensuring that only meaningful transitions are included in further evaluations.

Finally, a global statistics derived from the before and after masks are used to analyze the overall trends in LCC. These statistics provide insights into the general behavior of each LC classification as well as the aggregated types, highlighting patterns such as increases or decreases in specific classifications. Furthermore, the global statistics would enable the identification of the dominant global LC classifications, offering a comprehensive overview of the most dominant classification and changes occurring globally. By integrating pixel level data to the transition matrix and the global statistics, the analysis delivers a deeper understanding of the LC dynamics.

3.3.2.2 Disturbed areas binary mask of each LCC transition

This part of the methodology is one of the main processes consisting of a 22 x 22 binary matrix derived from the 22 LC classifications in the ESA CCI LC dataset. In each LC classification binary mask, a value of 1 would represent disturbed pixels indicating areas where the LC has changed from one classification to another, while 0 denotes undisturbed pixels where no transitions occurred. The LC classification binary masks serve as the basis for the analysis of the relationship between LC and LST dynamics.

To ensure the accuracy of the analysis, all LST pixels corresponding to disturbed areas (binary value 1) from both timeline 1: LST difference and timeline 2: LST whole period undergoes IQR filtering to reduce variability and detect outliers (Vinutha et al., 2018; Wan et al., 2014). Similar to Section 3.2.1: Undisturbed areas, the extraction of LST pixels from timeline 1: LST difference is important because of the occurrence of extreme-valued pixels due to the calculation of the LST differences. The IQR-filtered LST values provide a more reliable dataset by minimizing noise and ensuring that the calculations reflect meaningful trends.

Following IQR filtering, the LST values for each LCC transition were further adjusted by subtracting the corresponding LST values derived from undisturbed areas. As discussed in Section 3.2.1 on undisturbed areas, this adjustment accounts for factors that can influence LST changes independently of LC transitions. This step isolates the specific impact of LCC on LST, improving the accuracy and relevance of the analysis.

The final adjusted LST values for each LCC were visualized using a transition matrix bubble plot. In this visualization, each bubble represents a specific LCC transition, with its size corresponding to the area of the transition (in square kilometers) and its color indicating the mean LST value. The visualization of the transition matrix bubble plot allows for easy comparison of LCC transitions in terms of both spatial extent (size) and thermal impact of LST, highlighting key patterns and trends.

By integrating the IQR filtering, normalization, and visual representation through the transition matrix bubble plot, this part of the methodology provides a comprehensive framework for quantifying the LST variations associated with the LCC. Through this approach, the study can provide valuable information on the spatial and thermal dynamics of LC transitions, supporting efforts to assess and mitigate the impacts of these changes on global and regional climates.

3.3.2.3 Disturbed areas of the overall transitions

This part of the methodology represents the combined 22 x 22 matrix of disturbed pixels, where a value of 1 indicates a disturbed pixel. The disturbance map generated provides a comprehensive visualization of the global distribution of disturbed areas, allowing the identification of regions most significantly affected by LCC. By aggregating the disturbed pixels across all classifications, the map highlights the disturbance patterns at a global scale that offers insights into the spatial distribution of the LC transitions. In addition to the disturbance map, an LST intensity map was generated to represent the global distribution of the LST pixels. The LST intensity map is crucial to understand how disturbances in the LC correlate with changes in temperature. The LST intensity map allows researchers to observe temperature variations across disturbed regions, providing valuable data on the thermal impact of LCC.

Both the disturbance map and the LST intensity map were accompanied by distribution plots to further enhance the analysis. These plots display the distribution of disturbed and temperature pixels by latitude, divided into increments of 20 degrees that provides a more detailed view on how disturbances and temperature variations are distributed across different regions starting from the equator towards the poles. Lastly, the combination of the maps and these distribution plots provides insight into the relationship between LC and LST, as well as the global patterns around it.

4 Results

4.1 Land surface temperature results

Two LST products were derived from two distinct timelines: timeline 1: whole period representing the LST linear trend, and timeline 2: LST difference calculated from the difference between LST values in the end period and the start period as detailed in Section 3.1: Timeline and study area. These timelines are critical for understanding temperature dynamics over time offering complementary approaches to analyze LST changes: timeline 1 offers a continuous trend perspective, while timeline 2 focuses on the overall changes over a 10-year period. To analyze and explore LST variations between day and night and their relationship with LCC, three combinations were used: combination 1: linear regression equation, combination 2: average of terra and aqua day, and combination 3: average of terra and aqua night, as explained in Section 3.2.2: Combination of the MODIS products. The three combinations were compared using timeline 2: LST difference, with the results visualized in Figure 4.1: combination 1 - linear regression equation, Figure 4.2: combination 2 - average of terra and aqua day, and Figure 4.3: combination 3 - average of terra and aqua night.

Figure 4.2 (combination 2) shows more prominent cooling and warming areas, reflecting greater variability in daytime LST due to dynamic heating and cooling processes. In contrast, Figure 4.1 (combination 1) and Figure 4.3 (combination 3) exhibit similar global patterns of warming and cooling, highlighting the stability of nighttime LST which is less influenced by diurnal fluctuations. Nighttime LST reflects the thermal properties of LST such as heat retention and release and is generally more stable, aligning with the findings of Zhang et al. (2016) that nighttime data exhibit lower RMSE compared to daytime data (Zhang et al., 2016). The variability between daytime and nighttime LST highlights the influence of factors such as albedo, vegetation cover, and urban heat islands. During the day, high-albedo surfaces such as bare soil, reflect solar radiation, while urban areas and dense vegetation absorb heat, causing localized warming. At night, these effects subside, allowing thermal properties to dominate (Nichol, 2005; Hain and Anderson, 2017).

In conclusion, the comparison of the three combinations provides valuable insights into the diurnal variations in LST. While daytime LST (combination 2) reveals greater variability driven by dynamic processes, nighttime LST (combination 3) and the LST linear regression equation (combination 1) offer more consistent patterns, making it a reliable indicator for analyzing stable temperature trends. These findings emphasize the importance of incorporating both daytime and nighttime observations to fully understand LST changes.

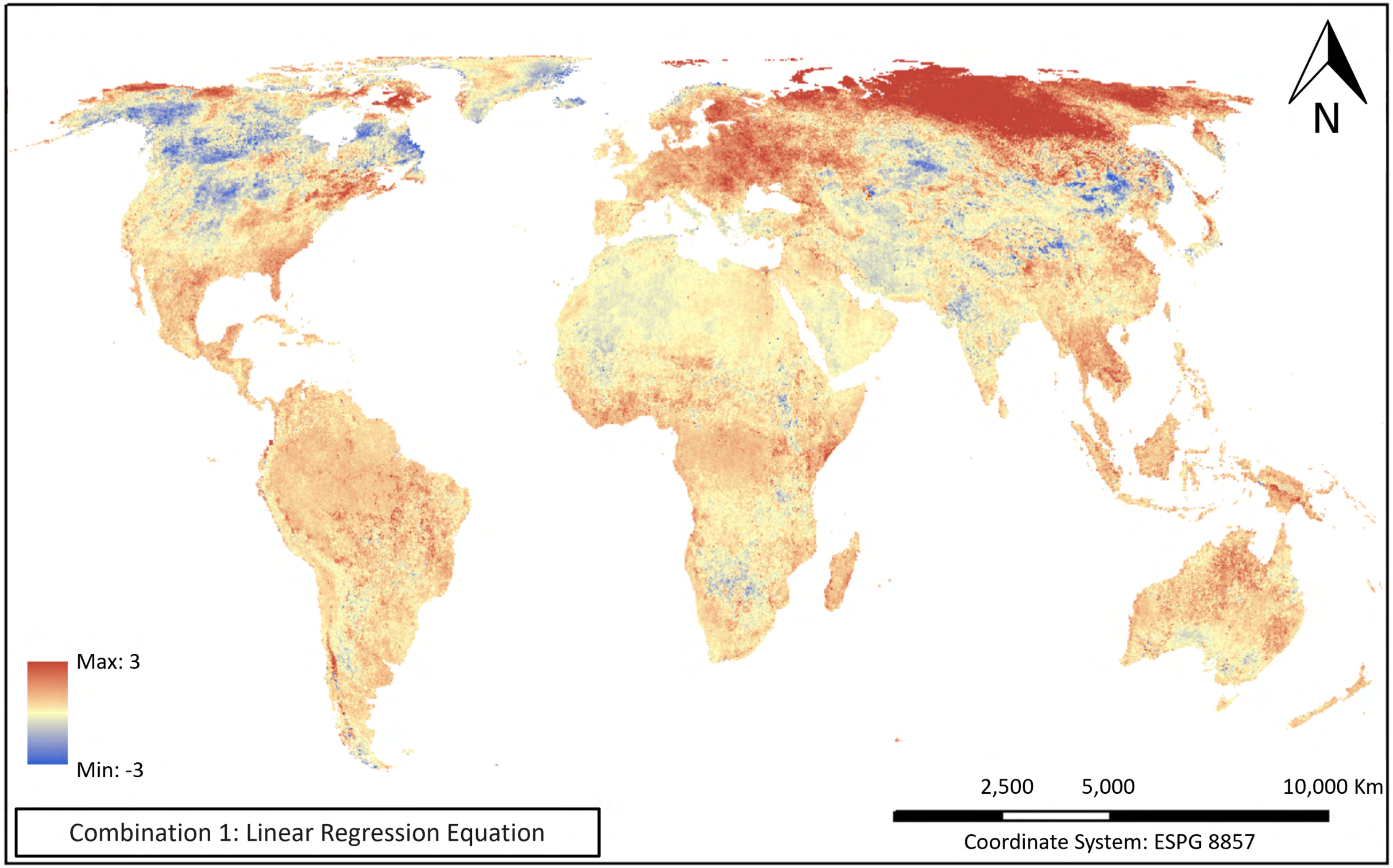

Figure 4.1: Visualization of the combination 1: linear regression equation using the LST difference (timeline 2). The map was created using the LST from timeline 2 (discussed in Section 3.1) and calculated with combination 1: linear regression equation (discussed in Section 3.2.2). The map was generated using ESRI ArcMap software (version 10.8).

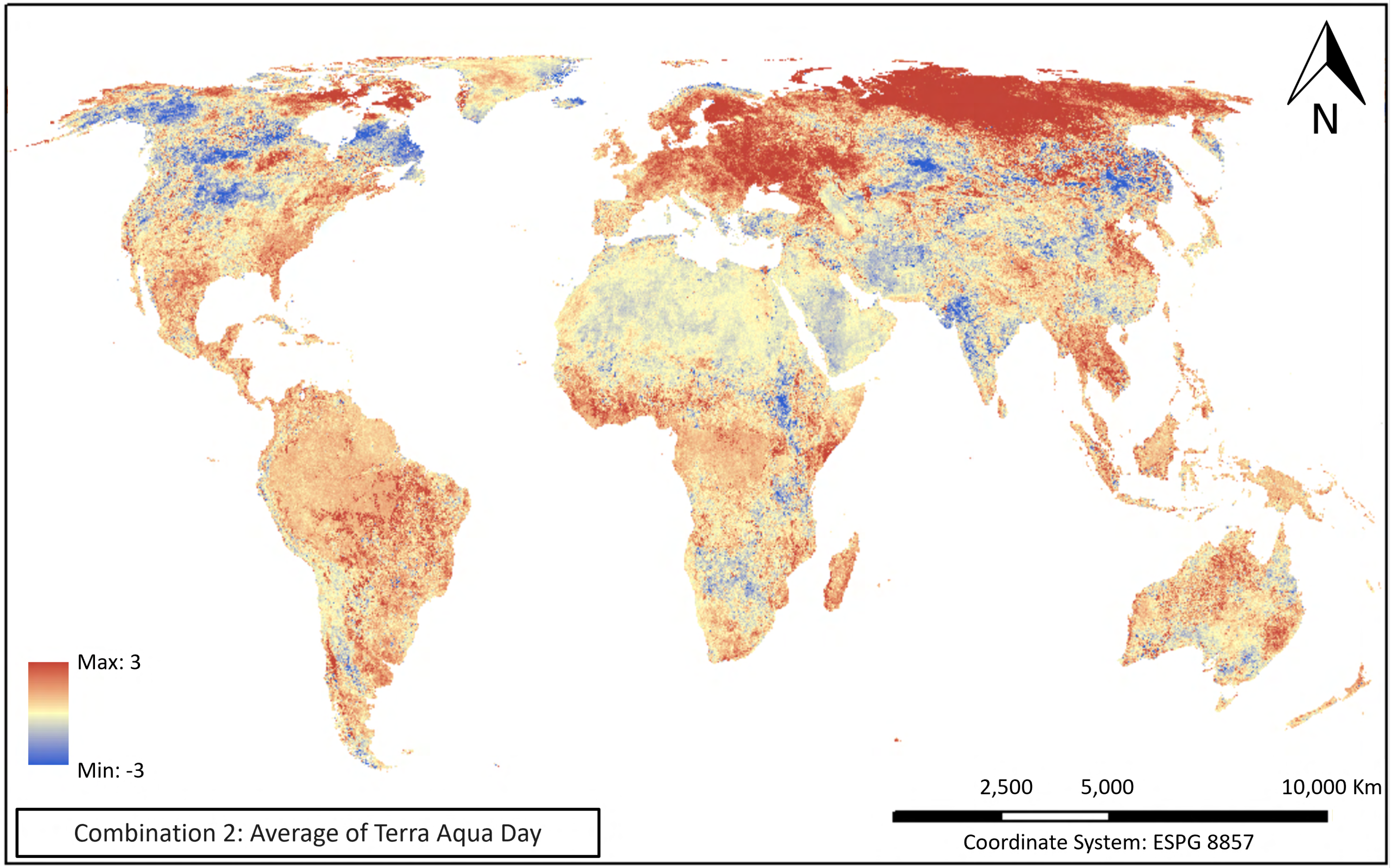

Figure 4.2: Visualization of the combination 2: average of terra aqua day using the difference of mean LST (timeline 2). The map was created using the LST from timeline 2 (discussed in Section 3.1) and calculated with combination 2: average of terra aqua day (discussed in Section 3.2.2). The map was generated using ESRI ArcMap software (version 10.8).

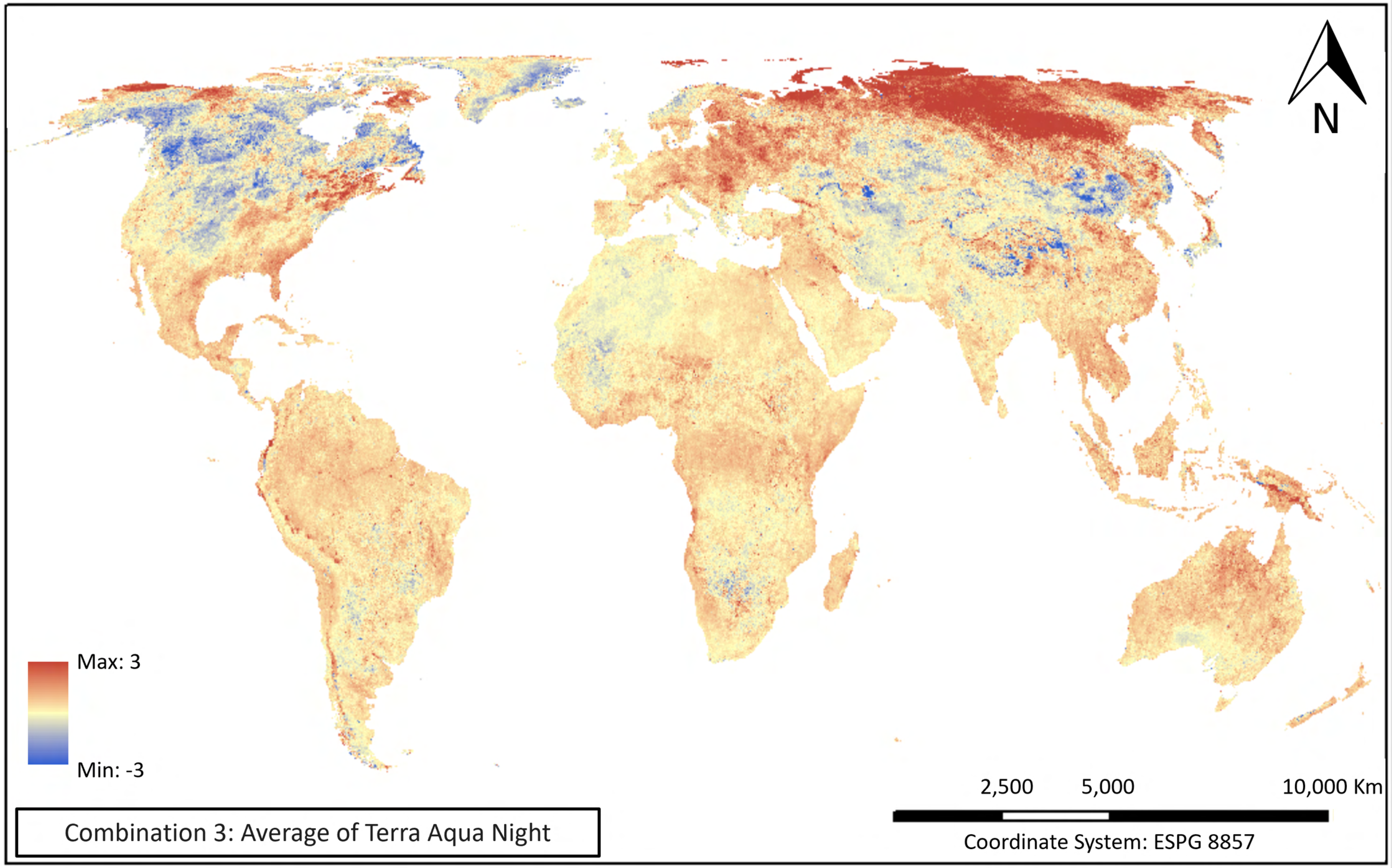

Figure 4.3: Visualization of the combination 3: average of terra aqua night using the difference of mean LST (timeline 2). The map was created using the LST from timeline 2 (discussed in Section 3.1) and calculated with combination 3: average of terra aqua night (discussed in Section 3.2.2). The map was generated using ESRI ArcMap software (version 10.8).

4.2 Land cover change results

4.2.1 ESA CCI LC global statistics

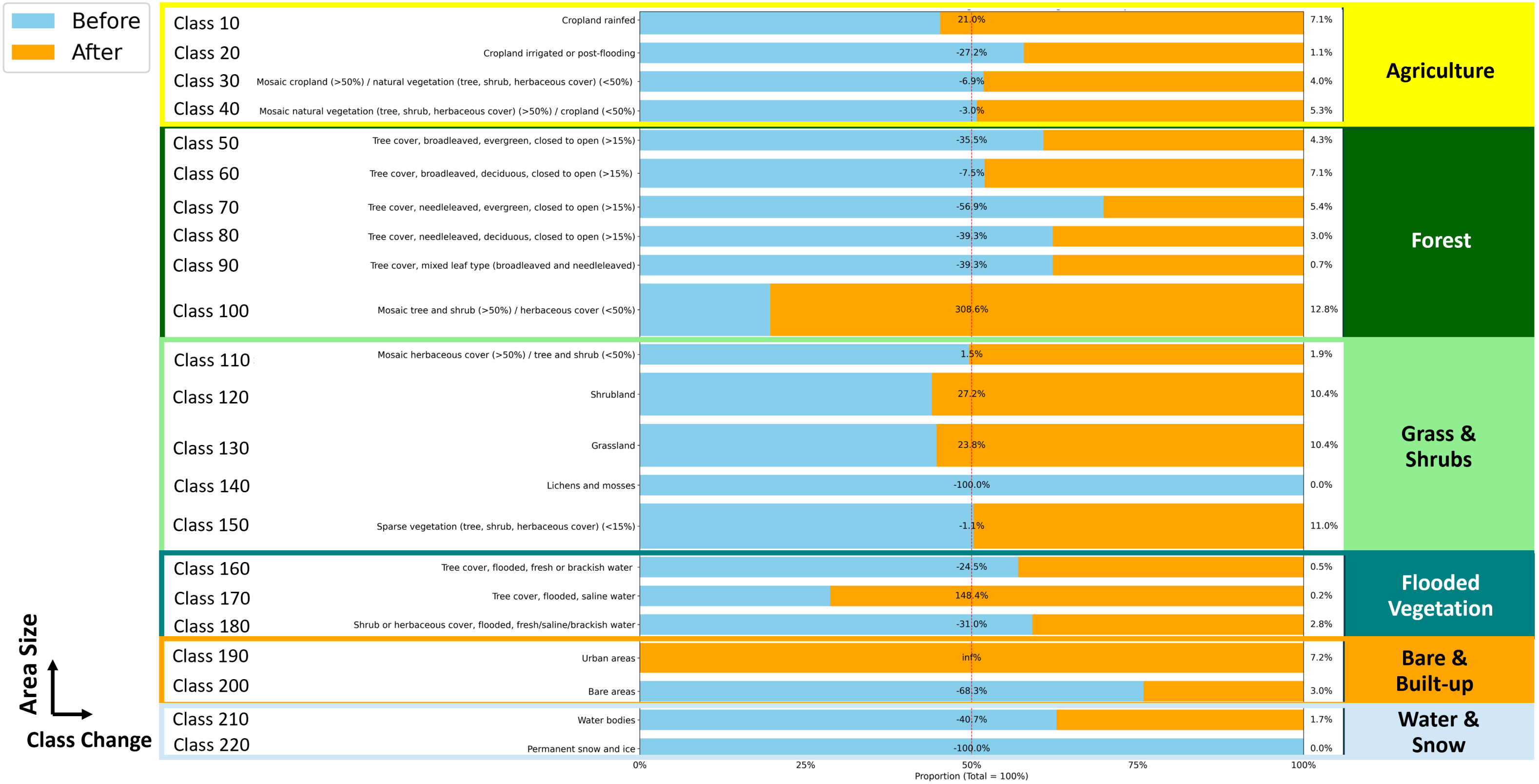

Figure 4.4: ESA CCI land cover classification global statistics for disturbed areas. The ESA CCI land cover statistics, based on the disturbed areas (discussed in Section 3.3.2), represent the total area of each class by the height of the bar, the total class change by the width of the bar, and the aggregated classification on the right.

The ESA CCI LC comprises 22 classifications, which are further aggregated in this study into six categories: agriculture (yellow), forest (green), grass and shrubs (light green), flooded vegetation (blue green), bare and built-up (orange), and water and snow (light blue), as outlined in Section 3.2.3. Based on global statistics derived from the before and after mask discussed in Section 3.3.2.1: Before and after mask of the overall transitions, Figure 4.4 illustrates the total class changes for each classification. For each classification, the before classification is represented by "blue" horizontal bars, while the after classification is represented by "orange" horizontal bar connecting the class as a whole. The vertical size of the bars reflects the total area size of each classification globally, providing a clear picture of the weight of the class.

From Figure 4.4, it is evident that the majority of global disturbances occur in the aggregated classification types "Forest" and "Grass & Shrubs" due to its combined global area size. These disturbances are followed by changes in the classification type "Agriculture", indicating significant transitions within these LC types. In contrast, the categories "Flooded Vegetation", "Bare & Built-up", and "Water & Snow" exhibit the smallest global areas.

When analyzing the "Agriculture" category, most classifications show a decrease. Specifically, class 10: rainfed cropland experienced an increase of 21%, while class 20: irrigated cropland, class 30: mosaic cropland, and class 40: mosaic natural vegetation declined by 27.2%, 6.9%, and 3%, respectively. This indicates a shift in agricultural practices or transitions to other LC types than agriculture.

The "Forest" category displays significant changes, with class 50: tree cover - evergreen broadleaf, class 60: tree cover - deciduous broadleaf, class 70: tree cover - evergreen needleleaf, class 80: tree cover - deciduous needleleaf and class 90: tree cover - mixed broadleaf & needleleaf decreasing by 35.5%, 7.5%, 56.9%, 39.3%, and 39.3%, respectively. The decreases in these tree cover or forests type suggest deforestation, degradation, or conversion to other LC types. However, class 100: mosaic tree and shrub (>50%), shows a remarkable increase of 308.6%. The substantial increase in the class 10: mosaic tree and shrub (>50%) could be attributed to the inclusion of both trees and shrubs within a single classification, making it one of the largest area classifications globally. This trend highlights the need for efforts such as afforestation or natural regrowth in areas previously classified differently.

Within the "Grass & Shrubs" category, class 110: mosaic herbaceous cover and class 150: sparse vegetation (<15%) show negligible change, while class 120: shrubland and class 130: grassland exhibit an increase at a rate of 27.2% and 23.8%. However, class 140: lichens and mosses, has completely disappeared during the transition, indicating a total loss of this classification during this time period.

For the "Flooded Vegetation" category, class 160: tree cover - flooded, fresh or brackish water and class 180: shrub or herbaceous cover, flooded water decreased by 24.5% and 31%, respectively, highlighting the impact of reduced wetland areas or alterations in hydrological conditions. Conversely, class 170: tree cover - flooded, saline water increased by 148.4%, reflecting changes in flood dynamics or the expansion of saline water coverage.

The "Bare & Built-up" category demonstrates a significant increase especially in class 190: urban areas, starting from zero in the "before" classification and becoming a prominent LC type in the "after" classification. This highlights the rapid pace of urbanization and infrastructure development globally. Meanwhile, class 200: bare areas experienced a sharp decrease of 68.3%, suggesting that previously bare areas were converted to other LC types.

Lastly, under the "Water & Snow" category, class 210: water bodies, shows a notable decrease at a rate of 40.7%, while class 220: permanent snow and ice, exhibits a drastic reduction to none. The complete loss of permanent snow and ice highlights the impact of climate change and warming temperatures on cryospheric regions.

Although some classes, such as class 140: lichens and mosses, class 190: urban areas, and class 220: permanent snow and ice, show complete increases or decreases between the "before" and "after" classifications, further analysis using the transition matrix is necessary. This detailed examination helps understanding the specific transitions between classifications and the underlying factors driving these changes.

4.2.2 ESA CCI LC transition matrix

	Class_10	Class_20	Class_30	Class_40	Class_50	Class_60	Class_70	Class_80	Class_90	Class_100	Class_110	Class_120	Class_130	Class_140	Class_150	Class_160	Class_170	Class_180	Class_190	Class_200	Class_210	Class_220
Class_10	0	0	0	0	8591	19220	3487	671	1665	7396	422	5304	10264	0	1875	673	356	95	82764	1150	2175	0
Class_20	0	0	0	0	239	735	93	29	10	530	29	200	1193	0	1319	6	224	0	30471	287	758	0
Class_30	0	0	0	0	45101	21142	2755	875	3758	10113	225	5149	7144	0	618	1027	517	12	8609	119	881	0
Class_40	0	0	0	0	24499	42085	8303	1711	3632	25530	299	5963	13842	0	1574	1574	426	58	6622	362	1014	0
Class_50	28734	624	39110	37904	0	0	0	0	0	22628	1116	25210	3998	0	1692	0	0	4262	711	61	1725	0
Class_60	26147	1536	13914	19990	0	0	0	0	0	25929	2912	76839	11996	0	646	0	0	6373	3068	464	1140	0
Class_70	15702	506	9253	13330	0	0	0	0	0	81287	9534	66907	18073	0	40559	0	0	26458	3447	8817	17948	0
Class_80	2654	33	1391	5151	0	0	0	0	0	28924	14710	41378	9471	0	6825	0	0	5225	244	5909	1205	0
Class_90	4563	151	1146	1411	0	0	0	0	0	11134	863	5218	1792	0	1002	0	0	2857	209	250	339	0
Class_100	2559	194	1541	3236	3868	8061	10832	9589	1601	0	2923	15329	5312	0	3277	622	21	2280	6262	415	350	0
Class_110	3468	934	712	2720	501	4913	7732	7374	171	8435	0	913	0	0	6035	162	18	53	1192	1141	154	0
Class_120	30876	1008	11730	9396	19275	54940	14758	13126	2109	30870	953	0	3759	0	933	1425	262	181	7863	540	1313	0
Class_130	23897	9485	10119	23190	2250	13877	6448	6029	955	16169	0	3767	0	0	61534	497	47	222	16297	13343	2802	0
Class_140	0	0	0	0	0	0	0	0	0	0	0	0	0	0	0	0	0	0	2	0	0	0
Class_150	25648	2602	8086	12874	133	2566	24733	26624	848	21923	11360	2505	105638	0	0	1042	42	926	2658	26765	1601	0
Class_160	2359	26	1979	1290	0	0	0	0	0	3752	47	2239	482	0	1008	0	0	1536	168	132	855	0
Class_170	345	103	227	206	0	0	0	0	0	146	16	142	100	0	20	0	0	123	284	11	779	0
Class_180	246	11	76	153	2222	7877	45201	6535	3498	23520	362	1703	544	0	572	3546	160	0	1081	23	4237	0
Class_190	0	0	0	0	0	0	0	0	0	0	0	0	0	0	0	0	0	0	0	0	0	0
Class_200	6713	8485	893	2044	29	293	465	495	23	461	1202	150	63978	0	141416	28	15	3	7704	0	3819	0
Class_210	2859	611	443	462	1443	910	9558	1730	502	1095	368	2281	3473	0	4466	1379	4129	19467	1803	15731	0	0
Class_220	0	0	0	0	0	0	0	0	0	0	0	0	0	0	0	0	0	0	1	0	0	0

Area in Sq. Km. < 1000 Meters

Figure 4.5: ESA CCI LC classification disturbed areas transition matrix. The transition matrix, presented in sq. km, highlights areas less than 1,000 sq. km in gray, with aggregated classes color-coded as follows: agriculture (yellow), forest (green), grass and shrubs (light green), flooded vegetation (blue-green), bare and built-up (orange), and water and snow (light blue), as discussed in Section 2.2.

The transition matrix in Figure 4.5 provides a detailed representation of LCC, displaying transitions of the before classifications represented by horizontal cells (rows) and the after classifications represented by vertical cells (columns). To emphasize significant changes, cells in the matrix with an area size of 1000 sq. km or less are highlighted with a gray background, indicating insignificant changes. This visualization allows for a clearer understanding of the most notable LC transitions during the study period.

The transition matrix as seen in Figure 4.5 reveals several notable patterns. Class 140: lichens and mosses and class 220: permanent snow and ice have their values reduced to zero in the after classification, indicating a significant loss of these LC types. In contrast, class 190: urban areas shows a value of zero in the before classification, reflecting its absence initially. However, it displays significant values in the after classification, highlighting the expansion of built-up areas and the decline in the other natural LC types. Interestingly, within the aggregated classification types of agriculture and forests, there are no observed transitions between individual classes, with the exception of class 100: mosaic tree and shrub (>50%). This suggests that these categories remained relatively stable during the study period, with minimal transitions within the same aggregated category.

The analysis of the transition matrix further identifies the top 10 most significant LCC:
Top 1: Class 200: Bare areas to Class 150: Sparse vegetation (<15%)
Top 2: Class 150: Sparse vegetation (<15%) to Class 130: Grassland
Top 3: Class 10: Rainfed Cropland to Class 190: Urban areas
Top 4: Class 70: Tree cover-Evergreen Needleleaf to Class 100: Mosaic tree and shrub
Top 5: Class 60: Tree cover-Deciduous Broadleaf to Class 120: Shrubland
Top 6: Class 70: Tree cover-Evergreen Needleleaf to Class 120: Shrubland
Top 7: Class 200: Bare areas to Class 130: Grassland
Top 8: Class 130: Grassland to Class 150: Sparse vegetation (<15%)
Top 9: Class 120: Shrubland to Class 60: Tree cover-Deciduous Broadleaf
Top 10: Class 180: Flooded Shrub/Herbaceous cover to Class 70: Tree cover-Evergreen Needleleaf

Among these, the most substantial overall changes occurred in class 100: mosaic tree and shrub, class 150: sparse vegetation (<15%), and class 130: grassland, all of which belong to the aggregated classification type "Grass & Shrubs". This indicates that the aggregated class type "Grass & Shrubs" experienced the highest amount of disturbance and transformation globally, indicating its vulnerability to LCC during the study period. Additionally, class 190: built-up areas stand out as a significant class transition, ranking fourth among the highest overall changes that occurred in a class transition. The increase in built-up areas aligns with trends of urban expansion and infrastructure development and is consistent with the patterns displayed in Figure 4.4. The dominant conversion of different classes towards class 190 in the "after" classification further emphasizes the global trend toward urbanization and its impact on natural LC types.

This comprehensive analysis of the transition matrix, combined with insights from Figure 4.4, provides a nuanced understanding of global LCC. It highlights key areas of disturbance, identifies vulnerable LC types, and offers a foundation for further exploration into the drivers of these transitions.

4.3 Combined land cover and land surface temperature results

4.3.1 Undisturbed areas LST

4.3.1.1 Timeline 1: LST whole period

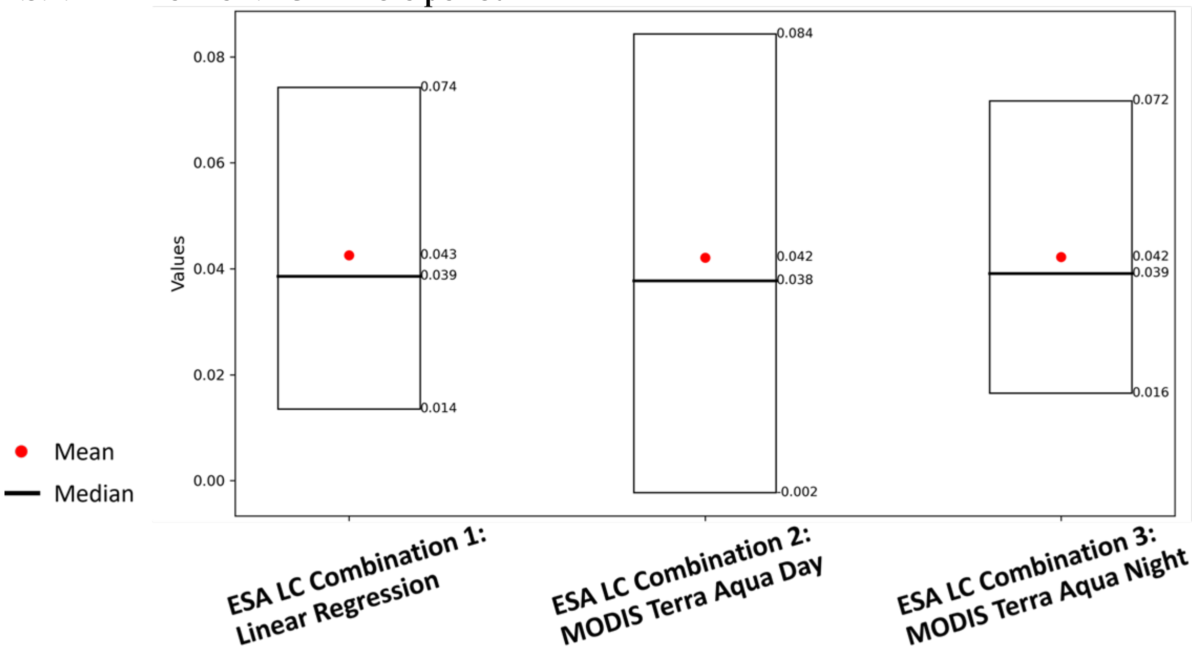

Figure 4.6: Undisturbed areas summary: linear trend LST (timeline 1: whole period). The figure represents a box plot that illustrates the minimum, maximum, mean (indicated by a red dot), and median (indicated by a horizontal line) for three combinations of MODIS LST data: combination 1: linear regression, combination 2: MODIS terra aqua day, and combination 3: MODIS terra aqua night, as described in Section 3.1.4. This visualization provides a statistical summary of the computed LST linear trend values derived from the IQR-filtered data for timeline 1: LST Whole Period.

The box plot results are based on LST data (linear trend) extracted using the undisturbed mask (with values 1) applied globally. For combination 1, the extracted LST values range from 0.014 to 0.074, with a mean of 0.043 and a median of 0.039. For combination 2, the values range from 0.002 to 0.084, with a mean of 0.042 and a median of 0.038. Lastly, for combination 3, the LST values range from 0.016 to 0.072, with a mean of 0.042 and a median of 0.039. A comparison of the three combinations reveals that the differences in their mean and median values are within ±0.001, indicating minimal variation in the extracted LST values for undisturbed areas across the three combinations. This consistency suggests that the choice of combination has little impact at the overall LST trends for undisturbed regions.

It is notable that combination 2: MODIS terra aqua day exhibits the largest variability among the three, reflecting greater fluctuations in daytime LST observations. On the other hand, combination 3: MODIS terra aqua night shows the lowest variability which aligns with the study conducted by Zhang et al. (2016) findings that nighttime observations tend to be more stable and lower RMSE (Zhang et al., 2016). The stability in nighttime observations underscores its reliability for studies that focus on long-term LST trends. Lastly, the mean values derived from these combinations serve as a reference to compensate for LST variability caused by factors other than LCC transitions.

4.3.1.2 Timeline 2: LST difference

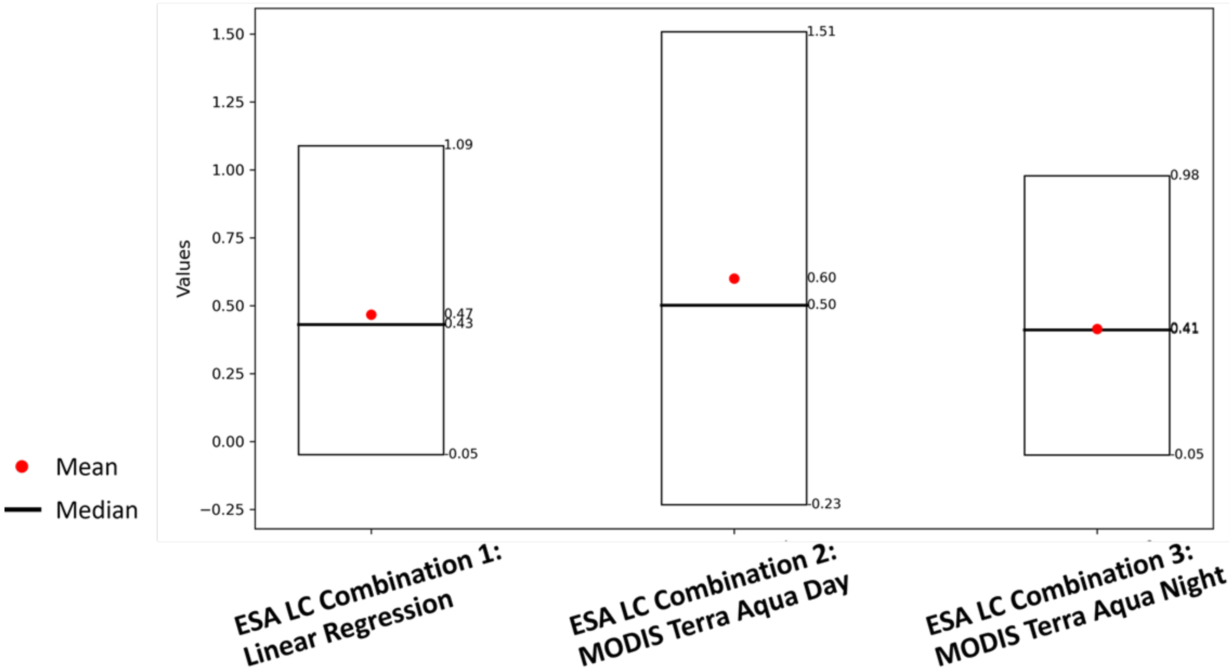

Figure 4.7: Undisturbed areas summary: difference of the mean LST (timeline 2: LST difference). The figure represents a box plot that illustrates the minimum, maximum, mean (indicated by a red dot), and median (indicated by a horizontal line) for three combinations of MODIS LST data: combination 1: linear regression, combination 2: MODIS terra aqua day, and combination 3: MODIS terra aqua night, as described in Section 3.1.4. The visualization provides a statistical summary of the computed LST linear trend values derived from the IQR-filtered data for Timeline 2: LST Difference.

The box plot results are based on LST data (LST Difference) extracted using the global undisturbed mask (with values "1"). For combination 1, the extracted LST values range from 0.05 to 1.09, with a mean of 0.47 and a median of 0.43. For combination 2, the values range from 0.23 to 1.51, with a mean of 0.60 and a median of 0.50. Lastly, for combination 3, the LST values range from 0.05 to 0.98, with a mean and median of 0.41. It can be observed that the results of the combination 1 derived using the linear regression equation have almost similar results to the combination 3 derived using the simple average of MODIS terra aqua nighttime observations. On the other hand, combination 2 derived using the simple average of MODIS terra aqua daytime observation exhibits the largest variability that includes outlier values among the three combinations. The increased variability in combination 2 suggests that there is a distinct impact of LST for undisturbed areas during daytime observations.

The findings of Zhang et al. (2016) regarding the variability of MODIS daytime observations support these results, as daytime products tend to exhibit higher variability compared to their nighttime counterparts (Zhang et al., 2016). The stability observed in both combination 1 and combination 3 makes them more suitable and reliable for temporal studies, where consistency and accuracy are critical. The mean values calculated from these combinations were utilized to compensate for LST variability caused by factors unrelated to LCC transitions.

4.3.2 Disturbed areas of LST per LCC

4.3.3 LST per transition summary: LST whole Period and LST difference

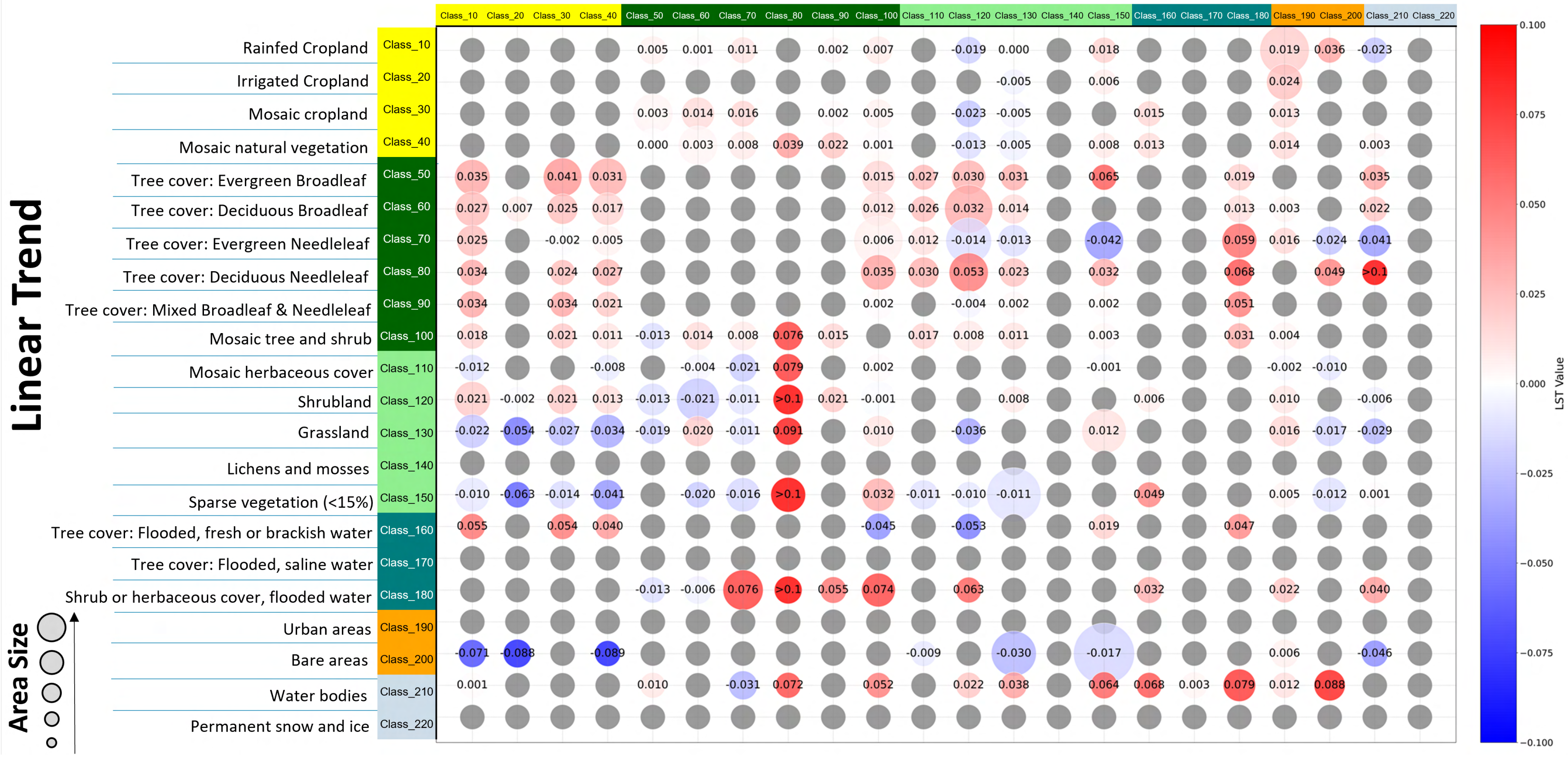

Figure 4.8: ESA CCI LC and linear trend LST (timeline 1) transition matrix bubble plot (combination 1: linear regression equation). The figure contains a transitional matrix bubble plot where the bubble represents the size, the color represents the temperature, before classes are along the horizontal axis, and after classes are along the vertical axis.

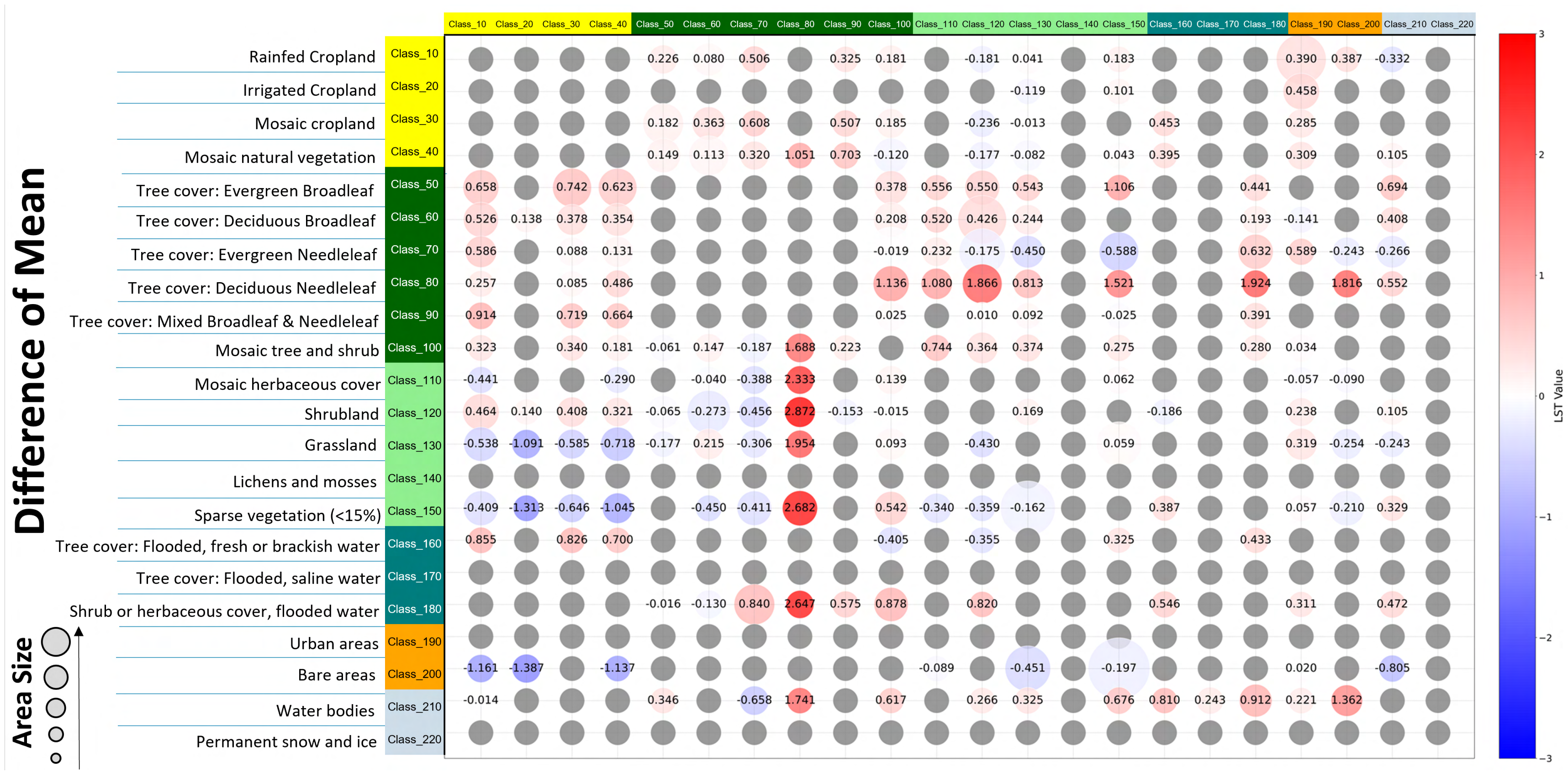

Figure 4.9: ESA CCI LC and difference of mean LST (timeline 2) transition matrix bubble plot (combination 1: linear regression equation). The figure contains a transitional matrix bubble plot where the bubble represents the size, the color represents the temperature, before classes are along the horizontal axis, and after classes are along the vertical axis.

The Figure 4.8 and Figure 4.9 are illustrated as a transitional matrix bubble plot. In these plots, the size of each bubble corresponds to the area size, while the color of the bubble represents temperature changes with blue indicating cooling and red indicating warming and its selected range of temperature change values is between -0.100 to 0.100 for linear trend LST (timeline 1) and -3 to 3 for difference of mean LST (timeline 2). Areas that are deemed irrelevant specifically those with sizes less than 1,000 sq. km are excluded from the display as a gray bubble. Additionally, the "before" classes are represented along the horizontal axis or rows, while the "after" classes are shown along the vertical axis or columns.

The Figure 4.8, which displays and utilizes the LST - linear trend derived from the entire period, and Figure 4.9, which displays and utilizes the LST - difference of the mean calculated using the start and end periods as discussed in Section 3.1: Timeline and study area, show similar patterns of temperature increases and decreases across almost all class transitions. When examining the aggregated LC classification types: agriculture (yellow), forest (green), grass and shrubs (light green), flooded vegetation (blue-green), bare and built-up areas (orange), and water and snow (light blue) several notable patterns emerge.

The first key observation is that the transition from the aggregated agricultural type to forest type classes has led to a minimal increase in temperatures, which contradicts the expected outcome of a temperature decrease. The unexpected result suggests the presence of complex interactions between classes or other influencing factors in these LC transitions or LST, which was examined in greater detail in the discussion at the next section. Secondly, the transition from agriculture to grass and shrubs has resulted in cooling of LST. However, an exception was observed in class 150: sparse vegetation where this transition led to a temperature increase. Third, the conversion of the agricultural type classes to urban and bare areas class resulted in an overall increase in temperature, with the transitions of the class to bare areas exhibits a more notable warming effect on the LST. Finally, the transition from agricultural areas to water bodies consistently led to cooling, aligning with expectations due to the thermal properties of water.

The next key observation shows that the majority of the transition originating from the aggregated forest type towards other aggregated classification types resulted in an increase in temperatures. However, a notable exception is observed within the forest type classification, specifically class 70: tree cover - evergreen needleleaf. Transitions from this class to other classes, including class 120: shrubland, class 130: grassland, class 150: sparse vegetation, and class 200: bare areas, resulted in cooling rather than warming in LST. The increase in LST outcomes is contrary to expectations and highlights the need to investigate the possible reasons behind these anomalies. These complexities are explored further in the next chapter during the discussion.

Coming from the aggregated classification type "Grass & Shrubs", it can be observed that the majority of transitions have resulted in cooling. However, a notable exception is the conversion from all classes under "Grass & Shrubs" to class 80: tree cover - deciduous needleleaf, which has shown an increase in temperature. Additionally, the transition from class 120: shrubland to agricultural type predominantly resulted in a temperature increase. However, exceptions were observed in transitions to class 110: mosaic herbaceous cover, class 130: grassland, and class 150: sparse vegetation, resulting in cooling. Lastly, it is worth noting that certain transitions of within the "Grass & Shrubs" type have led to both increases and decreases in temperature across various classes, which suggests that these classes may exhibit distinct and independent behaviors.

Within the bare and built-up classes, class 190: urban areas does not show any transitions originating from other classes in the before classes due to its area size. However, transitions leading to class 190: urban areas in the after classes have relevant area size and predominantly resulted in an increase in temperature. On the other hand, class 200: bare areas displays transitions from various before classes, all of which have resulted in cooling across all aggregated LC classification types. In contrast, transitions toward class 200: bare areas exhibited more varied outcomes, particularly in cases involving class 70: tree cover - evergreen needleleaf and the aggregated classification type "Grass & Shrubs". These varying results highlight the complexity of interactions within these transitions, suggesting that different LC types influence temperature changes in diverse ways.

The final notable observation is the transitions originating from the before classes to class 210: water bodies, which have predominantly resulted in an increase in temperature, except for class 70: tree Cover - evergreen needleleaf, which exhibited cooling. Conversely, the transitions toward class 210 in the "after" classes mostly led to cooling. A notable exception is class 80: tree cover - deciduous needleleaf, which showed an increase in temperature.

In summary, the analysis of LC transitions and their associated LST changes has revealed both expected and unexpected patterns, underscoring the complexity of these relationships. While some transitions align with expectations, some anomalies such as the aggregated agriculture type, class 70: tree Cover - evergreen needleleaf, which consistently demonstrates cooling in its transitions before and after, and class 80: tree cover - deciduous needleleaf, which consistently exhibits warming in its transitions, highlight the complexities between LC and LST, thus requiring the need for further investigation, which are examined in greater detail in the discussion of the subsequent section.

4.3.4 Linear trend LST comparison of day and night

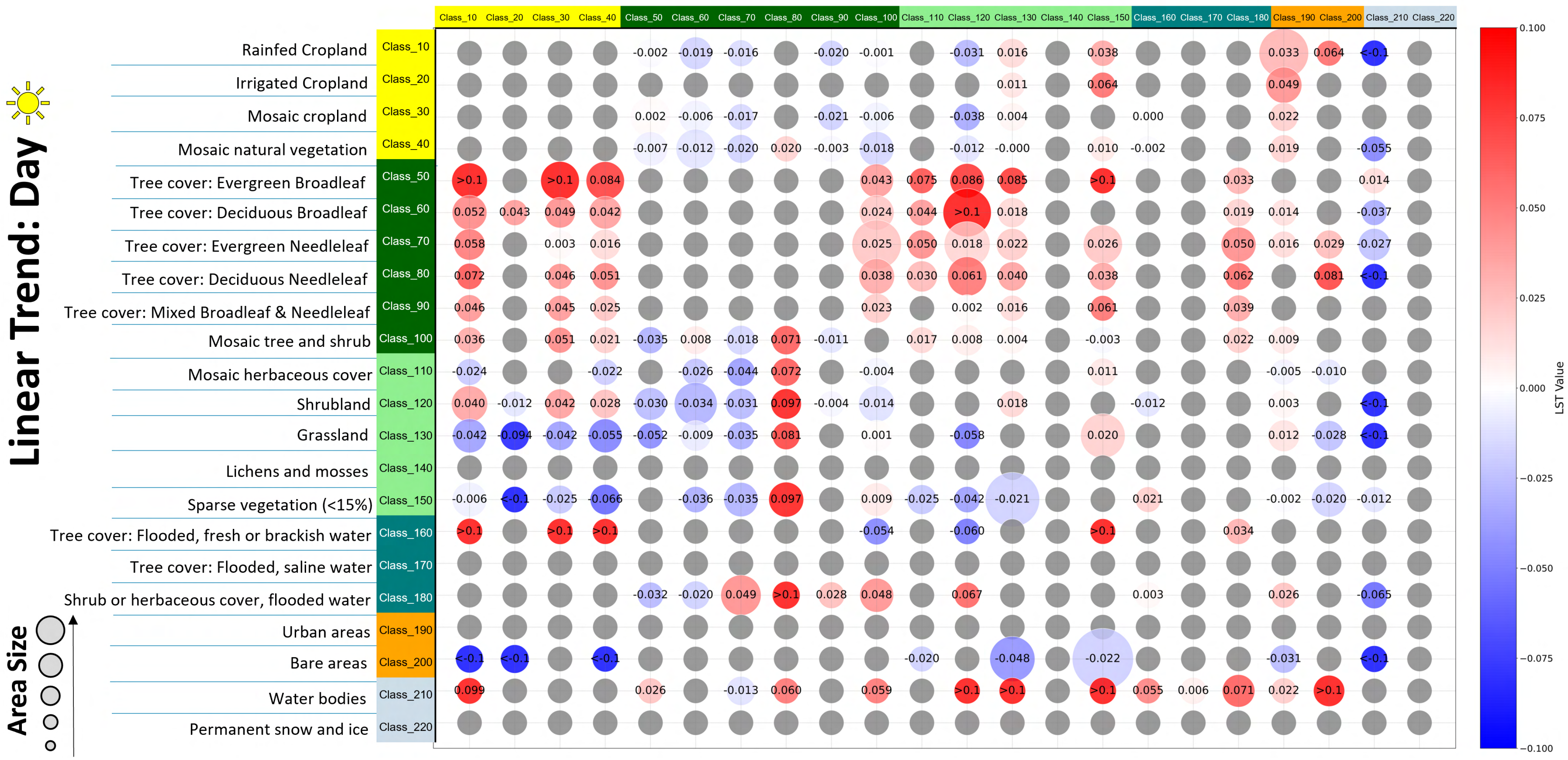

Figure 4.10: ESA CCI LC and linear trend LST (timeline 1) transition matrix bubble plot (combination 2: average of terra aqua day). The figure contains a transitional matrix bubble plot where the bubble represents the size, the color represents the temperature, before classes are along the horizontal axis, and after classes are along the vertical axis.

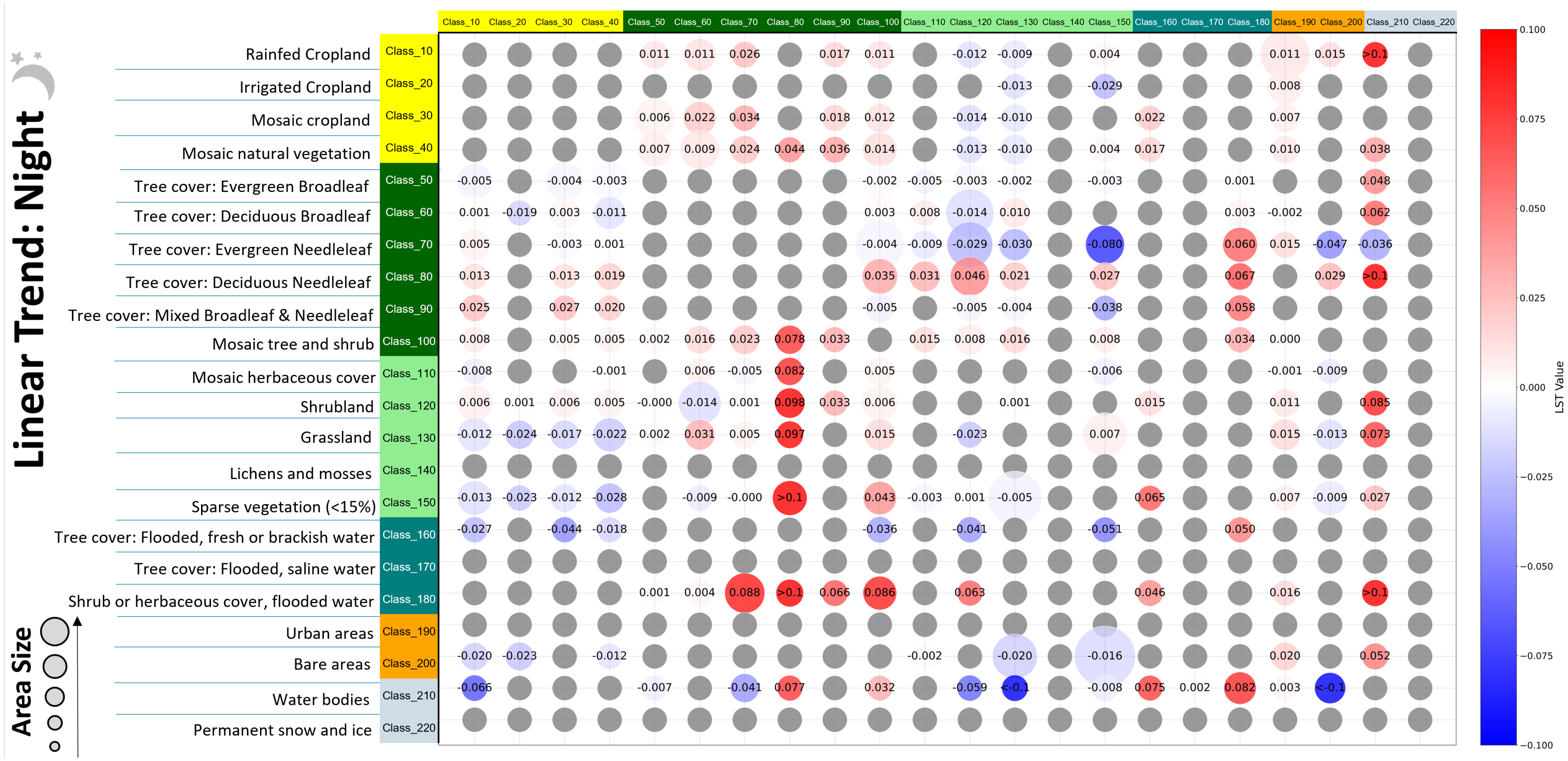

Figure 4.11: ESA CCI LC and linear trend LST (timeline 1) transition matrix bubble plot (combination 3: average of terra aqua night). The figure contains a transitional matrix bubble plot where the bubble represents the size, the color represents the temperature, before classes are along the horizontal axis, and after classes are along the vertical axis.

The Figure 4.10 and Figure 4.11 are illustrated as a transitional matrix bubble plot. In these plots, the size of each bubble corresponds to the area size, while the color of the bubble represents temperature changes with blue indicating cooling and red indicating warming and its selected range of temperature change values is between the minimum value of -0.100 and maximum value 0.100. Areas that are deemed irrelevant specifically those with sizes less than 1,000 sq. km are excluded from the display as a gray bubble. Additionally, the "before" classes are represented along the horizontal axis or rows, while the "after" classes are shown along the vertical axis or columns.

For the comparison of the day and night transition matrix bubble plots, the study used the linear trend LST from timeline 1: whole period to ensure long-term stability and to identify the trend of mean annual LST values. Based on Figure 4.10 and Figure 4.11, the quantified LST results for day and night differ significantly from each other. The results show that daytime LST values exhibit higher variability, with more extreme cooling and warming trends, while nighttime LST values demonstrate less variability, reflecting a more stable temperature pattern. The observed variability in disturbed LC transitions affecting LST during the day and night aligns with the patterns observed in undisturbed LC transitions discussed in Section 3.2.2: Combination of the MODIS products, Zhang et al. (2016) highlighted in their study that daytime LST typically exhibits greater variability than nighttime LST (Zhang et al., 2016). However, this does not necessarily guarantee that nighttime results are more accurate than those from daytime measurements. To further compare the results, the three combinations were analyzed: combination 1 (linear regression equation), combination 2 (average of terra and aqua day), and combination 3 (average of terra and aqua night).

Table 4.1: Tabulated results of the LST pattern using the three combinations. The table displays the tabulated LST patterns in each three combinations, with 1 indicating an increase, 0 indicating no change, -1 indicating a decrease. These values shows the average of all values within the intersection of the aggregated LC classifications.

Category		Agriculture	Forest	Grass & Shrubs	Flooded Vegetation	Bare & Built-up	Water & Snow
Agriculture	Linear Reg. Eq.	0	0	1	1	1	0
	Average Day	0	-1	1	-1	1	0
	Average Night	0	1	-1	1	1	0
Forest	Linear Reg. Eq.	1	0	1	0	1	0
	Average Day	1	0	1	0	1	0
	Average Night	1	0	-1	0	1	0
Grass & Shrubs	Linear Reg. Eq.	-1	-1	0	1	-1	0
	Average Day	-1	-1	0	-1	-1	0
	Average Night	-1	1	0	1	-1	0
Flooded Vegetation	Linear Reg. Eq.	1	0	1	0	1	0
	Average Day	1	0	1	0	1	0
	Average Night	-1	0	-1	0	1	0
Bare & Built-up	Linear Reg. Eq.	0	0	0	0	0	0
	Average Day	0	0	0	0	0	0
	Average Night	0	0	0	0	0	0
Water & Snow	Linear Reg. Eq.	0	0	0	0	1	0
	Average Day	0	0	0	0	1	0
	Average Night	0	0	0	0	-1	0

Based on Figure 4.1, it can be observed that combination 1 (linear regression equation) and combination 3 (average terra and aqua night) show similar cooling and warming patterns, particularly in long-term trends, indicating consistency in nighttime temperature behavior. Conversely, combination 2 (average terra and aqua day) demonstrates greater variability, leading to distinct patterns, especially in the aggregated classification types "Agriculture" and "Forests". Additionally, it can be observed that the expected results from the combination 2 (average terra and aqua day) are more accurate than the expected results. This variability reflects the dynamic heating and cooling processes during the day, which are influenced by multiple factors such as solar radiation, vegetation cover, and land use.

There are many similarities that can be observed on the three combinations especially for the aggregated classification type "Agriculture, "Forests" and "Grass & Shrubs". On the other hand, all three combinations show similar LST patterns in the aggregated classification types "Flooded Vegetation", "Bare & Built-up", and "Water & Snow". The consistency suggests that these LC types exhibit more stable LST behavior regardless of the combination or time of observation. The differences in patterns between the three combinations can be attributed to the varying quantified LST values for each LC transition, which display unique behaviors during the day and night due to diurnal temperature fluctuations.

These findings highlight the need for further studies to determine the most reliable representation of LST for different applications. Although nighttime observations provide stability and lower variability, daytime measurements capture dynamic temperature changes that may be critical for certain analyses. Therefore, selecting the most suitable LST combination requires careful consideration of the research objectives, the temporal scale, and the specific characteristics of the LC being studied.

4.3.5 Top 50 LST per transition summary of the LST difference (Area x LST)

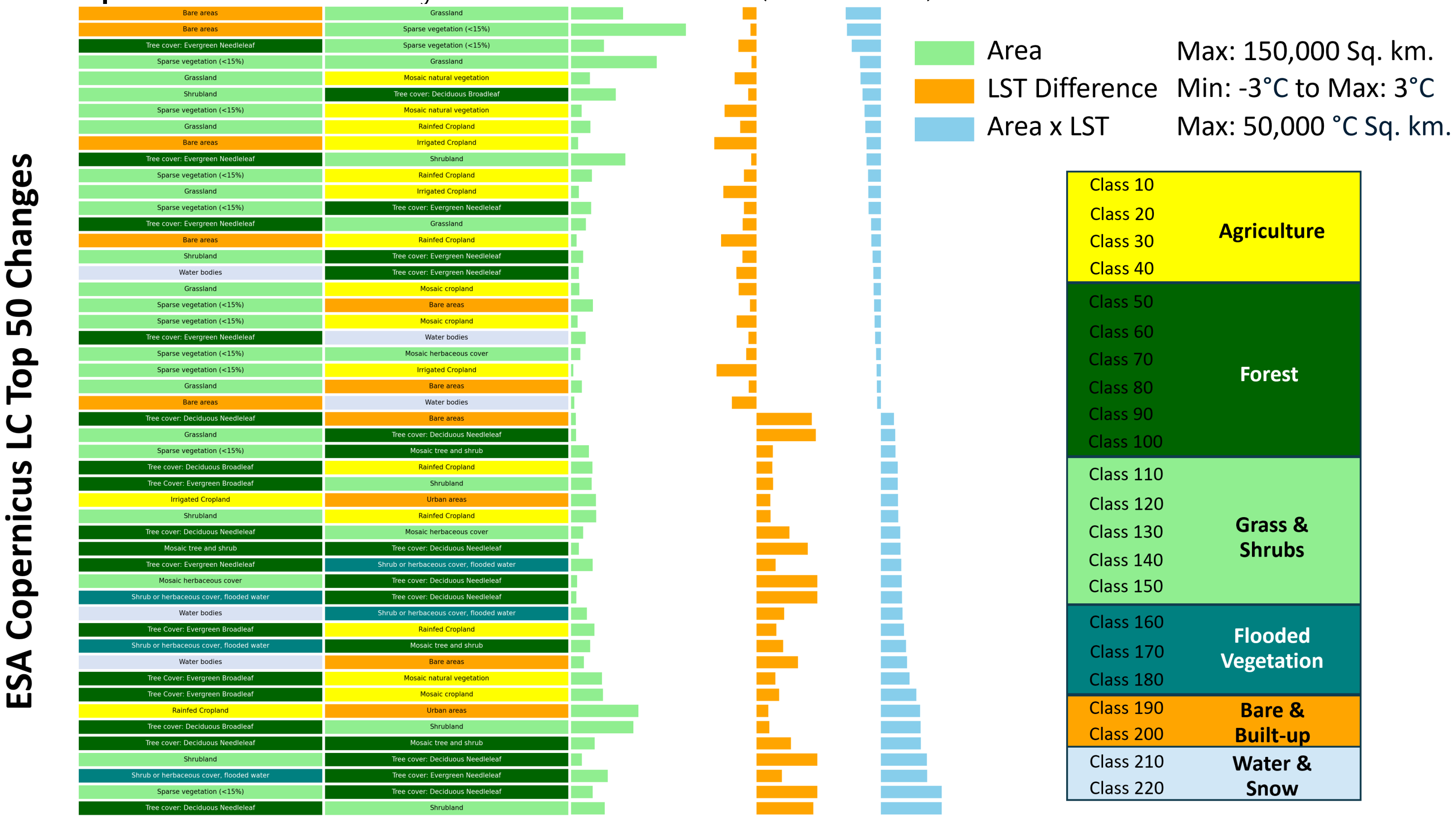

Figure 4.12: ESA CCI LC - LST (Area x LST): Top 50 summary of changes using the area and the difference of mean LST. The figure represents the top 50 LC and LST changes computed using (Area X LST).

The figure presents the top 50 LC and LST changes which is ranked by multiplying the area size by the LST difference and filtering the results from the lowest to the highest values. The chart consists of five columns: the first column represents the "before" classification, the second column represents the "after" classification, the third column shows the area size, the fourth column displays the LST difference, and the fifth column highlights results of the Area x LST.

One of the key insights from Figure 4.12 is that the chart reveals distinct patterns in the transitions that contribute to cooling and warming. In the cooling (upper) part of the chart, most of the transitions originate from "Grass & Shrubs" being converted to "Agriculture". Conversely, in the warming (lower) part of the chart, "Forests" are predominantly being converted to other classes. It can be observed that LST impacts associated with specific transitions between aggregated LC classification types reveal distinct and notable patterns.

Transitions from "Bare & Built-up" to "Grass & Shrubs" consistently result in cooling, indicating that shifts toward vegetated areas can lower LST. Similarly, the transitions from "Grass & Shrubs" to "Agriculture" and from "Grass & Shrubs" to "Forests" also show a cooling effect, further emphasizing the role of vegetation in mitigating global temperature increases. On the other hand, transitions from "Forests" to "Agriculture" and from "Forests" to "Grass & Shrubs" are associated with warming, suggesting that the reduction of forest cover contributes to increased LST. Additionally, transitions from "Flooded Vegetation" and "Water & Snow" to "Forests" and "Agriculture" result in warming, highlighting the sensitivity of these LC types to changes in water availability and their impact on LST. These observations highlight the intricate relationship between LCC transitions and their impact on LST dynamics, emphasizing the need for further analysis to better understand the factors driving these patterns.

In summary, the top 50 transitions mostly align with expected results, with two notable exceptions. class 70: tree Cover - evergreen needleleaf consistently results in cooling LST, whether it is in "before" or "after" transitions and class 80: tree cover - deciduous needleleaf exclusively exhibits warming LST in both its before and after class transitions, both of which are contrary to expectations. The unexpected results from these transitions further emphasize the complexity of LC and LST relationships and would require additional exploration in the subsequent sections.

4.3.6 Top 10 quantified transitions of the LC-LST relationship

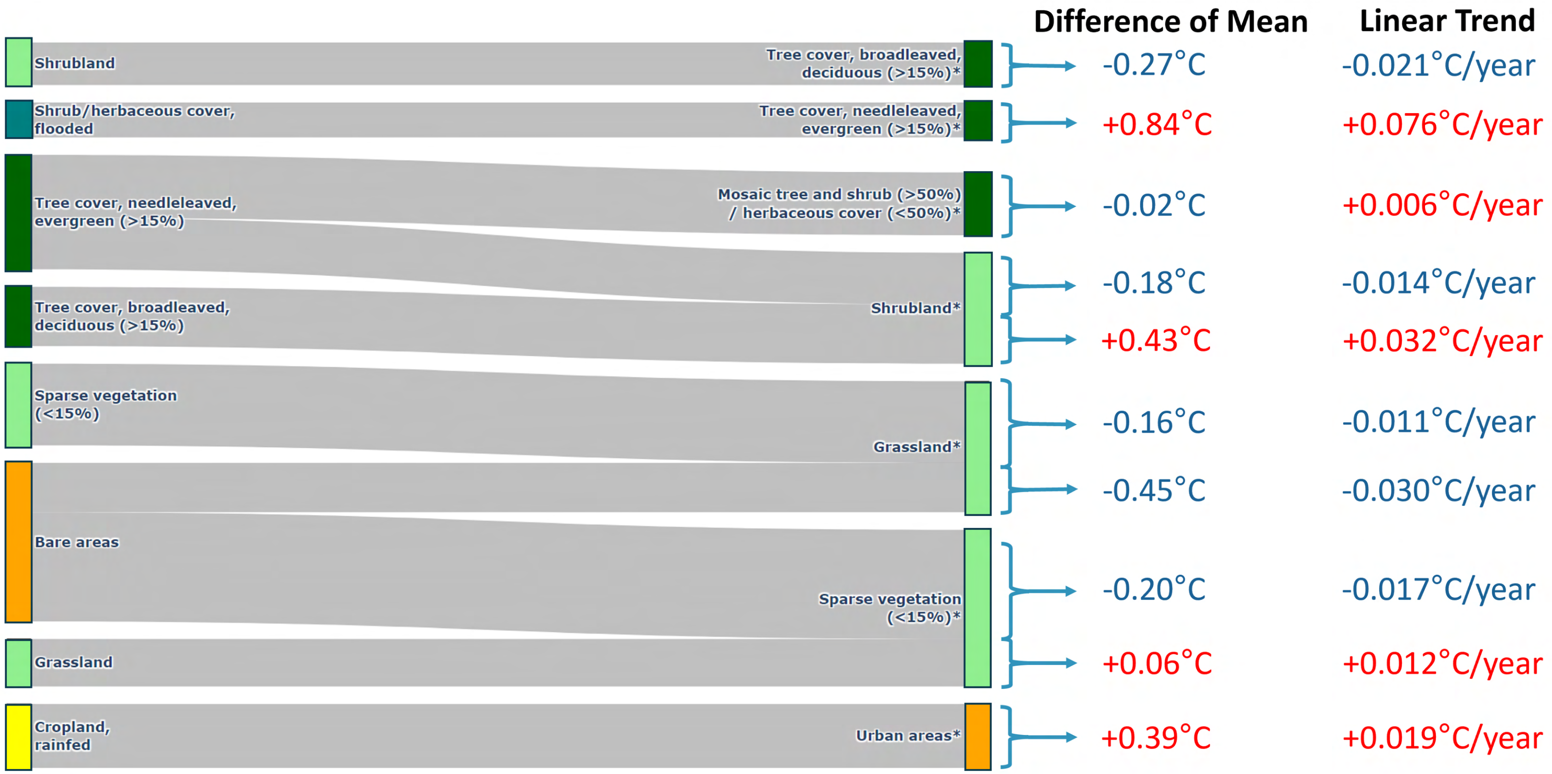

Figure 4.13: Quantified LC-LST sankey diagram of top 10 changes using the two timelines. The figure displays a sankey diagram of the top 10 LCC transitions along with the linear trend LST - timeline 1 (right) and the difference of mean LST - timeline 2 (left).

The figure provides a detailed representation of the quantified LST changes resulting from LCC transitions highlighting the top 10 LCC transitions, visualized through a sankey diagram. In this diagram, the thickness of each flow represents the area size associated with a specific LCC transition, offering a clear visual indicator of the relative scale of each transition. There are two columns that provide additional quantified data on the right side of the sankey diagram. The first column displays the LST differences calculated from timeline 2, which represents the change between the start and end periods. The second column presents the LST values derived from timeline 1, which reflects the whole period's linear trend.

Class 120: shrubland transitioning to class 60: tree Cover - deciduous broadleaf has resulted in a temperature decrease of $-0.27°C$, with a cooling rate of $-0.021°C/year$. The cooling effect on LST aligns with expectations, as the transition from the aggregated type "Grass & Shrubs" which typically has lower thermal absorption, towards the aggregated type "Forests" which has higher vegetation density that promotes reduced temperatures.

Class 180: shrub or herbaceous cover, flooded Water transitioning to class 70: tree cover - needleleaf evergreen has resulted in a temperature increase of $+0.84°C$, with a warming rate of $+0.076°$ $C/year$. This transition exhibits the most significant increase in both LST difference and LST linear trend within the top 10 LCC transitions. The significant warming may be attributed to the LC characteristics of class 180 which includes not only shrub or herbaceous cover but also flooded water. The reduction of water bodies and replacement with needleleaf forests likely leads to higher surface heating resulting in the temperature increase.

Class 70: tree cover - needleleaf evergreen transitioning to class 100: mosaic tree and shrub has resulted in a slight temperature decrease of $-0.02°C$, with a warming rate of $+0.006°C/year$. It is notable that the difference of mean LST (timeline 2) and LST linear trend LST (timeline 1) exhibit opposing effects, with one showing cooling and the other warming. However, the overall temperature change is minimal, indicating a balance within the same aggregated classification type under "Forests", where structural changes in the vegetation property may play a subtle role.

Class 70: tree cover - needleleaf evergreen transitioning to class 120: shrubland has resulted in a temperature decrease of $-0.18°C$, with a cooling rate of $-0.014°C/year$. The unexpected cooling effect is inconsistent with other results, as deforestation typically leads to warming. Further analysis is required to understand why this transition results in cooling. One possible explanation could involve the influence the neighboring temperatures or the specific characteristics of the selected pixels within class 70. The unexpected results was examined in greater detail in the subsequent chapter.

Class 60: tree Cover - broadleaf deciduous transitioning to Class 120: shrubland has resulted in a temperature increase of $+0.43°C$, with a warming rate of $+0.032°C/year$. Unlike the transition from class 70 to class 120, this result aligns with expectations, as deforestation leads to warming in temperatures. This transition is the second-highest contributor to increases in both difference of mean LST (timeline 2) and linear trend LST (timeline 1) among the top 10 LCC transitions, emphasizing the significant impact of deforestation.

Class 150: sparse Vegetation transitioning to class 130: grassland has resulted in a temperature decrease of $-0.16°C$, with a cooling rate of $-0.011°C/year$. The transition within the same aggregated classification type under "Grass & Shrubs" should be minimal, however, results show otherwise. Grasslands typically retain more moisture than sparse vegetation, which likely explains the observed reduction in temperature.

Class 200: bare areas transitioning to class 130: grassland have resulted in a temperature decrease of $-0.45°C$, with a cooling rate of $-0.030°C/year$. This transition demonstrates the most substantial cooling in both difference of mean LST (timeline 2) and linear trend LST (timeline 1) among the top 10 LCC transitions. The shift from bare areas which retain less moisture as compared to grasslands which retain significantly more moisture and support cooling through evapotranspiration is a key driver of this significant decrease in LST.

Class 200: bare areas transitioning to class 150: sparse vegetation has resulted in a temperature decrease of $-0.20°C$, with a cooling rate of $-0.017°C/year$. This transition has the largest area size among the top 10 transitions, as indicated by the flow thickness in the sankey diagram. Similar to the transition from class 200: bare areas to class 130: grassland, the increase in vegetation density, moisture and cooling through evapotranspiration probably contributes to the observed cooling effect.

Class 130: grassland transitioning to class 150: sparse vegetation has shown a slight temperature increase of $+0.06°C$, with a warming rate of $+0.012°C/year$. The minimal change in LST suggests a balance in the transition within the same aggregated classification type under "Grass & Shrubs", with sparse vegetation reflecting slightly higher solar radiation and retaining less moisture compared to grasslands.

Class 10: cropland, rainfed transitioning to class 190: urban areas has resulted in a temperature increase of $+0.39°C$, with a warming rate of $+0.019°C/year$. The conversion from the agricultural type croplands towards urban areas represents the third-highest increase in both difference of mean LST (timeline 2) and linear trend LST (timeline 1) within the top 10 LCC transitions. The warming effect is expected, as urban areas retain more heat and have a lower albedo compared to croplands. Additionally, it is notable that this transition ranks among the top 10 LC changes out of 484 class transitions globally, highlighting the impact of urbanization on local and global temperature dynamics.

The results reveal a diverse range of temperature impacts, with cooling LST effects commonly observed in transitions involving increased vegetation density - such as from bare areas to grasslands. Conversely, warming effects are notable in transitions involving deforestation or urbanization, such as from tree cover to shrubland or croplands to urban areas. The most substantial temperature increases and decreases underscore the critical role of vegetation, moisture retention, and land surface properties in regulating LST. However, some unexpected results such as the cooling effect in the transition from class 70: needleleaf evergreen forests to class 120: shrubland were observed. This transition highlight the complexity of LCC transitions and the influence of additional factors like neighboring pixel interactions or local conditions. These anomalies were explored further in the subsequent discussion to better understand the driving mechanisms behind these LC changes and their equivalent LST.

4.3.7 Disturbed areas LST of overall LCC

4.3.7.1 Timeline 1: LST whole period

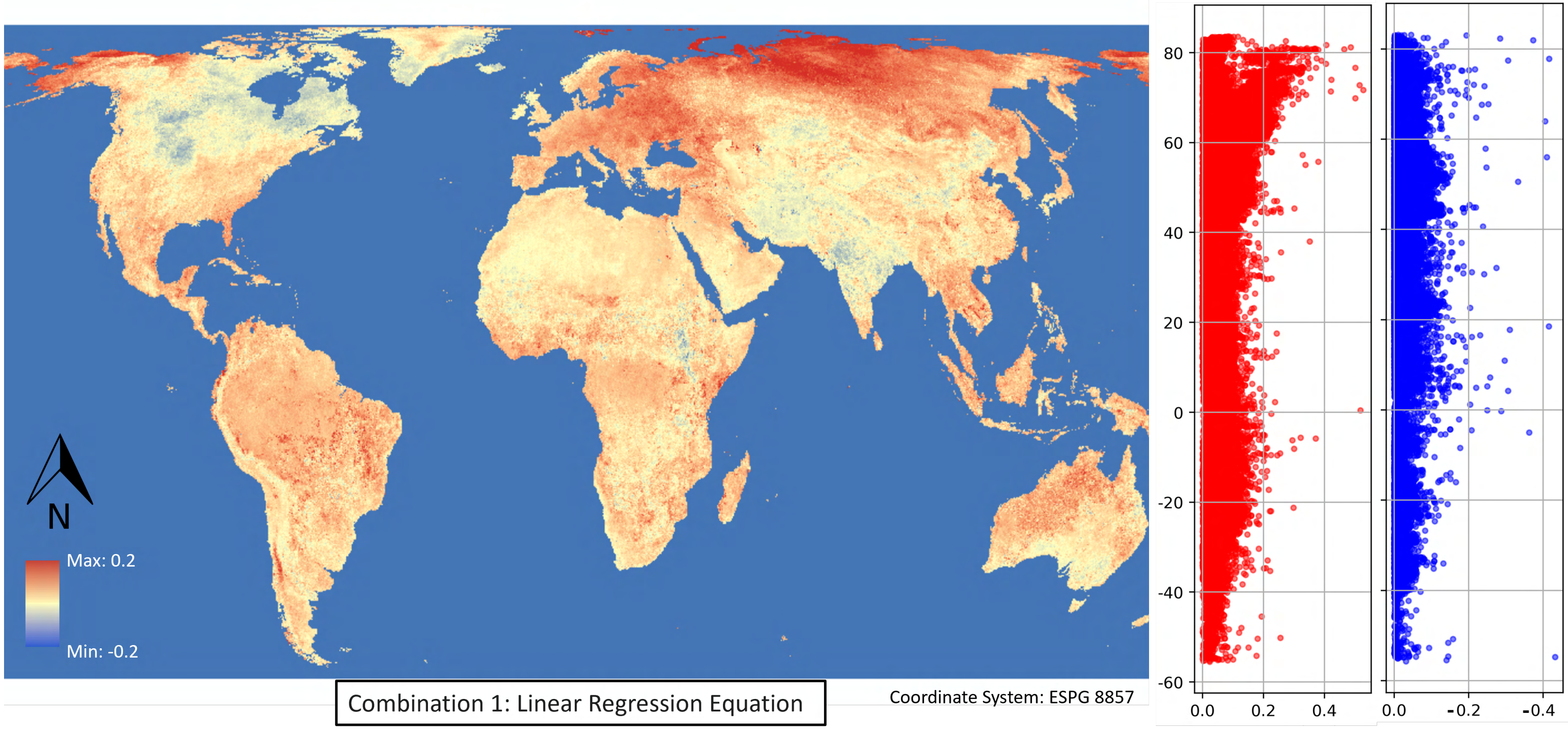

Figure 4.14: Scatter plot distribution of values: linear trend LST (timeline 1: whole period). The figure contains a global LST map with a scatter plot distribution of warming and cooling at 20 degree intervals. The map was generated using ESRI ArcMap software (version 10.8)

The visualization consists of a global LST map paired with a scatter plot, which depicts the distribution of warming and cooling points across latitudes. The scatter plot contains two columns: the first column represents warming, and the second column represents cooling, based on 50,000 randomly selected points from global data. The latitude range is divided into 20-degree intervals to provide a clearer view of the spatial LST trends.

The scatter plot distribution and the global LST map from Figure 4.14 reveal distinct patterns in warming and cooling. Cooling appears more prominent in the northern regions above the equator (between 0° and 90°N) compared to other areas such as the southern hemisphere below the equator. Conversely, warming is more notable in the southern hemisphere (0° to -20°S) and in the northern polar regions (60° to 90°N).

The warming areas on the LST map are particularly pronounced in the tundra regions of northern Russia and Alaska in the United States, reflecting significant increase in temperature in these areas. In contrast, the LST distribution in northern Africa appears more uniform, with minimal notable warming or cooling trends. A slight warming trend can also be observed in European regions, parts of Asia, northwestern Australia, and Brazil. On the other hand, significant cooling is evident in regions such as Canada, Greenland, and a slight increase in some parts of India.

4.3.7.2 Timeline 2: LST difference

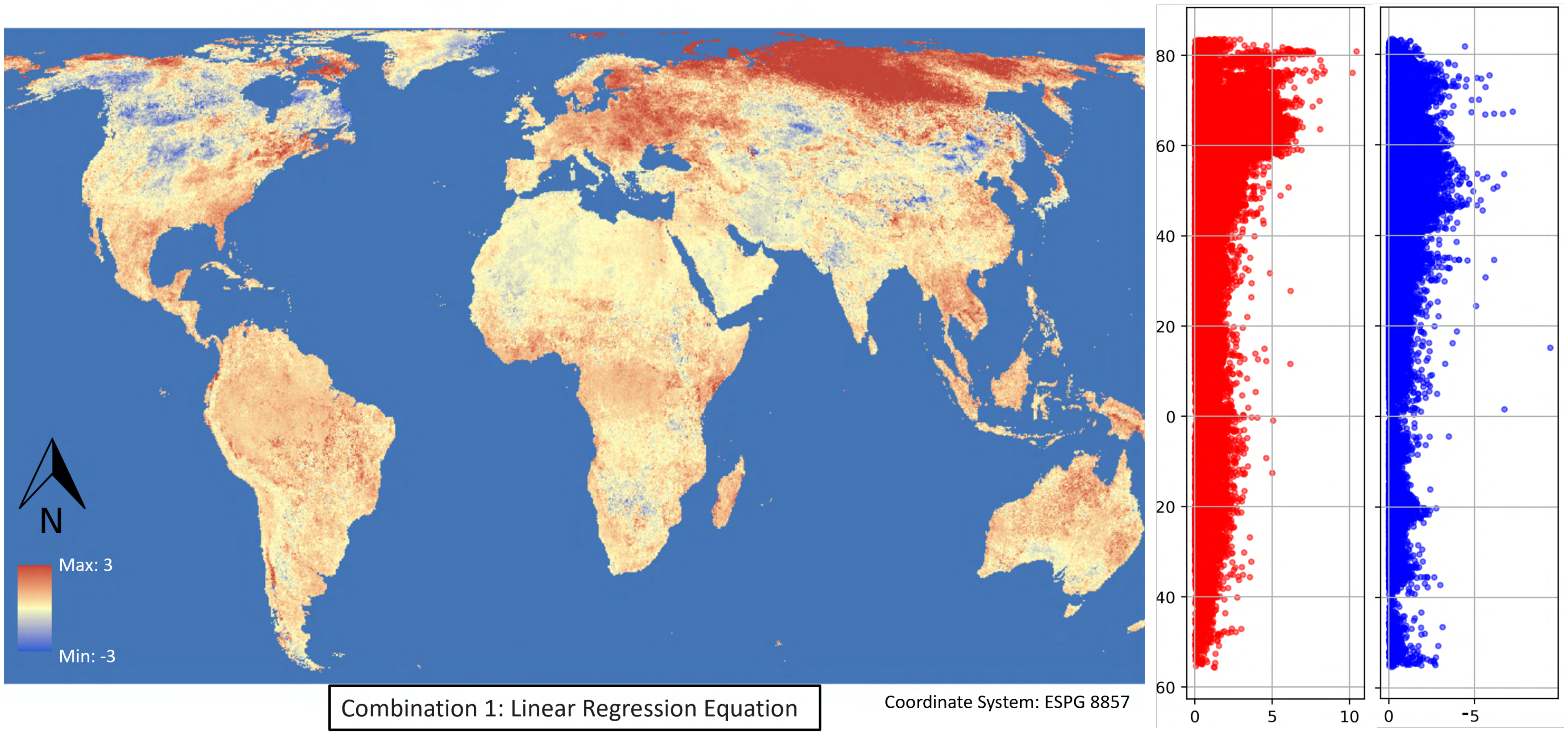

Figure 4.15: Scatter plot distribution of values: Difference of the mean LST (timeline 2: LST difference). The figure contains a global LST map with a scatter plot distribution of warming and cooling at 20 degree intervals. The map was generated using ESRI ArcMap software (version 10.8)

Similar to Figure 4.14, the visualization consists of a global LST map paired with a scatter plot, which depicts the distribution of warming and cooling points across latitudes. The scatter plot contains two columns: the first column represents warming, and the second column represents cooling, based on 50,000 randomly selected points from global data. The latitude range is divided into 20-degree intervals to provide a clearer view of the spatial LST trends.

The scatter plot distribution and the global LST map from Figure 4.15 reveal a more distinct patterns in warming and cooling as compared to Figure 4.12. However, cooling appears more prominent in the northern regions (between 40° and 90°N) compared to other areas such as the southern hemisphere below (below 40°). On the other hand, warming is more notable in the southern hemisphere (0° to -20°S) and in the northern polar regions (60° to 90°N).

Similar to Figure 4.14, the warming areas in the LST map are particularly pronounced in the tundra regions of northern Russia and parts of northern Canada, reflecting significant temperature increases in these areas. Additionally, the LST distribution in northern Africa also appears more uniform in Figure 4.15, with minimal notable warming or cooling trends. A slight warming trend can also be observed in European regions, parts of Asia, northwestern Australia, and Brazil. In contrast, significant cooling is evident in regions such as Canada, Greenland, kazakstan, northeast part of china, and a slight increase in some parts of India.

These cooling trends are clearly reflected in the scatter plot in both Figure 4.14 and Figure 4.15, which corresponds accurately with the global LST map. The visual alignment between the scatter plot and the map enhances the credibility of the analysis, showing consistent spatial trends in both warming and cooling across various regions of the globe. Overall, Figure 4.14 and Figure 4.15 highlights the global variability of LST changes over the whole period and effectively demonstrates the spatial and latitudinal patterns of warming and cooling, providing valuable insights into regional warming and cooling of LST dynamics.

4.3.7.3 Global disturbance

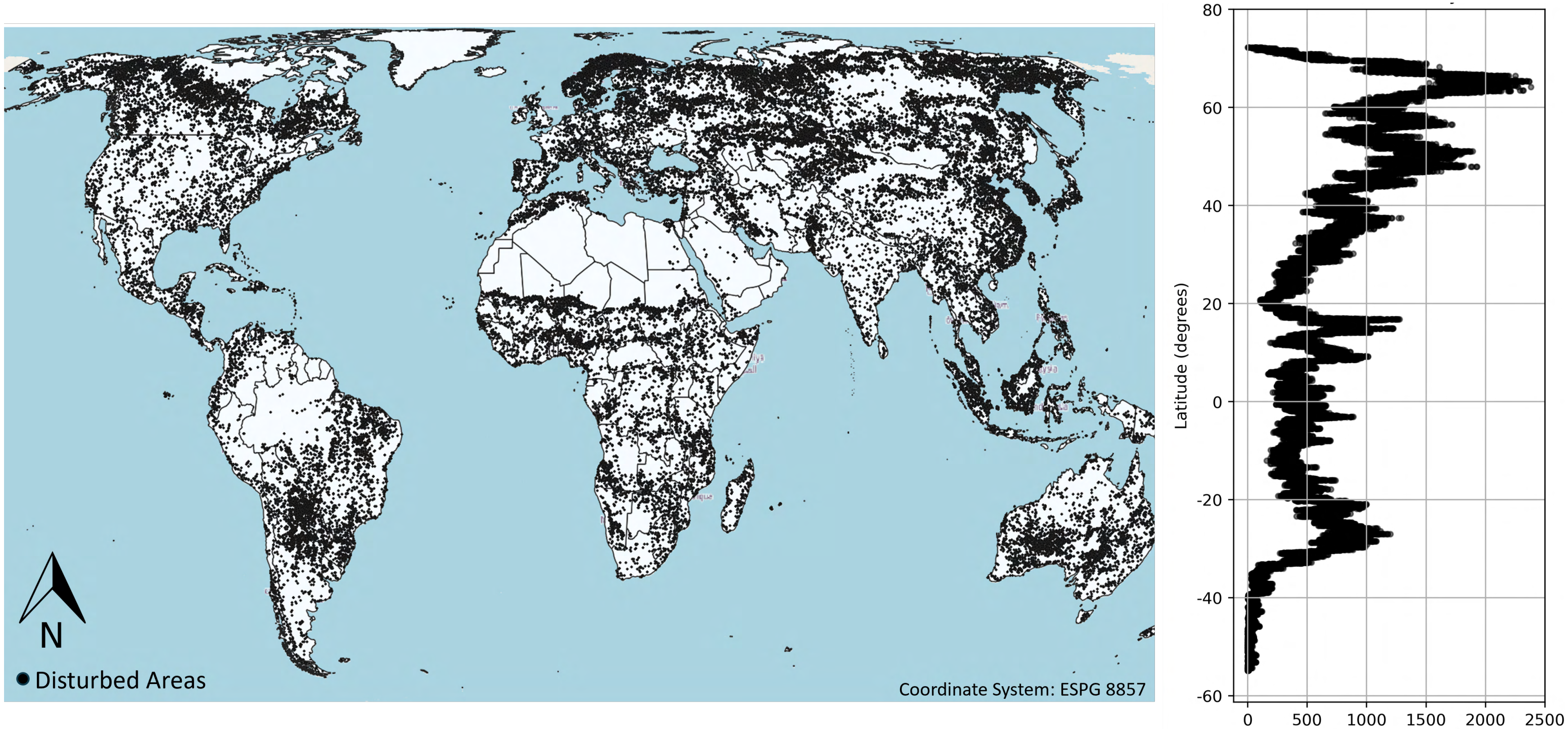

Figure 4.16: Scatter plot distribution of the global disturbed LC pixels. The figure illustrates the global distribution of disturbance pixels with a scatter plot distribution across latitudes, divided into 20-degree intervals. The map and the basemap were generated using QGIS desktop software (version 3.32.3).

Figure 4.16 illustrates the global distribution of disturbance pixels, representing points that experienced transitions from one LC class to another. The visualization includes both a global map of disturbances and a scatter plot distribution of disturbance points across latitudes, divided into 20-degree intervals. This scatter plot provides a clear overview of the spatial extent and intensity of disturbances in different regions.

The analysis of disturbance pixels between start period and the end period reveals that disturbances are predominantly concentrated in specific regions. Significant disturbances are observed in mid-Canada, Norway, Sweden, western and eastern Russia, western China, Korea, Japan, Indonesia, the southern part of Australia, and mid-Argentina. These regions reflect areas with notable LC transitions during the studied period, likely due to factors such as deforestation, agricultural expansion, or urbanization.

In contrast, regions such as Greenland, the Queen Elizabeth Islands in northern Canada, northwestern Brazil, northern Africa, and the Middle East exhibit little to no disturbances. These areas either experienced minimal LCC or remained relatively stable during the studied timeframe. Additionally, minimal disturbances are observed in northern Australia, parts of western and central Asia, and mid-regions of China, further highlighting regions of stability or less dynamic LC transitions.

Overall, Figure 4.16 provides a comprehensive spatial overview of LCC disturbances, offering insights into the regions with significant changes and those with minimal or no changes.

4.4 Local samples of LCC and LST relationship

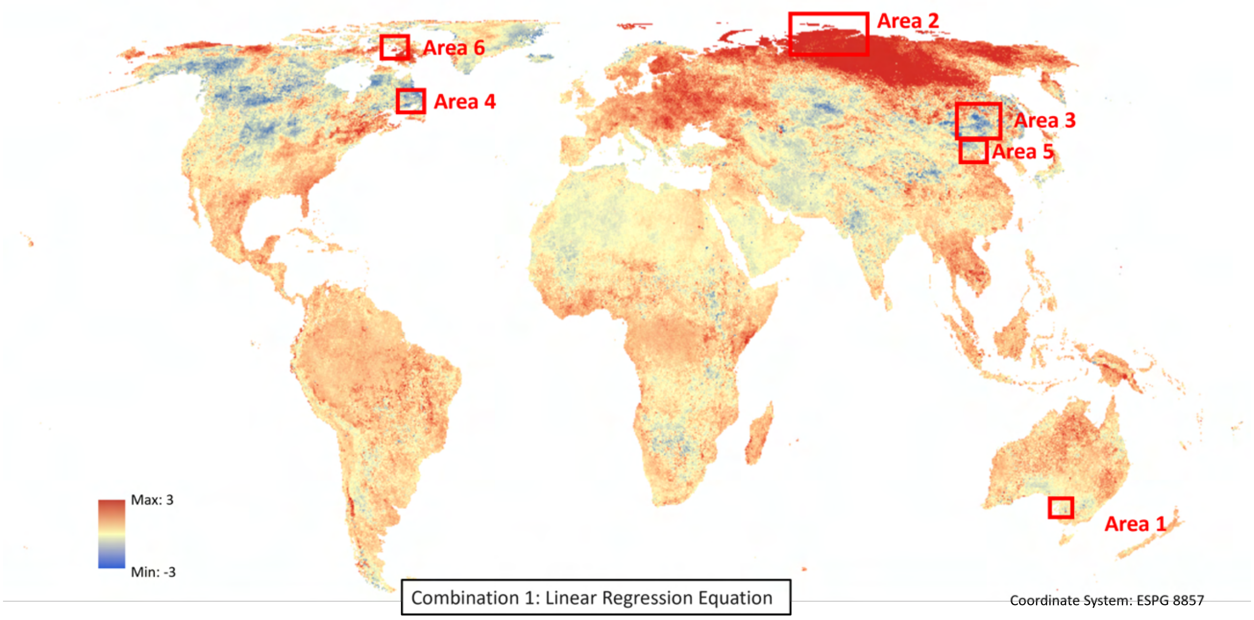

Figure 4.17: Global summary of the sampled areas for visualization of the LCC and LST relationship. The figure highlights the locations of six carefully selected sample areas marked with red rectangular boxes using the LST map. The map was generated using ESRI ArcMap software (version 10.8).

The LST map in Figure 4.17 was created using combination 1: linear regression equation to visualize the global patterns of overall warming and cooling in LST. The figure highlights the locations of six carefully selected sample areas marked with red rectangular boxes to provide a detailed visualization of the relationship between LCC and LST in regions exhibiting significant warming or cooling. These areas were chosen to offer insight into the dynamics of LC transitions and their impact on LST.

The first sample area is located in Australia which is selected as a result of its small yet noticeable cooling effect. The second area is situated in the tundra region of northern Russia, a region displaying some of the most significant global warming trends. The third area is located in the northwest part of China which was selected to explore the notable cooling observed. Similarly, the fifth area is also located in China specifically in Beijing where rapid urbanization has led to significant warming effects. Lastly, the fourth and sixth areas are located in Canada, with the fourth area exhibiting significant cooling and the sixth area exhibiting substantial warming.

In the subsequent figures, the satellite imagery of these six sample areas are presented, including "before" and "after" views of LC and LST. This detailed comparison helps provide a deeper understanding of the transitions occurring in these regions and their relationship to changes in LST. Zooming in on these selected areas with notable warming and cooling offers a more focused perspective, enabling a better understanding of the complex interactions between LCC and LST. This localized approach could help assess how specific LC transitions influence the LST dynamics.

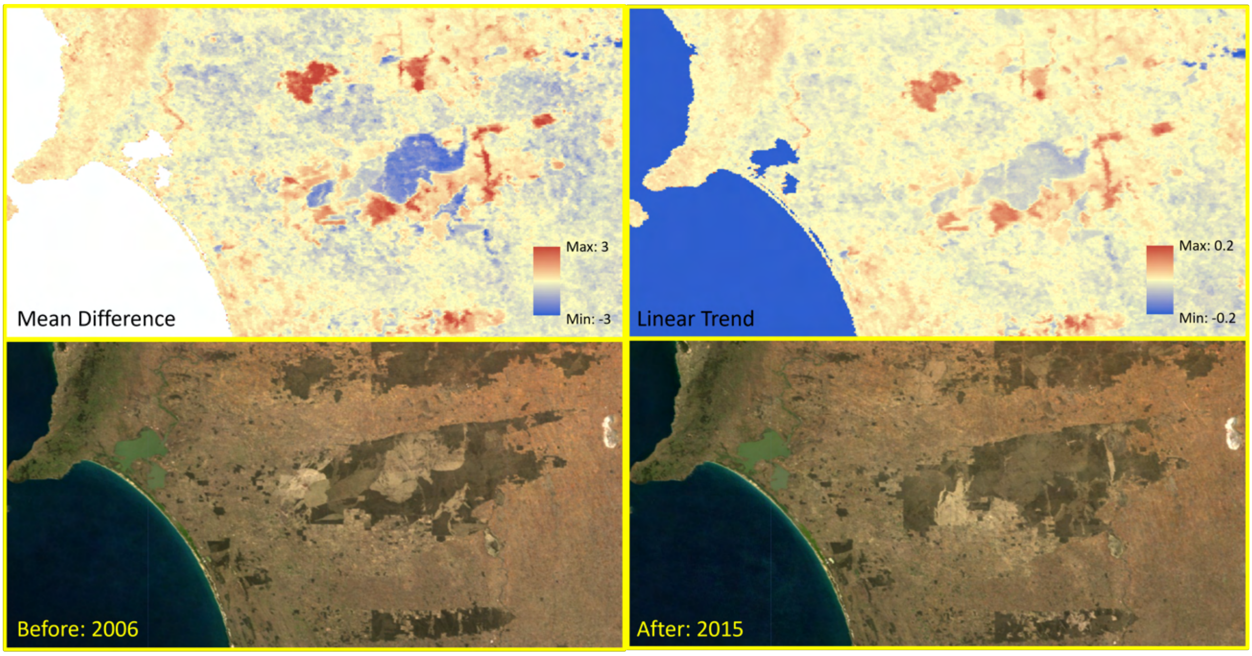

Figure 4.18: Sample area 1: Australia used for visualization of the LCC and LST relationship. The figure provides a focused view of Area 1 located in Australia. The top-left corner of the figure displays the LST visualization using the difference of mean (timeline 2): min -3°C to max +3°C, while the top-right corner presents the linear trend LST (timeline 1): min -0.2°C to max +0.2°C. The bottom-left corner shows the "Before" MODIS satellite RGB image mosaicked for the year 2006, and the bottom-right corner displays the "After" MODIS satellite RGB image mosaicked for the year 2015. The images was generated using GEE and ESRI ArcMap software (version 10.8).

Upon examining the before and after satellite images in Figure 4.18, it is evident that a significant portion of the bare land was converted into forests, which is consistent with the surrounding areas. The transition from bare areas to forests has resulted in a significant cooling effect on LST as observed in both the difference of mean LST (timeline 2) and the linear trend LST (timeline 1) visualizations. This finding correctly corresponds to the observation that the conversion of bare areas into forests (afforestation) leads to cooling LST trends, likely due to increased vegetation cover enhancing evapotranspiration and reducing LST.

Conversely, some areas of forest located in the upper and lower portions of the figure transitioned into bare land. The LC transition from forests to bare areas demonstrates a clear warming effect as highlighted in Figure 4.18. The warming effect is consistent with the reduced vegetation cover, leading to less shading, reduced evapotranspiration, and higher LST. With this focused example, it becomes evident that the LC transitions such as from bare areas to forests and vice versa have a direct and measurable impact on LST. Forest regrowth contributes to cooling, while deforestation or the conversion to bare areas results in warming. This observation reinforces the importance of LC management in regulating local and regional climate conditions.

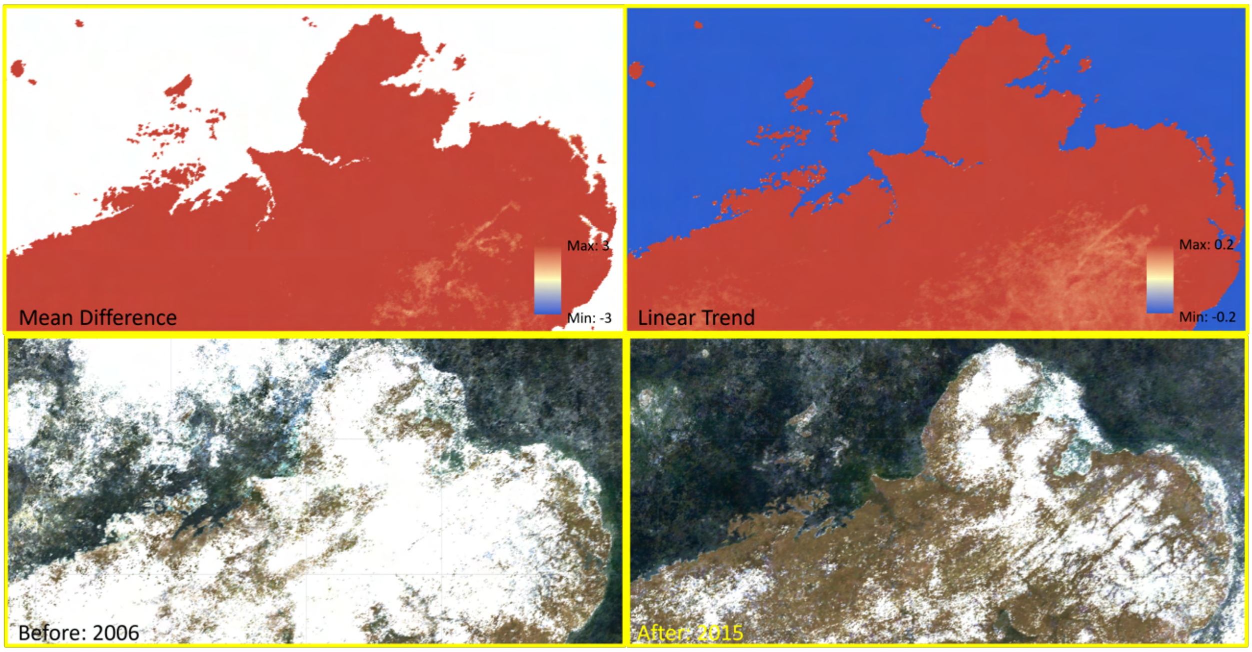

Figure 4.19: Sample area 2: Tundra in Northern Russia used for visualization of the LCC and LST relationship. The figure provides a focused view of Area 2 located in the tundra region of the northern part of Russia. The top-left corner of the figure displays the LST visualization using the difference of mean (timeline 2): min -3°C to max +3°C, while the top-right corner presents the linear trend LST (timeline 1): min -0.2°C to max +0.2°C. The bottom-left corner shows the "Before" MODIS satellite RGB image mosaicked for the year 2006, and the bottom-right corner displays the "After" MODIS satellite RGB image mosaicked for the year 2015. The images was generated using GEE and ESRI ArcMap software (version 10.8).

Based on Figure 4.19, it is evident from both the difference of the mean and linear trend visualizations that there is a significant and uniform increase in temperature throughout the tundra region. Upon closer examination of the "Before" and "After" satellite images, a notable change is observed: a significant reduction in white pixels, representing clouds, snow, and ice cover between 2006 and 2015. In the "After" image, areas of land and vegetation have become more prominent, indicating a considerable loss of snow and ice cover in this region. The transition from snow and ice to exposed land and vegetation is a key driver of the observed increase in temperature. Snow and ice surfaces, with their high albedo reflect most solar radiation which keeps the LST cool. However, as snow and ice are replaced by land or vegetation, the lower albedo of these surfaces leads to greater absorption of solar radiation contributing to a significant warming in the region. This transition highlights the critical role of snow cover in regulating local and global temperatures.

These observations in Figure 4.19 underscores the importance of addressing snow cover loss which is a direct consequence of climate change. The loss of snow and ice not only accelerates the regional warming of the LST but also contributes to global climate change that further exacerbates warming trends. The changes documented in Area 2 emphasize the urgent need for climate change mitigation and the preservation of Arctic and tundra environments to stabilize temperature increases and prevent further global impacts.

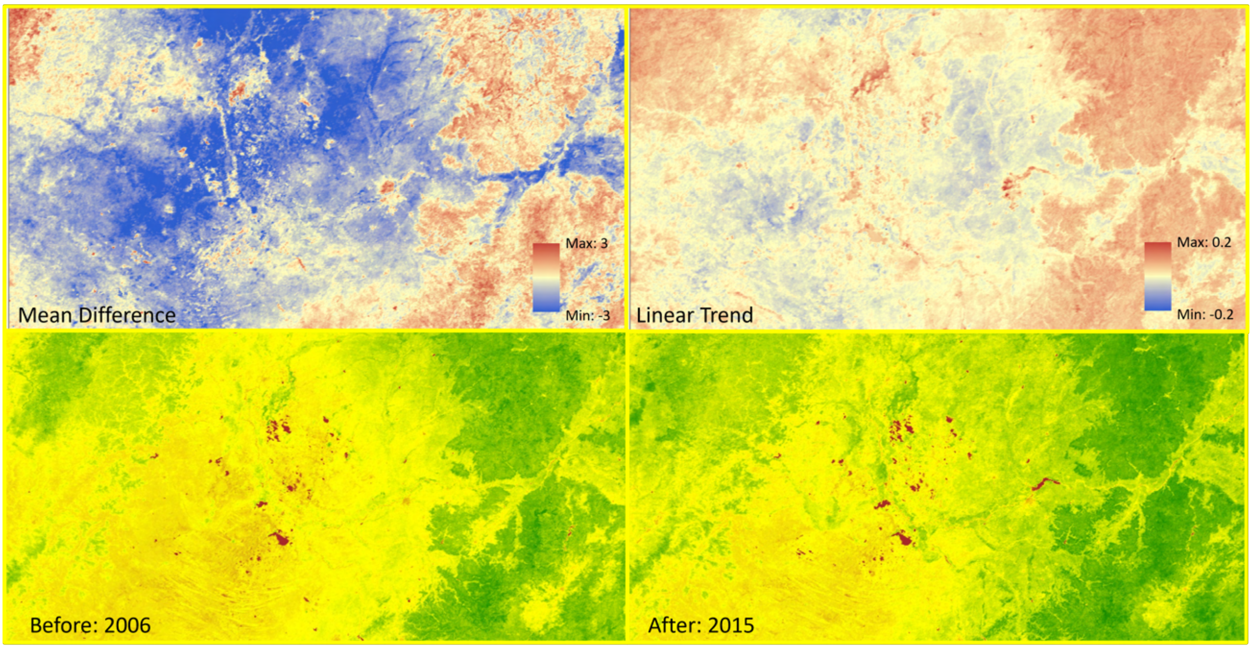

Figure 4.20: Sample area 3: Northwest of China used for visualization of the LCC and LST relationship. The figure provides a focused view of Area 3 located in northwest part of China. The top-left corner of the figure displays the LST visualization using the difference of mean (timeline 2): min -3°C to max +3°C, while the top-right corner presents the linear trend LST (timeline 1): min -0.2°C to max +0.2°C. The bottom-left corner shows the "Before" MODIS satellite NDVI image mosaicked for the year 2006, and the bottom-right corner displays the "After" MODIS satellite NDVI image mosaicked for the year 2015. The images was generated using GEE and ESRI ArcMap software (version 10.8).

Based on Figure 4.20, the region of northwest China exhibits significant cooling in the LST, as clearly observed in the difference in the mean visualization. The cooling effect is more prominently displayed in the difference of mean LST (timeline 2) compared to linear trend LST (timeline 1) which captures more subtle long-term trends. Conversely, areas of warming in the difference of mean LST (timeline 2) are less widespread but more distinct and sharply defined, while in the linear trend LST (timeline 1), warming trends appear more gradual and evenly distributed throughout the region.

A closer inspection of the Normalized Difference Vegetation Index (NDVI) images which highlight vegetation cover reveals a clear transition in LC. In the "Before" image, the region is dominated by bare soil and low vegetative areas indicated by brown hues. However, in the "After" image, these bare and low vegetative areas have significantly decreased, giving way to areas with low to mid vegetation cover. Furthermore, forested areas appear denser and greener in the "After" image, indicating an improvement in vegetation health and coverage.

Meanwhile, forest densification does not directly correlate with the observed cooling trends, the transition from bare soil and sparse vegetation to low and mid vegetative areas appears to be the primary driver of the overall cooling in the region. Vegetation contributes to cooling through processes such as evapotranspiration and increased shading, which reduce LST. The improved vegetation cover reduces the albedo effect of bare soil, balancing solar radiation absorption, and lowering LST.

In conclusion, the LCC in northwest China, particularly the reduction of bare soil and low vegetation areas and the increased in low to mid vegetation cover, have significantly contributed to observed cooling trends in the LST. This emphasizes the importance of vegetation restoration and management in mitigating regional warming and regulating LST.

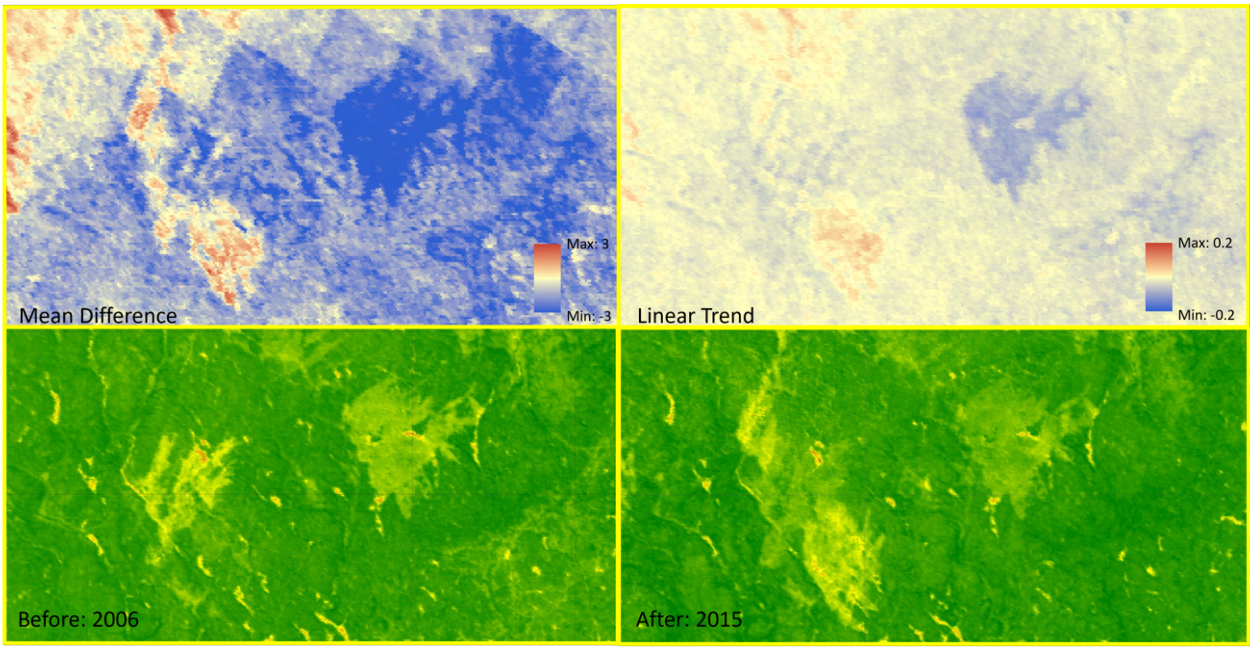

Figure 4.21: Sample area 4: Western Canada used for visualization of the LCC and LST relationship. The figure provides a focused view of Area 4 located in western Canada. The top-left corner of the figure displays the LST visualization using the difference of mean (timeline 2): min -3°C to max +3°C, while the top-right corner presents the linear trend LST (timeline 1): min -0.2°C to max +0.2°C. The bottom-left corner shows the "Before" MODIS satellite NDVI image mosaicked for the year 2006, and the bottom-right corner displays the "After" MODIS satellite NDVI image mosaicked for the year 2015.The images was generated using GEE and ESRI ArcMap software (version 10.8).

This area was selected due to its dominant cooling trend in the difference in the mean LST (timeline 2) visualization. Although the linear trend LST (timeline 1) also displays cooling in the region, the intensity and spatial extent of the cooling (represented by the blue hue) are less pronounced compared to the difference in the mean LST (timeline 2) visualization. This suggests that while the overall cooling of LST is significant, the long-term trends capture a more gradual change.

Based on Figure 4.21, the "Before" and "After" NDVI images provide insight into the LC transitions that contribute to these temperature changes. In the "Before" image, certain areas are characterized by high vegetation cover (indicated by a green hue), while others show mid-level vegetation (yellow hue). In the "After" image, areas of high vegetation can be seen transitioning to low vegetation cover (yellow hue), whereas areas of mid-level vegetation have transitioned to denser vegetation (green hue).

These LC transitions correspond directly to their respective LST changes. Transitions from high vegetative cover to low vegetative cover (green to yellow hues) are associated with warming in LST, as reduced vegetation leads to decreased evapotranspiration and increased surface heat absorption. Conversely, transitions from low vegetation to high vegetation cover (yellow to green hues) are linked to cooling in LST, as increased vegetation enhances shading and evapotranspiration, mitigating surface temperatures.

In conclusion, the observed LST cooling trends in western Canada are closely tied to LC dynamics. The transitions captured in this area underscore the significant role of vegetation in regulating surface temperatures. Although cooling trends dominate in the difference of mean LST (timeline 2), the linear trend LST (timeline 1) highlights a more nuanced picture of gradual LST variations. This analysis demonstrates the critical relationship between LC transitions and LST, emphasizing the importance of maintaining and restoring vegetation to mitigate warming effects in sensitive regions.

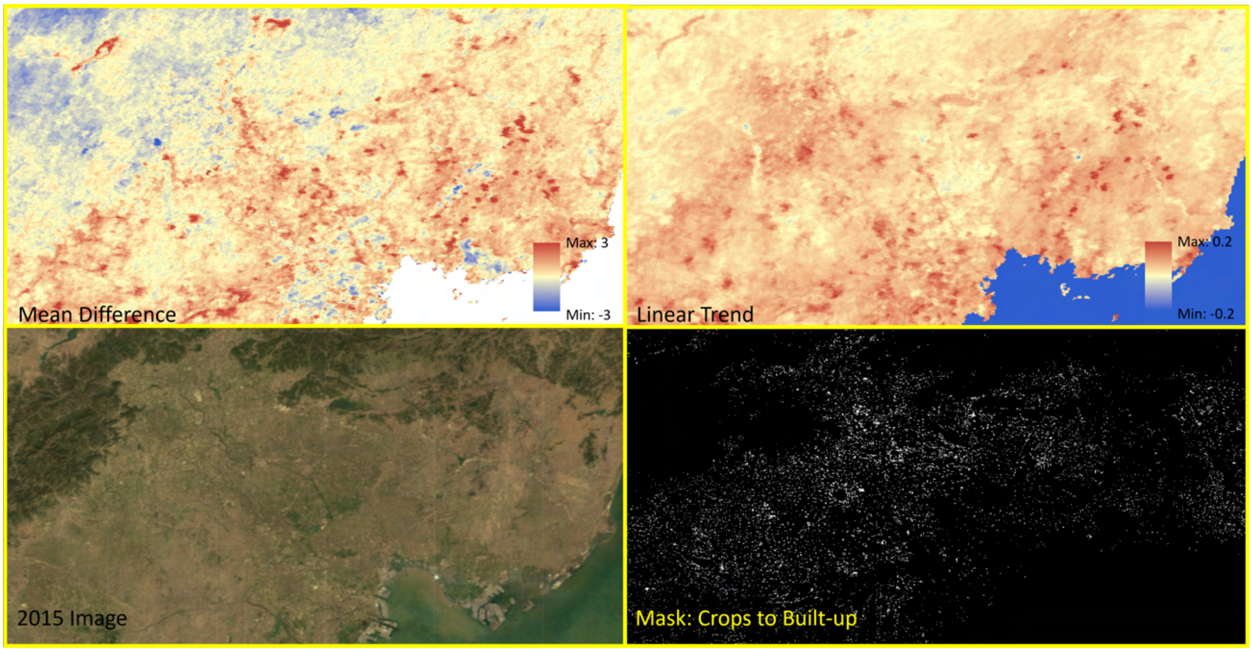

Figure 4.22: Sample area 5: Beijing, China used for visualization of the LCC and LST relationship. The figure provides a focused view of Area 5 located in Beijing, China. The top-left corner of the figure displays the LST visualization using the difference of mean (timeline 2): min -3°C to max +3°C, while the top-right corner presents the linear trend LST (timeline 1): min -0.2°C to max +0.2°C. The bottom-left corner shows the "After" MODIS satellite NDVI image mosaicked for the year 2015, and the bottom-right corner displays a disturbed mask indicating areas where crops were converted to built-up areas. The images was generated using GEE and ESRI ArcMap software (version 10.8).

Beijing was selected as a study area due to its high rate of urbanization and extensive LCC in recent decades. From the LST visualizations, it is evident that higher LST values are more prominent in built-up areas, and the road networks are distinctly visible in the difference of mean LST (timeline 1) and linear trend LST (timeline 1). The bottom-right mask further emphasizes this observation, showing that the conversion of crops to built-up areas is widespread and dominant in the region. These visual patterns confirm that the increase in built-up areas is directly associated with a corresponding increase in LST, since urbanized surfaces absorb and retain more heat compared to croplands.

It can be observed in Figure 4.22 that the alignment between the LST images-difference of mean (timeline 2), linear trend (timeline 1) and the crop-to-built-up mask is notable, as features such as road networks and disturbed pixels in the mask correspond clearly to areas of significant warming in the difference of mean LST (timeline 2) image. While these features are more pronounced in the difference of mean LST (timeline 2), the linear trend LST (timeline 1) also captures these patterns but with less detail. For example, road networks are still visible in the linear trend LST (timeline 1), though the warming effect is more gradual and less localized compared to the difference of mean LST (timeline 2).

This focused view of Beijing demonstrates the clear relationship between urbanization and the corresponding increase in LST. The conversion of croplands to built-up areas increases surface temperatures due to reduced vegetation, increased heat absorption by urban materials, and the urban heat island effect. The presence of distinct road networks in both the difference of the mean LST (timeline 2) and the linear trend LST (timeline 1) images further underscores the impact of urbanization on LST.

In conclusion, the observations from Area 5 highlight the significant impact of conversion of croplands to built-up areas and urbanization on LST. This analysis emphasizes the importance of sustainable urban planning and mitigation strategies to minimize the impact of LST from urbanization on the environment.

Based on Figure 4.23, the final area in northern Canada exhibits two opposing warming patterns visualized as "red hues" on the LST maps. In the difference of mean LST (timeline 2) image, the increase in LST appears to be more dominant with a brighter and more widespread red hue, whereas in the linear trend LST (timeline 1), the warming effect is less pronounced and more spatially constrained. By comparing these two visualizations, it becomes apparent that the linear trend LST (timeline 1) captures more distinct patterns of warming and cooling, while the difference of mean LST (timeline 2) produces a less detailed and generalized depiction of temperature changes.

The difference in detail between the two visualizations can be attributed to the timelines used in their creation. The linear trend LST which is derived from timeline 1, is based on 20 years of data, providing a more comprehensive and nuanced representation of long-term temperature trends.

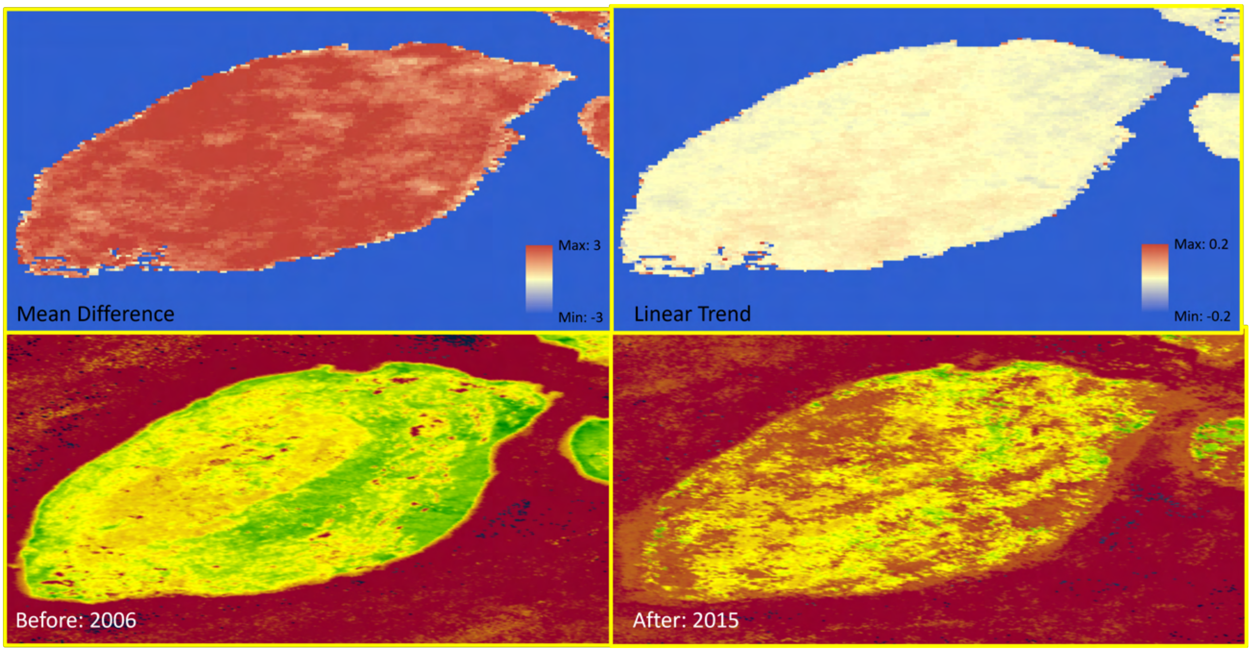

Figure 4.23: Sample area 6: Northern Canada used for visualization of the LCC and LST relationship. The figure provides a focused view of Area 6 located in northern Canada. The top-left corner of the figure displays the LST visualization using the difference of mean LST (timeline 2): min -3°C to max +3°C, while the top-right corner presents the linear trend LST (timeline 1): min -0.2°C to max +0.2°C. The bottom-left corner shows the "Before" MODIS satellite NDVI image mosaicked for the year 2006, and the bottom-right corner displays the "After" MODIS satellite NDVI image mosaicked for the year 2015. The images was generated using GEE and ESRI ArcMap software (version 10.8).

In contrast, the difference of mean LST from timeline 2 is calculated using two 5-year periods (end period and start period) which is more susceptible to anomalies or incomplete data.

Further examination of the "Before" and "After" NDVI images reveals additional insights. The "Before" image from 2006 contains fewer cloudy pixels and appears clearer, while the "After" image from 2015 is more pixelated and cloud-affected. This disparity suggests that the difference in the mean LST (timeline 2) image may have been influenced by data limitations or the presence of clouds resulting in a less detailed and potentially less accurate depiction of temperature changes in the region.

Despite these limitations, the warming patterns captured in Area 6 align with expectations for northern Canada a region experiencing significant environmental changes. The observed LST increases are likely tied to reduced snow and ice cover, exposing more land surface and contributing to increased heat absorption. The differences in clarity and detail between the difference of mean LST (timeline 2) and linear trend LST (timeline 1) image underscore the importance of using long-term datasets, such as those utilized in the linear trend, for more reliable assessments of temperature trends.

In conclusion, Area 6 highlights the value of comparing the difference of the mean LST (timeline 2) and linear trend LST (timeline 1) images to gain a better understanding of temperature dynamics. While the difference of mean LST (timeline 2) offers a overview of the overall LST increase or decrease, the linear trend LST (timeline 1) provides a more accurate and detailed perspective, particularly in regions like northern Canada, where climatic changes are significant. These findings emphasize the importance of the use of different LST datasets to analyze its relationship with LC.

5 Discussion

5.1 Large-scale LC changes since 2000

The analysis of global LCC since 2000 reveals striking patterns of transformation across diverse ecosystems shedding light on the dynamic interplay between natural processes and human activities. Among the most prominent changes, the transition from bare areas (class 200) to sparse vegetation (class 150) stands out as the most significant. The transition from bare areas to sparse vegetation suggests potential recovery in previously degraded or arid regions, likely driven by improved environmental conditions, climatic changes, or targeted restoration efforts. Similarly, the conversion of sparse vegetation (class 150) to grassland (class 130), which is the second of the most prominent LCC, underscores ecological transitions within the aggregated type "Grass and Shrubs". In particular, the aggregated classification type "Grass & Shrubs" accounts for a significant proportion of the global land area, further highlighting its vulnerability to large-scale disturbances as discussed in Section 4.2.1: ESA CCI LC global statistics.

Urban expansion emerges as a particularly impactful driver of LC change, as evident in the transition from rainfed cropland (class 10) to urban areas (class 190), which ranks as the third-largest global transition. This pattern reflects the rapid growth of urban centers and infrastructure development, a trend that was also emphasized in Figure 4.5 under Section 4.2.2: ESA CCI LC transition matrix. The widespread conversion of various LC types into urban areas underscores the intensification of human activities and raises concerns about the sustainability of these transformations and their long-term environmental consequences.

Forested and shrubland ecosystems have also undergone significant changes, such as the conversion of evergreen needleleaf tree cover (class 70) to mosaic tree and shrub cover (class 100) and the transition from deciduous broadleaf tree cover (class 60) to shrubland (class 120). These LC transitions highlight the ongoing displacement and reorganization within forested areas, potentially driven by deforestation, LULC tensions, and climate-related factors. The aggregated "Grass & Shrubs" classification (encompassing classes 120, 130, and 150) experienced the highest levels of disturbance and transformation globally, indicating its susceptibility to external pressures and environmental changes.

As discussed in Section 4.2.2, the majority of global LC disturbances are concentrated in the aggregated classification types "Forest" and "Grass & Shrubs", reflecting their extensive global AOI coverage. In contrast, categories such as "Flooded Vegetation", "Bare & Built-up", and "Water & Snow" exhibit the smallest global areas and consequently lower levels of transformation.

The continued expansion of built-up areas (class 190) reinforces the growing impact of urbanization on global LC patterns. The dominance of urban transitions highlights the widespread influence of human land use and signals long-term challenges for biodiversity, ecosystem services, and sustainable development. Balancing the demands of urbanization with the need for conservation and sustainable land management will be crucial to safeguarding the ecological integrity of the planet.

In summary, this analysis captures the dynamics of large-scale LC changes, revealing key areas of vulnerability, and highlighting the significant influence of deforestation and urbanization. These insights provide a valuable foundation for the development of targeted strategies in land management, conservation, and climate adaptation to mitigate future environmental impacts.

5.2 Quantifying mean annual LST variations due to LC changes

The quantifying the mean annual LST variations due to LCC provides valuable insights on the complex interactions between the LC transitions and the LST dynamics. The findings reveal a variety of temperature impacts, with cooling effects predominantly linked to transitions that increase vegetation density and moisture retention, while warming effects are associated with deforestation and urbanization.

Quantifying mean annual LST variations due to LCC was visualized using localized area samples in Section 4.4: Local samples of the LCC and LST relationship. This quantification used the disturbed and undisturbed masks to select LST pixels globally. Each LC transition mask, represented by global binary pixels, was overlayed onto the linear trend LST (timeline 1: whole period) and the difference of mean LST (timeline 2: LST difference). The LC classification included 22 classes, resulting in 484 LCC transitions, which were displayed in a transition matrix bubble plot (Figure 4.8 and Figure 4.9) in Section 4.3.2: Disturbed areas of LST per LCC. The extracted LST values for undisturbed and disturbed areas were discussed in Sections 4.3.1: Undisturbed areas LST and Section 4.3.2: Disturbed areas of LST per LCC, with the top 10 LCC transitions further analyzed in Figure 4.13 under Section 4.3.6: Top 10 quantified transitions of the LC-LST relationship.

Among the samples from the top LCC transitions, a notable cooling effect was observed in the transition from bare areas (class 200) to grasslands (class 130), resulting in a significant temperature decrease of $-0.45°C$, with a cooling rate of $-0.030°C/\text{year}$. This transition exhibited the largest cooling effect among the top 10 LCC transitions, highlighting the critical role of vegetation in mitigating surface heating through enhanced evapotranspiration and moisture retention.

Similarly, transitions from sparse vegetation (class 150) to grassland (class 130) and from bare areas (class 200) to sparse vegetation (class 150) resulted in cooling effects of $-0.16°C$ (cooling rate: $-0.011°C/year$) and $-0.20°C$ (cooling rate: $-0.017°C/year$), respectively. These findings further underscore the importance of increased vegetation cover in the regulating of LST.

Conversely, warming effects were most prominent in transitions involving urbanization and deforestation. The conversion from rainfed cropland (class 10) to urban areas (class 190) resulted in an increase in temperature of $+0.39°C$, with a warming rate of $+0.019°C/year$. This warming aligns with expectations, as urban areas have lower albedo and higher heat retention properties, which intensify surface heating. Deforestation-related transitions, such as from deciduous broadleaf tree cover (class 60) to shrubland (class 120), contributed significantly to temperature increases, with a warming effect of $+0.43°C$. Transitions involving the reduction of water bodies also led to notable warming, as exemplified by the shift from flooded shrub/herbaceous cover (class 180) to needleleaf evergreen forests (class 70), which produced the most substantial temperature increase ($+0.84°C$, warming rate: $+0.076°C/year$). This result underscores the role of water in regulating surface temperatures through evaporation, with its removal contributing to elevated LST values.

Overall, the results highlight the critical influence of vegetation density, moisture retention, and land surface properties on LST dynamics. LCC transitions that increase vegetation cover tend to exert a cooling effect, mitigating the impacts of rising temperatures, while urbanization, deforestation, and the loss of water bodies contribute to the warming of LST. These findings underscore the importance of preserving and restoring vegetation cover to mitigate the effects of LCC on the increase of global LST.

In conclusion, while the majority of the findings align with established patterns, the unexpected results observed in specific transitions such as the transition from class 70: needleleaf evergreen forests to class 120: shrublands reveal the complexities of LCC and their impacts on LST. These anomalies underscore the need for further research to explore localized influences, neighboring interactions, and other factors that contribute to these dynamics. Understanding these mechanisms will improve our ability to predict and manage the impacts of LCC on global and regional LST effectively.

5.3 Significant regions cooling and warming due to LC changes

The analysis of significant regional cooling and warming due to LCC as visualized in Figure 4.14 and Figure 4.15 under Section 4.3.7: Disturbed areas LST of overall LCC, provides valuable insights into the spatial and latitudinal variability of the LST dynamics. Both figures effectively highlight the different overall regional LSTs over 20 years along with the LST trends, emphasizing the global variability of warming and cooling patterns over the study period.

In both timelines, cooling trends are prominently concentrated in the northern hemisphere, particularly in regions between 40° and 90°N. This cooling is most evident in areas such as Canada, Greenland, Kazakhstan, and northeastern China, as well as portions of India. These trends are closely associated with transitions involving increased vegetation density, which enhance evapotranspiration and mitigate surface heating. In contrast, the southern hemisphere shows less pronounced cooling trends, reflecting a lower overall vegetation density and differing LULC dynamics.

Warming patterns, on the other hand, are particularly notable in the southern hemisphere (0° to -20°S) and in polar regions of the northern hemisphere (60° to 90°N). The tundra regions of northern Russia and Alaska stand out as significant warming hotspots, likely driven by ongoing climate change and vegetation shifts in these sensitive ecosystems. Slight warming trends are also observed in Europe, parts of Asia, northwestern Australia, and Brazil, aligning with urbanization and LuLC changes.

The global LST maps and scatter plots in Figure 4.14 and Figure 4.15 demonstrate consistent spatial patterns between the warming and cooling distributions. Both scatter plots accurately represent the latitudinal variability of temperature changes, with cooling more dominant in higher latitudes of the northern hemisphere and warming more prevalent in southern latitudes and northern polar regions. This alignment between the scatter plots and the global maps reinforces the robustness of the analysis. Importantly, the uniform distribution of LST observed in regions such as northern Africa highlights areas with minimal notable warming or cooling trends, providing a baseline for comparison with more dynamic regions. These stable zones may offer opportunities to investigate the relative resilience of certain ecosystems to LCC and climate change.

Overall, the visualizations in Figure 4.14 and Figure 4.15 effectively capture the global and regional variability of the changes in LST over the entire study period. The figures reveal clear spatial and latitudinal patterns of warming and cooling, providing critical insights into the regional impacts of LCC on LST dynamics. These findings underscore the importance of targeted regional studies in addressing localized drivers of warming and cooling and in the formation of global and regional climate adaptation strategies.

5.4 Impact of common LC changes on LST

The analysis of common or "aggregated" LC transitions and their associated impacts on land LST, as illustrated in Figure 4.8 and Figure 4.9 under Section 4.3.3: LST per transition summary: LST whole period and the LST difference reveal notable patterns of warming and cooling across various classes. The size of each bubble in the transition matrix plots corresponds to the area size, while the color intensity represents the temperature change, providing a comprehensive visualization of LCC impacts on LST dynamics.

Key observations

Agriculture transitions

1. Transitions from agricultural areas to grass and shrubs generally resulted in LST cooling, except for the case of class 150: sparse vegetation, which exhibited an increase in LST.
2. Conversions from agricultural areas to urban or bare areas showed significant warming, with transitions to bare areas resulting in a stronger warming effect.
3. Transitions from agricultural classes to water bodies consistently led to LST cooling, aligning with the thermal properties of water.

Forest transitions

1. Most transitions originating from forests to other aggregated classification types resulted in LST warming.
2. However, class 70: tree cover - evergreen needleleaf displayed an unexpected consistent cooling effect when transitioning to other classes, including shrubland, grassland, sparse vegetation, and bare areas, which warrants further exploration in the subsequent sections.

Grass and shrubs transitions

1. The majority of transitions within and from the aggregated grass and shrubs category resulted in cooling. However, transitions to class 80: tree cover - deciduous needleleaf consistently showed LST warming, indicating distinct temperature dynamics within this class.
2. Transitions from class 120: shrubland to agricultural classes predominantly caused warming, except in specific cases (e.g., transitions to class 110: mosaic herbaceous cover, class 130: grassland, and class 150: sparse vegetation), which exhibited cooling effects.

Bare and built-up classes

1. Transitions toward urban areas (class 190) consistently led to warming, highlighting the role of urbanization in amplifying surface temperatures.
2. Transitions from bare areas (class 200) resulted in cooling across all aggregated classification types, reflecting the lower thermal absorption of bare surfaces. However, transitions towards bare areas exhibited mixed outcomes, particularly with forested and grass and shrubs classes, indicating complex interactions.

Water bodies transitions

1. Transitions originating from various classes to water bodies (class 210) predominantly resulted in LST cooling, except for class 80: tree cover - deciduous needleleaf, which exhibited LST warming.
2. Conversely, transitions from water bodies to other classes generally showed warming, except for transitions involving class 70: tree cover - evergreen needleleaf, which demonstrated LST cooling.

The results reveal that, while many transitions align with expected thermal behaviors, several unexpected patterns highlight the complexity of the relationship between LC changes and LST. For instance, the consistent cooling effects observed in transitions involving class 70: tree cover - evergreen needleleaf and the consistent warming effects in transitions involving class 80: tree Cover - deciduous needleleaf underscore the influence of specific LC properties. Similarly, the conversion from the agricultural type category to the forest type emphasizes the need for further investigation to understand the driving mechanisms behind these interactions.

Overall, this analysis underscores the critical role of LC transitions in shaping LST dynamics and highlights the importance of preserving and managing LC to mitigate temperature increases. These findings also provide a basic foundation for targeted research on observed complexities and anomalies, which will be examined further in the next section.

5.5 Challenges and anomalies in the analysis

The analysis of LC transitions and their associated LST changes revealed several anomalies and inconsistencies. These unexpected results highlight the challenges and uncertainties inherent in working with complex datasets and environmental processes. In the following, the inconsistencies are described, followed by a discussion of probable causes.

5.5.1 Inconsistency 1: Cooling in class 70 - tree cover (evergreen needleleaf)

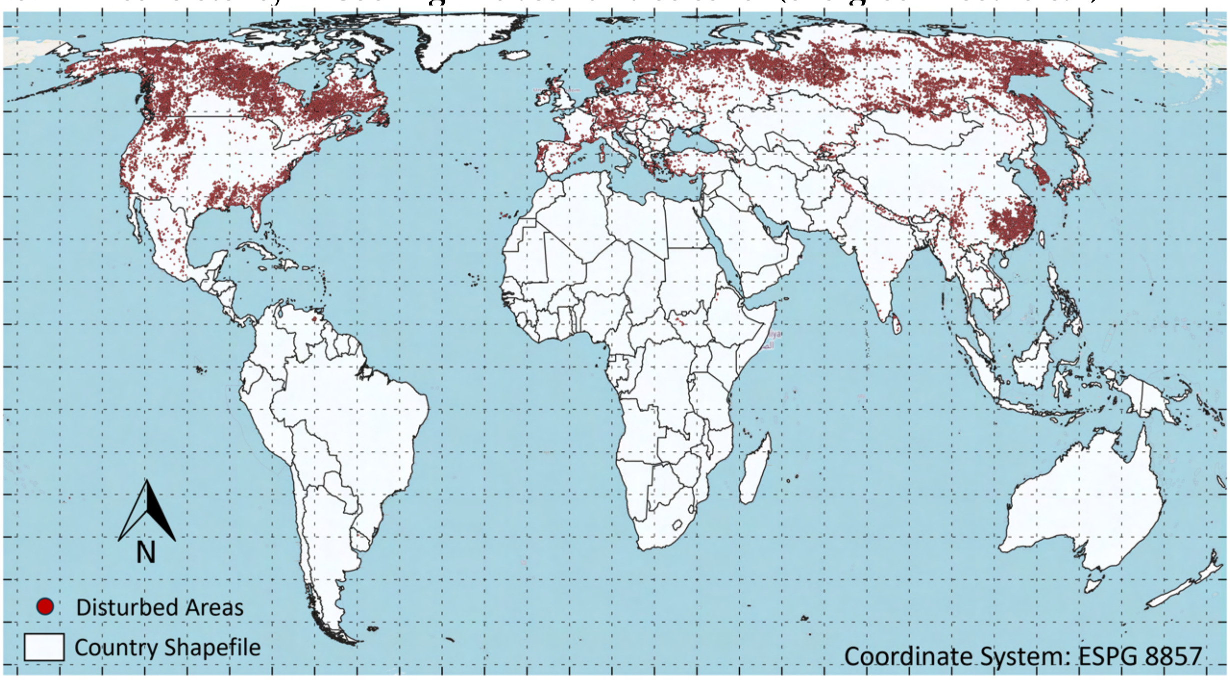

Figure 5.1: Tree cover - evergreen needleleaf (class 70): before and after distribution of disturbed points. The map shows 50,000 random pixels from the before and after mask of class 70, converted to point shapefiles and overlaid on a basemap layer with country shapefiles to visualize the distribution of disturbances. The map and the basemap were generated using QGIS desktop software (version 3.32.3).

Based on Figure 5.1, most LST transitions involving class 70: tree cover (evergreen needleleaf) in both its "before" and "after" states resulted in cooling, contrary to typical expectations of warming associated with deforestation. Further analysis indicates that the majority of these transitions occurred in Canada, where cooling trends are often influenced by regional factors such as high-latitude climatic conditions.

5.5.2 Inconsistency 2: Warming in class 80 - tree cover (deciduous needleleaf)

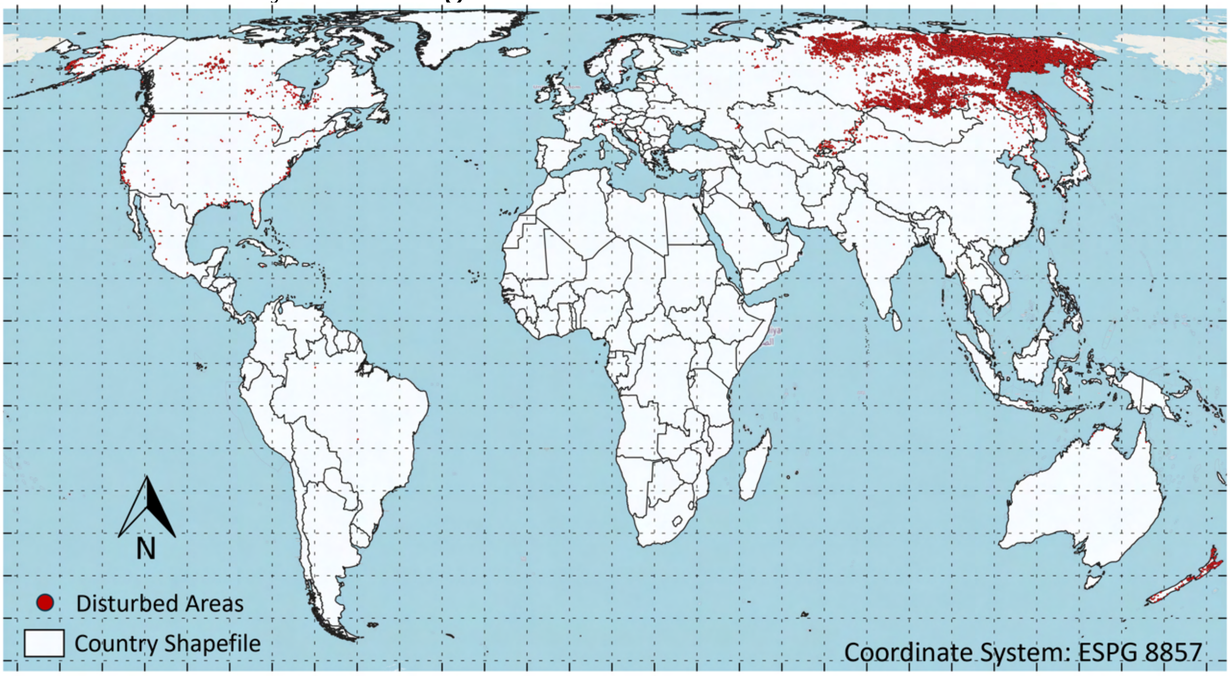

Figure 5.2: Tree cover - deciduous needleleaf (class 80): before and after distribution of disturbed points. The map shows 50,000 random pixels from the before and after mask of Class 80, converted to point shapefiles and overlaid on a basemap layer with country shapefiles to visualize the distribution of disturbances. The map and the basemap were generated using QGIS desktop software (version 3.32.3).

Conversely as seen in Figure 5.2, transitions involving class 80: tree cover (deciduous needleleaf) consistently resulted in warming, regardless of whether this class appeared in the "before" or "after" state. Spatial analysis shows that these transitions are predominantly located in tundra regions, where significant warming has been observed due to snow and ice cover loss, combined with reduced forest density. These combined effects are likely to amplify the impact of warming in these areas.

5.5.3 Inconsistency 3: Increased temperatures in agricultural transitions to forests

The classification under the aggregated agriculture types are defined as: class 10: cropland, rainfed, class 20: cropland, irrigated or post-flooding, class 30: mosaic cropland (>50%) / natural vegetation (tree, shrub, herbaceous cover) (<50%), class 40: mosaic natural vegetation (tree, shrub, herbaceous cover) (>50%) / cropland (<50%) (Copernicus Climate Change Service, 2019.

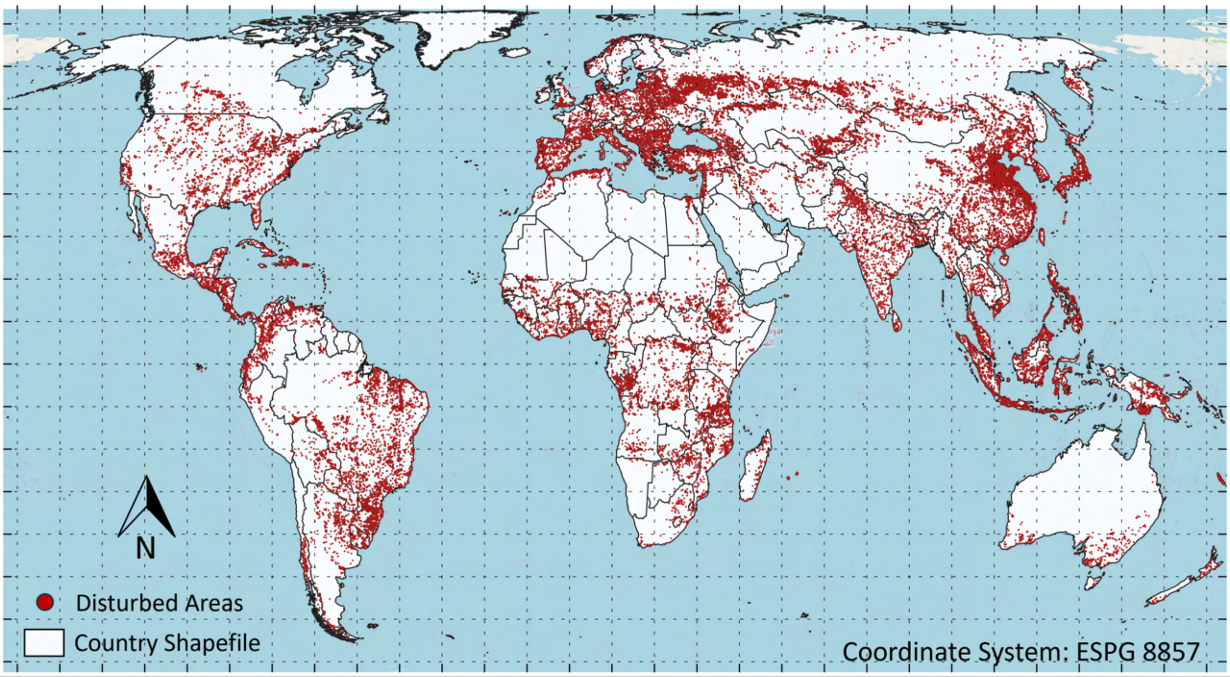

Figure 5.3: Aggregated class type "Agriculture": Before and after distribution of disturbed points. The map shows 50,000 random pixels from the before and after mask of the aggregated agriculture type, converted to point shapefiles and overlaid on a basemap layer with country shapefiles to visualize the distribution of disturbances. The map and the basemap were generated using QGIS desktop software (version 3.32.3).

Based on Figure 5.3, the transitions from agricultural land to forested areas were unexpectedly associated with the increase in LST, contradicting the expectation of cooling due to the increased in vegetation density. Upon reviewing the distribution of agricultural classes, it was observed that these points are evenly distributed throughout the globe. This uniform distribution suggests that changes in surrounding LC types may have influenced the LST outcomes, with nearby areas potentially contributing to warming effects. On the other hand, the results in Section 4.3.4: Linear trend LST comparison of day and night show the expected quantified LST from the transition from agricultural lands to forested area, highlighting the importance of using the correct LST combination to quantify the temperature.

5.6 Limitations and probable causes of observed anomalies

There are different uncertainties that can influence the results of the quantified LST. One of the probable causes would be the accuracy of the LC images. The ESA CCI LC maps have an overall accuracy of 75.6% for the 1998–2015 period, which decreases to 70.77% (std = 0.28) for the 2016–2022 period (Copernicus Climate Change Service, 2019. These inaccuracies could result in the misrepresentation of specific LCC transitions and their associated temperature impacts. Furthermore, there is no clear definition of the LC classes samples, one sample would be from ESA CCI LC - class 10: rainfed cropland and class 20: irrigated cropland, there is no absolute definition of "cropland" as expected.

Another challenge arises from the resolution mismatch between the LC and LST datasets, which further complicates the analysis. The ESA CCI LC dataset has a spatial resolution of 300 meters(Copernicus Climate Change Service, 2019, while the MODIS LST dataset has a coarser resolution of 1,000 meters(Hulley and Hook, 2017). The disparity in resolution allows neighboring areas to influence the measured LST values, potentially skewing the results. Addressing this mismatch in future studies could involve clustering pixel groups, analyzing the impact of surrounding pixels, or using datasets with matching spatial resolutions to improve data alignment.

The selection of timelines and LC disturbances also plays a critical role in shaping the outcomes of the analysis. Different timelines, such as the disturbance between 2000 and 2020 compared to that between 2006 and 2015, yielded varied results. These variations influence LC transitions and subsequently affect the quantified LST changes. The variability underscores the importance of carefully selecting the timelines to align with the objectives of the study and ensure consistency in the analysis.

Another probably cause of the uncertainties would be the accuracy of the LST images. According to a study done by Xu et al. (2023), MOD products had the lowest RMSE among all skin temperature with an RMSE of 3.35 K, however these products also exhibited a relatively high percentage of missing values (48.4%) in certain regions such as the Heihe River Basin (Xu et al., 2023).These missing data points can introduce biases, particularly in regions with frequent cloud cover or other factors that obscure satellite observations. The "clear sky" bias was examined in a study by Gallo and Krishnan (2022), they evaluated the bias induced by the use of clear-sky versus all-sky (clear and cloudy) conditions which revealed that there are significant differences between the mean annual clear-sky and all-sky daytime LST (Gallo and Krishnan, 2022). Moreover, studies have shown that different combinations of MODIS aqua, terra, day and night products yield different accuracy and results (Zhang et al., 2016). Although this study used the equation from Xing et al. (2021), which demonstrated an RMSE of 0.80 K, further research is needed to refine LST data accuracy and minimize biases in future analyses(Xing et al., 2021.

Lastly, uncertainties can be introduced when dealing with LST difference calculations. The shorter timelines, such as the end period and the start period (5 years) and calculating the difference between them, are more prone to biases due to the limited data range and missing pixels. These missing values which are often caused by cloud cover as visualized in Figure 4.23 under Section 4.4: Local samples of LCC and LST relationship, can create gaps in LST measurements that affect the reliability of results. In contrast, the linear trend LST approach which integrates 20 years of data provides a smoother and more consistent representation of pixel distributions. However, these methodological differences highlight the need for careful consideration when interpreting results derived from different approaches.

In summary, this study's challenges and uncertainties stem from data accuracy, resolution mismatches, timeline selection, and methodological limitations. Key observations, such as cooling effects in class 70: evergreen needleleaf transitions, warming in tundra regions involving class 80: deciduous needleleaf, and unexpected warming in agricultural transitions to forests, highlight the complexity of LC and LST interactions. Addressing these issues through improved datasets, resolution compatibility, and robust methodologies in future studies will enhance the reliability of LST quantification and provide deeper insights into the dynamics of LCC and temperature variability.

5.7 Suggestions for future research

The study initially began by using the MODIS LC product as discussed in Section 2.3: Other datasets considered. However, due to its relatively lower accuracy and the complexities of its LC classes, and the MODIS LC dataset which categorizes LC into five classification types (Sulla-Menashe et al., 2019) presented challenges. Furthermore, when MODIS LC was tested specifically for Type 1 and Type 3 LC, the aggregation of classes yielded inconsistent results, leading to significant variability in the results. Consequently, the ESA CCI LC dataset was selected as a substitute, as it was deemed more suitable for the study due to its higher accuracy and detailed LC classifications. With the LC dataset finalized, the MODIS LST data, already prepared for use in the study, served as the primary temperature dataset.

Upon further review, it was noted that ESA CCI also offers an LST product with uncertainty estimates similar to the MODIS aqua LST providing monthly average LST data (Ghent et al., 2022). However, the ESA CCI LST product only covers the period from 4th July 2002 to 31st December 2018 (Ghent et al., 2022), which does not align with the timeline required for this study. This limitation reinforces the importance of aligning temporal coverage and data resolution between LC and LST datasets. For future studies, improving the resolution compatibility between the LC and LST data would enhance the reliability of LST quantification. Additionally, addressing the spatial resolution mismatch—ESA CCI LC has a 300-meter resolution (ESA—European Space Agency, 2014; Defourny, 2019), while MODIS LST has a coarser 1,000-meter resolution (Hulley and Hook, 2017), which could help mitigate the influence of neighboring pixels and improve the accuracy of LST values associated with specific LC transitions.

There is no clear representation of surface temperatures, there is a notable difference between LST and near-surface air temperature, which should be considered in future analysis. Multiple studies have focused on improving the accuracy of LST measurements by combining LST with other datasets such as air temperature. For instance, Qin et al. (2022) conducted a study on the Tibetan Plateau that fused MODIS and ERA5 temperature datasets that resulted in improved accuracy, with an overall RMSE of 1.33 °C and a mean bias error (MBE) of 1.03 °C (Qin et al., 2022). Similarly, further exploration of the combination of LST products with other temperature datasets could provide a more robust representation of temperature dynamics, especially in regions where ground-based validation is limited. Furthermore, studies could explore the integration of advanced data fusion techniques, such as machine learning, to combine multiple satellite datasets, enabling improved spatial and temporal resolution for enhanced LST quantification. Lastly, since this study relies entirely on global satellite imagery datasets, there is a lack of ground-truth validation, which could otherwise enhance the accuracy and reliability of the LST measurements. Although satellite images such as MODIS provide consistent large-scale coverage images, they may be subject to uncertainties due to atmospheric influences, sensor limitations, and spatial resolution constraints (Xing et al., 2021; Duan et al., 2021; Duan et al., 2014. The absence of direct in-situ validation limits the ability to assess potential biases or systematic errors in the derived LST values. For future research, the accuracy of LST can be significantly improved by integrating global ground truth datasets to validate LST data derived from satellite images.

Incorporating surrounding pixels into the analysis could also provide a more in-depth understanding of how LST varies spatially around LC changes. By examining not only the pixels directly undergoing transitions but also their neighboring pixels, researchers can capture the influence of neighborhood effects and gradual transitions between LC types. This approach would allow for a more comprehensive analysis of the localized thermal impacts of LCC and provide insights into how surrounding factors contributing to regional temperature patterns. Additionally, adopting a regionalized approach to quantifying LST changes could improve our understanding of the relationship between LC changes and LST dynamics at a localized level. Regional analysis could involve dividing the study area into smaller zones based on geographic, climatic, or ecological characteristics, allowing for a more granular examination of the relationship of LCC and LST trends. Compiling and comparing these regional results could highlight variations in how LC changes affect LST across different environments. For example, forest loss in tropical regions may have different thermal implications compared to similar changes in boreal or temperate regions. A regionalized approach could also help identify areas where specific mitigation efforts, such as reforestation or urban greening would be most effective in reducing local warming. Moreover, regionalized data could guide targeted adaptation strategies to address local vulnerabilities to climate change such as improving vegetation in urban areas to counteract heat island effects.

In summary, while the current study provides valuable insights into the relationship between LC changes and LST, there are opportunities to improve future research. Addressing data alignment issues, improving spatial and temporal resolutions, and integrating datasets such as air temperature and ground-truth validation could provide a more accurate and comprehensive understanding of LST dynamics. Additionally, incorporating neighborhood pixel analysis and regionalized approaches would allow for a more detailed exploration of localized temperature changes, helping to inform targeted climate adaptation and mitigation strategies. By refining methodologies and utilizing more accurate and harmonized datasets, future studies could further reduce uncertainties and improve the understanding of the complex interactions between LC and LST.

6 Conclusion

This research provides a comprehensive analysis of global LCC since 2000 and their impacts on LST. Significant transformations were observed across diverse ecosystems that are driven both by natural processes and human activities. Among the most prominent changes are the transition from bare areas (class 200) to sparse vegetation (class 150) which emerged as the largest global change, indicating ecological recovery in previously degraded or arid regions. Similarly, the conversion of sparse vegetation (class 150) to grasslands (class 130) underscored ecological transitions within the aggregated "Grass Shrubs" classification, which experienced the highest levels of global disturbance due to its extensive coverage and susceptibility to environmental pressures. Urban expansion, such as the transition from rainfed cropland (class 10) to urban areas (class 190) ranked as the third-largest LCC globally, reflecting the rapid growth of cities and infrastructure development. Significant changes were also observed in forested and shrubland ecosystems, with transitions such as evergreen needleleaf forests (class 70) converting to mosaic tree and shrub cover (class 100) and deciduous broadleaf forests (class 60) transitioning to shrubland (class 120). These patterns highlight the vulnerability of natural ecosystems to human-driven changes and the global prevalence of deforestation, urbanization, and LULC changes.

The mean annual LST variations due to LCC were quantified using a systematic approach involving disturbed and undisturbed masks, global binary pixel overlays, and LST trend calculations. Two key timelines were used: the linear trend over the whole period (timeline 1) and the difference of the mean between the start and end periods (timeline 2). By integrating LST data with a transition matrix of 22 LC classes equivalent to 484 transitions, the analysis provided a detailed understanding of the LST dynamics across global LCC. For instance, the transition from bare areas (class 200) to grasslands (class 130) produced the largest cooling effect, with a temperature decrease of $-0.45°C$ at a rate of $-0.030°C/year$. Similarly, the transition from bare areas (class 200) to sparse vegetation (class 150) resulted in a cooling effect of $-0.20°C$ at a rate of $-0.017°C/year$. These findings highlight the critical role of increasing vegetation density in mitigating surface heating and regulating LST. On the other hand, transitions that involve water loss produced the most significant warming effects observed in this study, underscoring the critical role of water and vegetation in moderating surface temperatures. For example, the transition from flooded shrub/herbaceous cover (class 180) to needleleaf evergreen forests (class 70) resulted in a temperature increase of $+0.84°C$ at a rate of $+0.076°C/year$. Similarly, deforestation, such as the transition from deciduous broadleaf forests (class 60) to shrubland (class 120), contributed significantly to warming with a temperature increase of +0.43°C at a rate of +0.032°C/year. Similarly, urban expansion has further amplified the warming effects, as seen in the conversion of cropland (class 10) to urban areas (class 190), which resulted in a temperature increase of +0.39°C at a rate of +0.019°C/year. Collectively, these findings emphasize the significant impact of LULC changes, particularly water loss, deforestation, and urbanization, in amplifying surface temperatures and highlight the critical need for sustainable land management to mitigate these effects.

Regional analysis revealed distinct patterns of warming and cooling associated with LCC. Cooling effects were prominent in northern regions, such as Canada, Greenland, and northeastern China, where vegetation recovery played a key role. In contrast, warming was more evident in tundra regions, including northern Russia and Alaska, where forest loss and snow cover reduction amplified surface heating. The tropical and temperate regions also displayed warming trends associated with urban expansion and deforestation. These findings demonstrate the importance of the geographic context in shaping the thermal impacts of LCC.

The most common LCC transitions revealed a clear relationship between vegetation density and LST impacts. Transitions that increased vegetation cover, such as bare areas to grasslands, consistently resulted in cooling effects due to enhanced evapotranspiration and moisture retention. Conversely, transitions involving deforestation, such as forests to shrublands or forests to bare areas, led to significant warming effects by reducing vegetation density and altering surface albedo. Urban expansion was another dominant driver of warming, with transitions from agricultural land to urban areas highlighting the heat-retention properties of built-up environments. Furthermore, transitions involving the loss of water bodies, such as flooded shrub/herbaceous cover to needleleaf forests, produced the most substantial warming effects, underscoring the critical role of water in regulating surface temperatures. These findings highlight the importance of preserving and restoring vegetation and water bodies to mitigate the adverse impacts of LCC on LST.

This study provides valuable insights in the interplay between global LCC and LST dynamics. Although many findings align with established patterns, anomalies such as cooling in evergreen needleleaf forest transitions and warming in tundra regions highlight the complexities of LCC and their localized impacts. Future research should focus on resolving uncertainties by improving data alignment, addressing resolution mismatches, and integrating ground-truth validation and advanced methodologies such as pixel clustering and data fusion. Regionalized analysis could further enhance our understanding of localized LCC impacts and guide targeted climate adaptation and mitigation strategies, such as reforestation and urban greening. By refining the methodologies and using harmonized datasets, future research can provide deeper insights into the complex interplay between LC and LST dynamics. These efforts will support sustainable land management practices and contribute to global climate adaptation and mitigation strategies.

Bibliography

Abdullah-Al-Faisal, Abdulla - Al Kafy, A. N. M. Foyezur Rahman, A. A. Rakib, K. S. Akter, V. Raikwar, D. M. A. Jahir, J. Ferdousi, and M. A. Kona (Aug. 2021). "Assessment and prediction of seasonal land surface temperature change using multi-temporal Landsat images and their impacts on agricultural yields in Rajshahi, Bangladesh." *Environmental Challenges* 4, p. 100147.

Abou Samra, R. M. (Nov. 2023). ""Investigating and mapping day-night urban heat island and its driving factors using Sentinel/MODIS data and Google Earth Engine. Case study: Greater Cairo, Egypt"." *Urban Climate* 52, p. 101729.

Ahmed, M. R., E. Ghaderpour, A. Gupta, A. Dewan, and Q. K. Hassan (Apr. 2023). "Opportunities and Challenges of Spaceborne Sensors in Delineating Land Surface Temperature Trends: A Review." *IEEE Sensors Journal* 23.7, pp. 6460–6472.

Amani, M., A. Ghorbanian, S. A. Ahmadi, M. Kakooei, A. Moghimi, S. M. Mirmazloumi, S. H. A. Moghaddam, S. Mahdavi, M. Ghahremanloo, S. Parsian, Q. Wu, and B. Brisco (2020). "Google Earth Engine Cloud Computing Platform for Remote Sensing Big Data Applications: A Comprehensive Review." *IEEE Journal of Selected Topics in Applied Earth Observations and Remote Sensing* 13, pp. 5326–5350.

Arvidson, T., S. Goward, J. Gasch, and D. Williams (Oct. 2006). "Landsat-7 Long-Term Acquisition Plan." *Photogrammetric Engineering & Remote Sensing* 72.10, pp. 1137–1146.

Avdan, U. and G. Jovanovska (2016). "Algorithm for Automated Mapping of Land Surface Temperature Using LANDSAT 8 Satellite Data." *Journal of Sensors* 2016, pp. 1–8.

Bala, R., R. Prasad, and V. Pratap Yadav (July 2020). "A comparative analysis of day and night land surface temperature in two semi-arid cities using satellite images sampled in different seasons." *Advances in Space Research* 66.2, pp. 412–425.

Bardan, R. (Jan. 2024). *NASA Analysis Confirms 2023 as Warmest Year on Record*. Tech. rep. National Aeronautics and Space Administration (NASA).

Barnes, W., T. Pagano, and V. Salomonson (July 1998). "Prelaunch characteristics of the Moderate Resolution Imaging Spectroradiometer (MODIS) on EOS-AM1." *IEEE Transactions on Geoscience and Remote Sensing* 36.4, pp. 1088–1100.

Barnes, W., X. Xiong, and V. Salomonson (Dec. 2003). "Status of terra MODIS and aqua modis." *Advances in Space Research* 32.11, pp. 2099–2106.

Bastiaanssen, W., M. Menenti, R. Feddes, and A. Holtslag (Dec. 1998). "A remote sensing surface energy balance algorithm for land (SEBAL). 1. Formulation." *Journal of Hydrology* 212-213, pp. 198–212.

Bateman, J. (Jan. 2024). *2023 was the world's warmest year on record, by far*.

Bechtel, B. (Mar. 2015). "A New Global Climatology of Annual Land Surface Temperature." *Remote Sensing* 7.3, pp. 2850–2870.

BECKER, F. and Z.-L. LI (Mar. 1990). "Towards a local split window method over land surfaces." *International Journal of Remote Sensing* 11.3, pp. 369–393.

Betts, R. A., P. D. Falloon, K. K. Goldewijk, and N. Ramankutty (Feb. 2007). "Biogeophysical effects of land use on climate: Model simulations of radiative forcing and large-scale temperature change." *Agricultural and Forest Meteorology* 142.2-4, pp. 216–233.

Bokaie, M., M. K. Zarkesh, P. D. Arasteh, and A. Hosseini (May 2016). "Assessment of Urban Heat Island based on the relationship between land surface temperature and Land Use/ Land Cover in Tehran." *Sustainable Cities and Society* 23, pp. 94–104.

Brown, C. F., S. P. Brumby, B. Guzder-Williams, T. Birch, S. B. Hyde, J. Mazzariello, W. Czerwinski, V. J. Pasquarella, R. Haertel, S. Ilyushchenko, K. Schwehr, M. Weisse, F. Stolle, C. Hanson, O. Guinan, R. Moore, and A. M. Tait (June 2022). "Dynamic World, Near real-time global 10m land use land cover mapping." *Scientific Data* 9.1, p. 251.

Buchhorn, M., M. Lesiv, N.-E. Tsendbazar, M. Herold, L. Bertels, and B. Smets (Mar. 2020). "Copernicus Global Land Cover Layers—Collection 2." *Remote Sensing* 12.6, p. 1044.

Chen, J., X. Zhu, J. E. Vogelmann, F. Gao, and S. Jin (Apr. 2011). "A simple and effective method for filling gaps in Landsat ETM+ SLC-off images." *Remote Sensing of Environment* 115.4, pp. 1053–1064.

Clinton, N. and P. Gong (July 2013). "MODIS detected surface urban heat islands and sinks: Global locations and controls." *Remote Sensing of Environment* 134, pp. 294–304.

Copernicus Climate Change Service, C. D. S. (2019). "Land cover classification gridded maps from 1992 to present derived from satellite observation." *Copernicus Climate Change Service (C3S) Climate Data Store (CDS)*.

Defourny, P. ESA Land Cover CCI project team; (2019). *ESA Land Cover Climate Change Initiative (Land_Cover_cci): Global (2019) Land Cover Maps, Version 2.0.7. Centre for Environmental Data Analysis*.

Defourny P., Lamarche C., Bontemps S., De Maet T., Van Bogaert E., Moreau I., Brockmann C., Boettcher M., Kirches G., Wevers J., and Santoro M. (2017). *Land Cover CCI: Product User Guide Version 2.0 (2017)*.

Donlon, C., B. Berruti, A. Buongiorno, M.-H. Ferreira, P. Féménias, J. Frerick, P. Goryl, U. Klein, H. Laur, C. Mavrocordatos, J. Nieke, H. Rebhan, B. Seitz, J. Stroede, and R. Sciarra (May 2012). "The Global Monitoring for Environment and Security (GMES) Sentinel-3 mission." *Remote Sensing of Environment* 120, pp. 37–57.

Duan, S.-B., Z.-L. Li, and P. Leng (June 2017). "A framework for the retrieval of all-weather land surface temperature at a high spatial resolution from polar-orbiting thermal infrared and passive microwave data." *Remote Sensing of Environment* 195, pp. 107–117.

Duan, S.-B., Z.-L. Li, B.-H. Tang, H. Wu, and R. Tang (Jan. 2014). "Generation of a time-consistent land surface temperature product from MODIS data." *Remote Sensing of Environment* 140, pp. 339–349.

Duan, S.-B., Z.-L. Li, W. Zhao, P. Wu, C. Huang, X.-J. Han, M. Gao, P. Leng, and G. Shang (May 2021). "Validation of Landsat land surface temperature product in the conterminous United

States using in situ measurements from SURFRAD, ARM, and NDBC sites." *International Journal of Digital Earth* 14.5, pp. 640–660.

Duguay-Tetzlaff, A., V. Bento, F. Göttsche, R. Stöckli, J. Martins, I. Trigo, F. Olesen, J. Bojanowski, C. Da Camara, and H. Kunz (Oct. 2015). "Meteosat Land Surface Temperature Climate Data Record: Achievable Accuracy and Potential Uncertainties." *Remote Sensing* 7.10, pp. 13139–13156.

Eleftheriou, D., K. Kiachidis, G. Kalmintzis, A. Kalea, C. Bantasis, P. Koumadoraki, M. E. Spathara, A. Tsolaki, M. I. Tzampazidou, and A. Gemitzi (Mar. 2018). "Determination of annual and seasonal daytime and nighttime trends of MODIS LST over Greece - climate change implications." *Science of The Total Environment* 616-617, pp. 937–947.

ESA—European Space Agency (2014). "CCI Land Cover Product User Guide version 2.4." *ESA CCI LC project*.

Feng, S., A. Wehrlé, J. M. Cook, A. M. Anesio, J. E. Box, L. G. Benning, and M. Tranter (June 2024). "The apparent effect of orbital drift on time series of MODIS MOD10A1 albedo on the Greenland ice sheet." *Science of Remote Sensing* 9, p. 100116.

Friedl, M, J Gray, and D Sulla-Menashe (2022). "MODIS/Terra+Aqua Land Cover Dynamics Yearly L3 Global 500m SIN Grid V061." *NASA EOSDIS Land Processes DAAC*.

Fu, P. and Q. Weng (Oct. 2016). "Consistent land surface temperature data generation from irregularly spaced Landsat imagery." *Remote Sensing of Environment* 184, pp. 175–187.

Gallego, F. J. (Aug. 2004). "Remote sensing and land cover area estimation." *International Journal of Remote Sensing* 25.15, pp. 3019–3047.

Gallo, K. and P. Krishnan (Oct. 2022). "Evaluation of the Bias in the Use of Clear-Sky Compared with All-Sky Observations of Monthly and Annual Daytime Land Surface Temperature." *Journal of Applied Meteorology and Climatology* 61.10, pp. 1485–1495.

Ghaderpour, E., P. Mazzanti, F. Bozzano, and G. Scarascia Mugnozza (June 2024). "Trend Analysis of MODIS Land Surface Temperature and Land Cover in Central Italy." *Land* 13.6, p. 796.

Ghent, D., K Veal, and M. Perry (June 2022). "ESA Land Surface Temperature Climate Change Initiative (LST_cci): Monthly land surface temperature from MODIS (Moderate resolution Infrared Spectroradiometer) on Aqua, level 3 collated (L3C) global product (2002-2018), version 3.00." *NERC EDS Centre for Environmental Data Analysis*.

Gök, D. T., D. Scherler, and H. Wulf (May 2024). *Land surface temperature trends derived from Landsat imagery in the Swiss Alps*.

Gorelick, N., M. Hancher, M. Dixon, S. Ilyushchenko, D. Thau, and R. Moore (Dec. 2017). "Google Earth Engine: Planetary-scale geospatial analysis for everyone." *Remote Sensing of Environment* 202, pp. 18–27.

Goward, S., T. Arvidson, D. Williams, J. Faundeen, J. Irons, and S. Franks (Oct. 2006). "Historical Record of Landsat Global Coverage." *Photogrammetric Engineering & Remote Sensing* 72.10, pp. 1155–1169.

Guzinski, R., M. C. Anderson, W. P. Kustas, H. Nieto, and I. Sandholt (July 2013). "Using a thermal-based two source energy balance model with time-differencing to estimate surface energy fluxes with day–night MODIS observations." *Hydrology and Earth System Sciences* 17.7, pp. 2809–2825.

Hain, C. R. and M. C. Anderson (Oct. 2017). “Estimating morning change in land surface temperature from MODIS day/night observations: Applications for surface energy balance modeling.” *Geophysical Research Letters* 44.19, pp. 9723–9733.

Hashim, B. M., A. Al Maliki, M. A. Sultan, S. Shahid, and Z. M. Yaseen (June 2022). “Effect of land use land cover changes on land surface temperature during 1984–2020: a case study of Baghdad city using landsat image.” *Natural Hazards* 112.2, pp. 1223–1246.

Hemati, M., M. Hasanlou, M. Mahdianpari, and F. Mohammadimanesh (July 2021). “A Systematic Review of Landsat Data for Change Detection Applications: 50 Years of Monitoring the Earth.” *Remote Sensing* 13.15, p. 2869.

Huang, J., Q. Li, and Z. Song (Apr. 2022). “Historical global land surface air apparent temperature and its future changes based on CMIP6 projections.” *Science of The Total Environment* 816, p. 151656.

Hulley, G and S Hook (2017). “MOD21A1D MODIS/Terra Land Surface Temperature/3-Band Emissivity Daily L3 Global 1km SIN Grid Day Night V006.” *NASA EOSDIS Land Processes Distributed Active Archive Center*.

Hulley, G. C. and S. J. Hook (Apr. 2011). “Generating Consistent Land Surface Temperature and Emissivity Products Between ASTER and MODIS Data for Earth Science Research.” *IEEE Transactions on Geoscience and Remote Sensing* 49.4, pp. 1304–1315.

Imran, H. M., A. Hossain, A. K. M. S. Islam, A. Rahman, M. A. E. Bhuiyan, S. Paul, and A. Alam (Sept. 2021). “Impact of Land Cover Changes on Land Surface Temperature and Human Thermal Comfort in Dhaka City of Bangladesh.” *Earth Systems and Environment* 5.3, pp. 667–693.

Jiang, L. and L. Yu (Oct. 2019). “Analyzing land use intensity changes within and outside protected areas using ESA CCI-LC datasets.” *Global Ecology and Conservation* 20, e00789.

Johnson, B. (Oct. 2015). “Scale Issues Related to the Accuracy Assessment of Land Use/Land Cover Maps Produced Using Multi-Resolution Data: Comments on “The Improvement of Land Cover Classification by Thermal Remote Sensing”. Remote Sens. 2015, 7(7), 8368–8390.” *Remote Sensing* 7.10, pp. 13436–13439.

Kuenzer, C. and S. Dech (2013). *Thermal Infrared Remote Sensing*. Ed. by C. Kuenzer and S. Dech. Vol. 17. Dordrecht: Springer Netherlands.

Li, W., P. Ciais, N. MacBean, S. Peng, P. Defourny, and S. Bontemps (May 2016a). “Major forest changes and land cover transitions based on plant functional types derived from the ESA CCI Land Cover product.” *International Journal of Applied Earth Observation and Geoinformation* 47, pp. 30–39.

Li, Y., M. Zhao, D. J. Mildrexler, S. Motesharrei, Q. Mu, E. Kalnay, F. Zhao, S. Li, and K. Wang (Dec. 2016b). “Potential and Actual impacts of deforestation and afforestation on land surface temperature.” *Journal of Geophysical Research: Atmospheres* 121.24.

Li, Z.-L., B.-H. Tang, H. Wu, H. Ren, G. Yan, Z. Wan, I. F. Trigo, and J. A. Sobrino (Apr. 2013). “Satellite-derived land surface temperature: Current status and perspectives.” *Remote Sensing of Environment* 131, pp. 14–37.

Liang, D., Y. Zuo, L. Huang, J. Zhao, L. Teng, and F. Yang (Nov. 2015). “Evaluation of the Consistency of MODIS Land Cover Product (MCD12Q1) Based on Chinese 30 m GlobeLand30

Datasets: A Case Study in Anhui Province, China." *ISPRS International Journal of Geo-Information* 4.4, pp. 2519–2541.

Liang, L., Q. Liu, G. Liu, H. Li, and C. Huang (June 2019). "Accuracy Evaluation and Consistency Analysis of Four Global Land Cover Products in the Arctic Region." *Remote Sensing* 11.12, p. 1396.

Liu, B., Z. Zhang, L. Pan, Y. Sun, S. Ji, X. Guan, J. Li, and M. Xu (May 2023). "Comparison of Various Annual Land Cover Datasets in the Yellow River Basin." *Remote Sensing* 15.10, p. 2539.

Liu, J., D. F. T. Hagan, and Y. Liu (Dec. 2020). "Global Land Surface Temperature Change (2003–2017) and Its Relationship with Climate Drivers: AIRS, MODIS, and ERA5-Land Based Analysis." *Remote Sensing* 13.1, p. 44.

Liu, X., L. Yu, W. Li, D. Peng, L. Zhong, L. Li, Q. Xin, H. Lu, C. Yu, and P. Gong (Oct. 2018). "Comparison of country-level cropland areas between ESA-CCI land cover maps and FAOSTAT data." *International Journal of Remote Sensing* 39.20, pp. 6631–6645.

LUINTEL, N., W. MA, Y. MA, B. WANG, and S. SUBBA (Sept. 2019). "Spatial and temporal variation of daytime and nighttime MODIS land surface temperature across Nepal." *Atmospheric and Oceanic Science Letters* 12.5, pp. 305–312.

Ma, J., J. Zhou, F.-M. Göttsche, S. Liang, S. Wang, and M. Li (Dec. 2020). "A global long-term (1981–2000) land surface temperature product for NOAA AVHRR." *Earth System Science Data* 12.4, pp. 3247–3268.

Marzban, F., T. Conrad, P. Marzban, and S. Sodoudi (Feb. 2018). "Estimation of the Near-Surface Air Temperature during the Day and Nighttime from MODIS in Berlin, Germany." *International Journal of Advanced Remote Sensing and GIS* 7.1, pp. 2478–2517.

Masek, J. G., M. A. Wulder, B. Markham, J. McCorkel, C. J. Crawford, J. Storey, and D. T. Jenstrom (Oct. 2020). "Landsat 9: Empowering open science and applications through continuity." *Remote Sensing of Environment* 248, p. 111968.

Mentaschi, L., G. Duveiller, G. Zulian, C. Corbane, M. Pesaresi, J. Maes, A. Stocchino, and L. Feyen (Jan. 2022). "Global long-term mapping of surface temperature shows intensified intra-city urban heat island extremes." *Global Environmental Change* 72, p. 102441.

Mousivand, A. and J. J. Arsanjani (May 2019). "Insights on the historical and emerging global land cover changes: The case of ESA-CCI-LC datasets." *Applied Geography* 106, pp. 82–92.

Neinavaz, E., M. Schlerf, R. Darvishzadeh, M. Gerhards, and A. K. Skidmore (Oct. 2021). "Thermal infrared remote sensing of vegetation: Current status and perspectives." *International Journal of Applied Earth Observation and Geoinformation* 102, p. 102415.

Nichol, J. (May 2005). "Remote Sensing of Urban Heat Islands by Day and Night." *Photogrammetric Engineering & Remote Sensing* 71.5, pp. 613–621.

Nicholson, S. E. (Oct. 2015). "Evolution and current state of our understanding of the role played in the climate system by land surface processes in semi-arid regions." *Global and Planetary Change* 133, pp. 201–222.

Pan, X., Z. Wang, S. Liu, Z. Yang, R. Guluzade, Y. Liu, J. Yuan, and Y. Yang (May 2024). "The impact of clear-sky biases of land surface temperature on monthly evapotranspiration estimation." *International Journal of Applied Earth Observation and Geoinformation* 129, p. 103811.

Peng, S.-S., S. Piao, Z. Zeng, P. Ciais, L. Zhou, L. Z. X. Li, R. B. Myneni, Y. Yin, and H. Zeng (Feb. 2014). "Afforestation in China cools local land surface temperature." *Proceedings of the National Academy of Sciences* 111.8, pp. 2915–2919.

Peng Fu and Qihao Weng (Oct. 2015). "Temporal Dynamics of Land Surface Temperature From Landsat TIR Time Series Images." *IEEE Geoscience and Remote Sensing Letters* 12.10, pp. 2175–2179.

Polasek, W. (Aug. 2013). "Time Series Analysis and Its Applications: With R Examples, Third Edition by Robert H. Shumway, David S. Stoffer." *International Statistical Review* 81.2, pp. 323–325.

Popp, T., M. I. Hegglin, R. Hollmann, F. Ardhuin, A. Bartsch, A. Bastos, V. Bennett, J. Boutin, C. Brockmann, M. Buchwitz, E. Chuvieco, P. Ciais, W. Dorigo, D. Ghent, R. Jones, T. Lavergne, C. J. Merchant, B. Meyssignac, F. Paul, S. Quegan, S. Sathyendranath, T. Scanlon, M. Schröder, S. G. H. Simis, and U. Willén (Nov. 2020). "Consistency of Satellite Climate Data Records for Earth System Monitoring." *Bulletin of the American Meteorological Society* 101.11, E1948–E1971.

Qin, J., M. He, H. Jiang, and N. Lu (Dec. 2022). "Reconstruction of 60-year (1961–2020) surface air temperature on the Tibetan Plateau by fusing MODIS and ERA5 temperatures." *Science of The Total Environment* 853, p. 158406.

Qiu, S., Z. Zhu, R. Shang, and C. J. Crawford (Dec. 2021). "Can Landsat 7 preserve its science capability with a drifting orbit?" *Science of Remote Sensing* 4, p. 100026.

Rindfuss, R. R., S. J. Walsh, B. L. Turner, J. Fox, and V. Mishra (Sept. 2004). "Developing a science of land change: Challenges and methodological issues." *Proceedings of the National Academy of Sciences* 101.39, pp. 13976–13981.

Salomonson, V., B. Guenther, and E. Masuoka (2001). "A summary of the status of the EOS Terra mission Moderate Resolution Imaging Spectroradiometer (MODIS) and attendant data product development after one year of on-orbit performance." *IGARSS 2001. Scanning the Present and Resolving the Future. Proceedings. IEEE 2001 International Geoscience and Remote Sensing Symposium (Cat. No.01CH37217)*. IEEE, pp. 1197–1199.

Savtchenko, A, D Ouzounov, S Ahmad, J Acker, G Leptoukh, J Koziana, and D Nickless (Jan. 2004). "Terra and Aqua MODIS products available from NASA GES DAAC." *Advances in Space Research* 34.4, pp. 710–714.

Sekertekin, A. and S. Bonafoni (Aug. 2020). "Sensitivity Analysis and Validation of Daytime and Nighttime Land Surface Temperature Retrievals from Landsat 8 Using Different Algorithms and Emissivity Models." *Remote Sensing* 12.17, p. 2776.

Shawky, M., M. R. Ahmed, E. Ghaderpour, A. Gupta, G. Achari, A. Dewan, and Q. K. Hassan (May 2023). "Remote sensing-derived land surface temperature trends over South Asia." *Ecological Informatics* 74, p. 101969.

Sobrino, J. A., F. Del Frate, M. Drusch, J. C. Jimenez-Munoz, P. Manunta, and A. Regan (May 2016). "Review of Thermal Infrared Applications and Requirements for Future High-Resolution Sensors." *IEEE Transactions on Geoscience and Remote Sensing* 54.5, pp. 2963–2972.

Sobrino, J. A., Y. Julien, and S. García-Monteiro (Jan. 2020). "Surface Temperature of the Planet Earth from Satellite Data." *Remote Sensing* 12.2, p. 218.

Sulla-Menashe, D., J. M. Gray, S. P. Abercrombie, and M. A. Friedl (Mar. 2019). "Hierarchical mapping of annual global land cover 2001 to present: The MODIS Collection 6 Land Cover product." *Remote Sensing of Environment* 222, pp. 183–194.

Sun, H., Y. Chen, A. Gong, X. Zhao, W. Zhan, and M. Wang (Oct. 2014). "Estimating mean air temperature using MODIS day and night land surface temperatures." *Theoretical and Applied Climatology* 118.1-2, pp. 81–92.

Sun, H., X. Zhao, Y. Chen, A. Gong, and J. Yang (Dec. 2013). "A new agricultural drought monitoring index combining MODIS NDWI and day–night land surface temperatures: a case study in China." *International Journal of Remote Sensing* 34.24, pp. 8986–9001.

Sun, L. and K. Schulz (June 2015). "The Improvement of Land Cover Classification by Thermal Remote Sensing." *Remote Sensing* 7.7, pp. 8368–8390.

Sun, W., X. Ding, J. Su, X. Mu, Y. Zhang, P. Gao, and G. Zhao (Aug. 2022). "Land use and cover changes on the Loess Plateau: A comparison of six global or national land use and cover datasets." *Land Use Policy* 119, p. 106165.

Turner, B. L., E. F. Lambin, and A. Reenberg (Dec. 2007). "The emergence of land change science for global environmental change and sustainability." *Proceedings of the National Academy of Sciences* 104.52, pp. 20666–20671.

Vinutha, H. P., B. Poornima, and B. M. Sagar (2018). "Detection of Outliers Using Interquartile Range Technique from Intrusion Dataset," pp. 511–518.

Waldner, F. and P. Defourny (Aug. 2017). "Where can pixel counting area estimates meet user-defined accuracy requirements?" *International Journal of Applied Earth Observation and Geoinformation* 60, pp. 1–10.

Wan, X., W. Wang, J. Liu, and T. Tong (Dec. 2014). "Estimating the sample mean and standard deviation from the sample size, median, range and/or interquartile range." *BMC Medical Research Methodology* 14.1, p. 135.

Wan, Z., Y. Zhang, Q. Zhang, and Z.-l. Li (Nov. 2002). "Validation of the land-surface temperature products retrieved from Terra Moderate Resolution Imaging Spectroradiometer data." *Remote Sensing of Environment* 83.1-2, pp. 163–180.

Wang, Q., Y. Tang, X. Tong, and P. M. Atkinson (May 2024). "Filling gaps in cloudy Landsat LST product by spatial-temporal fusion of multi-scale data." *Remote Sensing of Environment* 306, p. 114142.

Wang, T., J. Shi, Y. Ma, H. Letu, and X. Li (Mar. 2020). "All-sky longwave downward radiation from satellite measurements: General parameterizations based on LST, column water vapor and cloud top temperature." *ISPRS Journal of Photogrammetry and Remote Sensing* 161, pp. 52–60.

Wijedasa, L. S., S. Sloan, D. G. Michelakis, and G. R. Clements (Sept. 2012). "Overcoming Limitations with Landsat Imagery for Mapping of Peat Swamp Forests in Sundaland." *Remote Sensing* 4.9, pp. 2595–2618.

Williams, D. L., S. Goward, and T. Arvidson (Oct. 2006). "Landsat." *Photogrammetric Engineering & Remote Sensing* 72.10, pp. 1171–1178.

Wulder, M. A., T. R. Loveland, D. P. Roy, C. J. Crawford, J. G. Masek, C. E. Woodcock, R. G. Allen, M. C. Anderson, A. S. Belward, W. B. Cohen, J. Dwyer, A. Erb, F. Gao, P. Griffiths, D. Helder, T. Hermosilla, J. D. Hipple, P. Hostert, M. J. Hughes, J. Huntington, D. M. Johnson, R. Kennedy,

A. Kilic, Z. Li, L. Lymburner, J. McCorkel, N. Pahlevan, T. A. Scambos, C. Schaaf, J. R. Schott, Y. Sheng, J. Storey, E. Vermote, J. Vogelmann, J. C. White, R. H. Wynne, and Z. Zhu (May 2019). "Current status of Landsat program, science, and applications." *Remote Sensing of Environment* 225, pp. 127–147.

Wulder, M. A., S. M. Ortlepp, J. C. White, and S. Maxwell (Jan. 2008a). "Evaluation of Landsat-7 SLC-off image products for forest change detection." *Canadian Journal of Remote Sensing* 34.2, pp. 93–99.

Wulder, M. A., D. P. Roy, V. C. Radeloff, T. R. Loveland, M. C. Anderson, D. M. Johnson, S. Healey, Z. Zhu, T. A. Scambos, N. Pahlevan, M. Hansen, N. Gorelick, C. J. Crawford, J. G. Masek, T. Hermosilla, J. C. White, A. S. Belward, C. Schaaf, C. E. Woodcock, J. L. Huntington, L. Lymburner, P. Hostert, F. Gao, A. Lyapustin, J.-F. Pekel, P. Strobl, and B. D. Cook (Oct. 2022). "Fifty years of Landsat science and impacts." *Remote Sensing of Environment* 280, p. 113195.

Wulder, M. A., J. C. White, S. N. Goward, J. G. Masek, J. R. Irons, M. Herold, W. B. Cohen, T. R. Loveland, and C. E. Woodcock (Mar. 2008b). "Landsat continuity: Issues and opportunities for land cover monitoring." *Remote Sensing of Environment* 112.3, pp. 955–969.

Wulder, M. A., J. C. White, J. G. Masek, J. Dwyer, and D. P. Roy (Feb. 2011). "Continuity of Landsat observations: Short term considerations." *Remote Sensing of Environment* 115.2, pp. 747–751.

Xing, Z., Z.-L. Li, S.-B. Duan, X. Liu, X. Zheng, P. Leng, M. Gao, X. Zhang, and G. Shang (Aug. 2021). "Estimation of daily mean land surface temperature at global scale using pairs of daytime and nighttime MODIS instantaneous observations." *ISPRS Journal of Photogrammetry and Remote Sensing* 178, pp. 51–67.

Xu, S., D. Wang, S. Liang, Y. Liu, and A. Jia (June 2023). "Assessment of gridded datasets of various near surface temperature variables over Heihe River Basin: Uncertainties, spatial heterogeneity and clear-sky bias." *International Journal of Applied Earth Observation and Geoinformation* 120, p. 103347.

Yao, R., L. Wang, S. Wang, L. Wang, J. Wei, J. Li, and D. Yu (Dec. 2020). "A detailed comparison of MYD11 and MYD21 land surface temperature products in mainland China." *International Journal of Digital Earth* 13.12, pp. 1391–1407.

Yu, P., T. Zhao, J. Shi, Y. Ran, L. Jia, D. Ji, and H. Xue (Apr. 2022). "Global spatiotemporally continuous MODIS land surface temperature dataset." *Scientific Data* 9.1, p. 143.

Zhang, H. and D. Roy (Dec. 2016). "Landsat 5 Thematic Mapper reflectance and NDVI 27-year time series inconsistencies due to satellite orbit change." *Remote Sensing of Environment* 186, pp. 217–233.

Zhang, H., F. Zhang, M. Ye, T. Che, and G. Zhang (Oct. 2016). "Estimating daily air temperatures over the Tibetan Plateau by dynamically integrating MODIS LST data." *Journal of Geophysical Research: Atmospheres* 121.19.

Zhang, X., M. A. Friedl, C. B. Schaaf, A. H. Strahler, J. C. Hodges, F. Gao, B. C. Reed, and A. Huete (Mar. 2003). "Monitoring vegetation phenology using MODIS." *Remote Sensing of Environment* 84.3, pp. 471–475.

Zhao, B., K. Mao, Y. Cai, J. Shi, Z. Li, Z. Qin, X. Meng, X. Shen, and Z. Guo (Oct. 2020). "A combined Terra and Aqua MODIS land surface temperature and meteorological station data product for China from 2003 to 2017." *Earth System Science Data* 12.4, pp. 2555–2577.

Zhao, Q., L. Yu, X. Li, D. Peng, Y. Zhang, and P. Gong (Sept. 2021). “Progress and Trends in the Application of Google Earth and Google Earth Engine.” *Remote Sensing* 13.18, p. 3778.

Zhao, W., H. Wu, G. Yin, and S.-B. Duan (June 2019). “Normalization of the temporal effect on the MODIS land surface temperature product using random forest regression.” *ISPRS Journal of Photogrammetry and Remote Sensing* 152, pp. 109–118.

Zhu, Z. and C. E. Woodcock (Mar. 2014). “Continuous change detection and classification of land cover using all available Landsat data.” *Remote Sensing of Environment* 144, pp. 152–171.

7 Appendices

7.1 Code

The code can be accessed from the GitHub repository: `https://github.com/lerren144/UZH-Master-Thesis.git`

7.1.1 MODIS LST and visualization

All the scripts provided in text file format were extracted directly from Google Earth Engine. These scripts contain the code used for processing the harmonics and extracting the MODIS LST Products.

7.1.1.1 MODIS LST global coverage

Google Earth Engine Code Editor: `https://code.earthengine.google.com/a4cc8f8b94e8bd6cfbb1b37854a200b1`
GitHub Repository: `https://github.com/lerren144/UZH-Master-Thesis/blob/32b2d3cfb849a11779f093e3e67c9bb760159e1c/1.%20MODIS%20LST%20and%20Visualization/1.1%20MODIS%20LST%20Global%20Coverage.txt`

7.1.1.2 MODIS LST divided global coverage

Google Earth Engine Code Editor: `https://code.earthengine.google.com/011b0909ddea608c5660b4cd632a9cfd`
GitHub Repository: `https://github.com/lerren144/UZH-Master-Thesis/blob/32b2d3cfb849a11779f093e3e67c9bb760159e1c/1.%20MODIS%20LST%20and%20Visualization/1.2%20MODIS%20LST%20Divided%20Global%20Coverage.txt`

7.1.1.3 MODIS satellite image visualization

Google Earth Engine Code Editor: `https://code.earthengine.google.com/d0d4b84d72ef78c535e87151903e6cc9`
GitHub Repository: `https://github.com/lerren144/UZH-Master-Thesis/blob/32b2d3cfb849a11779f093e3e67c9bb760159e1c/1.%20MODIS%20LST%20and%20Visualization/1.3%20MODIS%20Satellite%20Image%20Visualization.txt`

7.1.2 Land surface temperature scripts

The folder contains all the scripts for LST mosaicking, generating the LST difference images, generating the LST combination images, and extracting the LST from the LC - creating transition matrix.

7.1.2.1 MODIS LST mosaicking script (Pre-processing)

The folder contains all the scripts used to mosaic the MODIS LST (Land Surface Temperature) products exported from Google Earth Engine. These scripts ensure the proper merging of datasets into a single mosaic image for further analysis.
GitHub Repository: `https://github.com/lerren144/UZH-Master-Thesis/tree/32b2d3cfb849a11779f093e3e67c9bb760159e1c/2.%20Land%20Surface%20Temperature%20Scripts/2.1.%20MODIS%20LST%20Mosaicking%20Script%20(Pre-Processing)`

7.1.2.2 MODIS LST difference script

The folder contains all the scripts used to calculate the differences between the mosaicked MODIS LST product images: End Period and Start Period.
GitHub Repository: `https://github.com/lerren144/UZH-Master-Thesis/tree/32b2d3cfb849a11779f093e3e67c9bb760159e1c/2.%20Land%20Surface%20Temperature%20Scripts/2.2.%20MODIS%20LST%20Difference%20Script%3A`

7.1.2.3 MODIS LST combination script

The folder contains all the scripts used to combine the mosaicked MODIS LST product images using three methods: Combination 1: Linear Regression Equation, Combination 2: Average MODIS Terra Aqua Day, Combination 3: Average MODIS Terra Aqua Night.
GitHub Repository: `https://github.com/lerren144/UZH-Master-Thesis/tree/32b2d3cfb849a11779f093e3e67c9bb760159e1c/2.%20Land%20Surface%20Temperature%20Scripts/2.3%20MODIS%20LST%20Combination%20Script`

7.1.3 Undisturbed areas LST extraction script

The folder contains all the scripts used to extract LST values from the undisturbed land cover mask. Additionally, the reference scripts include the trial-and-error scripts that were initially tested and refined during the development process.
GitHub Repository: `https://github.com/lerren144/UZH-Master-Thesis/tree/f3a249aef9f44e5dd8b41a86bf1e29a3b394e7c9/3.%20Undisturbed%20Areas%20LST%20Extraction%20Script`

7.1.4 LST visualization per latitude script

The folder contains all the scripts used to create visualization plots for extracting LST pixel values across different latitudes. These scripts are designed to analyze and represent the spatial distribution of LST data effectively in each latitude.

GitHub Repository: `https://github.com/lerren144/UZH-Master-Thesis/tree/f3a249aef9f44e5dd8b41a86bf1e29a3b394e7c9/4.%20LST%20Visualization%20per%20Latitude%20Script`

7.1.5 LST visualization per latitude script

The folder contains all the scripts used to extract the ESA CCI LC masks for disturbed and undisturbed areas, preprocess the LC masks, and generate various visualizations, including charts, transition matrices, bubble plots, and Sankey diagrams. These scripts play a crucial role in analyzing and visualizing land cover changes effectively.

GitHub Repository: `https://github.com/lerren144/UZH-Master-Thesis/tree/329ce443f9a1fa1b4ee050b5693a6c5adce48af3/5.%20ESA%20CCI%20Land%20Cover%20Scripts`

7.1.5.1 ESA CCI land cover disturbed and undisturbed analysis (Extraction of masks)

GitHub Repository: `https://github.com/lerren144/UZH-Master-Thesis/blob/722d18aca23de02e8658ac09d0dc3ed51452de64/5.%20ESA%20CCI%20Land%20Cover%20Scripts/5.1.%20%20ESACCI_LandCover_Analysis.ipynb`

7.1.5.2 ESA CCI land cover conversion from NETCDF4 to GeoTIFF (Pre-processing)

GitHub Repository: `https://github.com/lerren144/UZH-Master-Thesis/blob/722d18aca23de02e8658ac09d0dc3ed51452de64/5.%20ESA%20CCI%20Land%20Cover%20Scripts/5.2.%20Conversion_ESACCILC_Geotiff.py`

7.1.5.3 ESA CCI LC before and after bar chart (Graph)

GitHub Repository: `https://github.com/lerren144/UZH-Master-Thesis/blob/722d18aca23de02e8658ac09d0dc3ed51452de64/5.%20ESA%20CCI%20Land%20Cover%20Scripts/5.3.%20ESACCI_LC_Before_After_BarChart_22x22.py`

7.1.5.4 ESA CCI LC transition matrix (Table)

GitHub Repository: `https://github.com/lerren144/UZH-Master-Thesis/blob/722d18aca23de02e8658ac09d0dc3ed51452de64/5.%20ESA%20CCI%20Land%20Cover%20Scripts/5.4.%20ESACCI_LC_Transition_Matrix_22x22.ipynb`

7.1.5.5 ESA CCI LC-LST bubble plot (Graph)

GitHub Repository: https://github.com/lerren144/UZH-Master-Thesis/blob/722d18aca23de02e8658ac09d0dc3ed51452de64/5.%20ESA%20CCI%20Land%20Cover%20Scripts/5.5.%20ESACCI_LC_LST_BubblePlot_22x22.py

7.1.5.6 ESA CCI LC-LST sankey diagram (Graph)

GitHub Repository: https://github.com/lerren144/UZH-Master-Thesis/blob/722d18aca23de02e8658ac09d0dc3ed51452de64/5.%20ESA%20CCI%20Land%20Cover%20Scripts/5.6.%20Sankey_Diagram_Copernicus_22x22.ipynb

7.1.6 LST visualization per latitude script

The folder contains all the scripts used to extract the MODIS LC masks for disturbed and undisturbed areas, preprocess the LC masks, and generate various visualizations, including charts, transition matrices, bubble plots, and Sankey diagrams. These scripts play a crucial role in analyzing and visualizing land cover changes effectively.
GitHub Repository: https://github.com/lerren144/UZH-Master-Thesis/tree/329ce443f9a1fa1b4ee050b5693a6c5adce48af3/6.%20MODIS%20Land%20Cover%20Scripts

7.1.6.1 MODIS LC disturbed and undisturbed analysis (Extraction of masks)

Google colab link: https://colab.research.google.com/drive/1ANxziJ66DZ1oyW0K0LhR4e_a3DXLc08h?usp=sharing
GitHub repository: https://github.com/lerren144/UZH-Master-Thesis/tree/329ce443f9a1fa1b4ee050b5693a6c5adce48af3/6.%20MODIS%20Land%20Cover%20Scripts/6.1.%20MODIS%20Land%20Cover%20Disturbed%20and%20Undisturbed%20Analysis%20(Extraction%20of%20Masks)

7.1.6.2 MODIS LC mosaicking script (Pre-processing)

GitHub Repository: https://github.com/lerren144/UZH-Master-Thesis/blob/722d18aca23de02e8658ac09d0dc3ed51452de64/6.%20MODIS%20Land%20Cover%20Scripts/6.2.%20MODIS_LC_Mosaic_Script.py

7.1.6.3 MODIS LC before and after bar chart (Graph)

GitHub Repository: https://github.com/lerren144/UZH-Master-Thesis/blob/722d18aca23de02e8658ac09d0dc3ed51452de64/6.%20MODIS%20Land%20Cover%20Scripts/6.3.%20MODIS_LC_Before_After_BarChart_10x10.py

7.1.6.4 MODIS LC transition matrix (Table)

GitHub Repository: `https://github.com/lerren144/UZH-Master-Thesis/blob/722d18aca23de02e8658ac09d0dc3ed51452de64/6.%20MODIS%20Land%20Cover%20Scripts/6.4.%20MODIS_LC_Transtion_Matrix_10x10.ipynb`

7.1.6.5 MODIS LC-LST bubble plot (Graph)

GitHub Repository: `https://github.com/lerren144/UZH-Master-Thesis/blob/722d18aca23de02e8658ac09d0dc3ed51452de64/6.%20MODIS%20Land%20Cover%20Scripts/6.5.%20MODIS_LC_LST_BubblePlot_10x10.py`

7.1.6.6 MODIS LC-LST sankey diagram (Graph)

GitHub Repository: `https://github.com/lerren144/UZH-Master-Thesis/blob/722d18aca23de02e8658ac09d0dc3ed51452de64/6.%20MODIS%20Land%20Cover%20Scripts/6.6.%20Sankey_Diagram_MODIS_10x10.ipynb`

7.2 Results: LC and LST using different timelines (2000 to 2020)

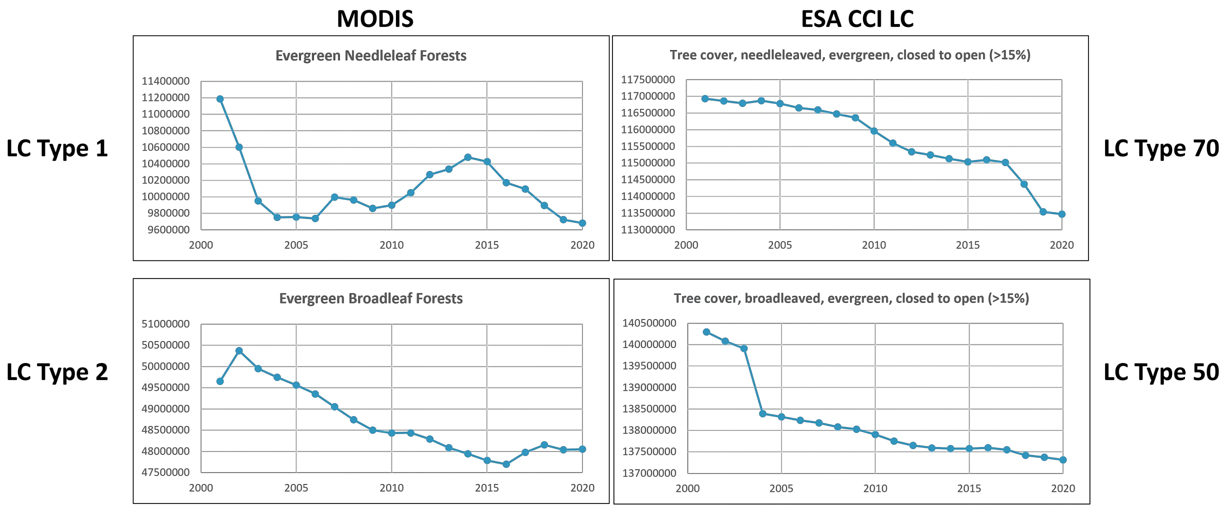

Figure 7.1: Yearly pixel count trends: Comparison of MODIS LC Type 1 and Type 2 with ESA CCI LC.

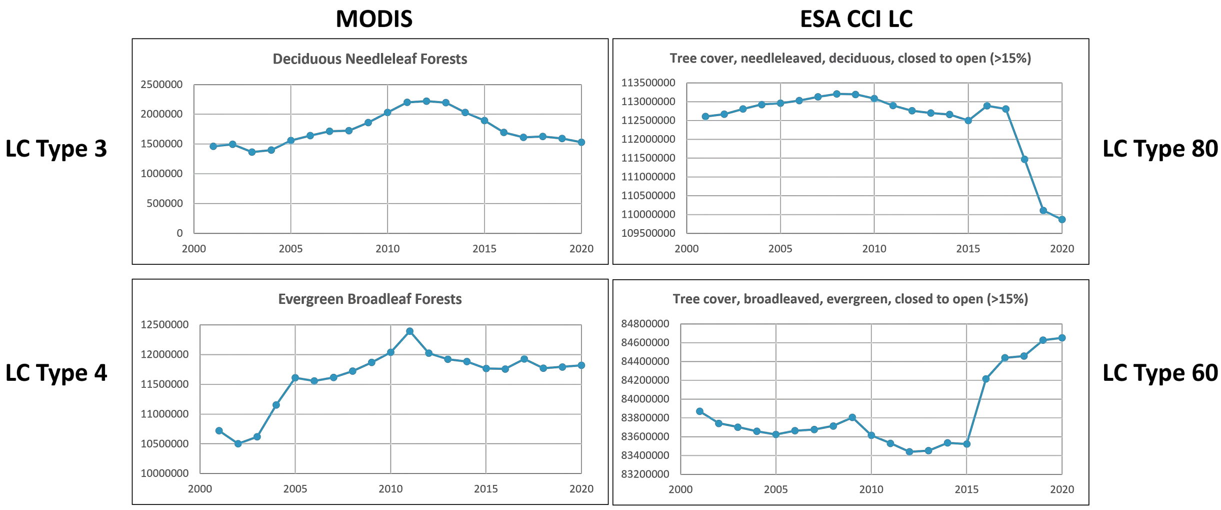

Figure 7.2: Yearly pixel count trends: Comparison of MODIS LC Type 3 and Type 4 with ESA CCI LC.

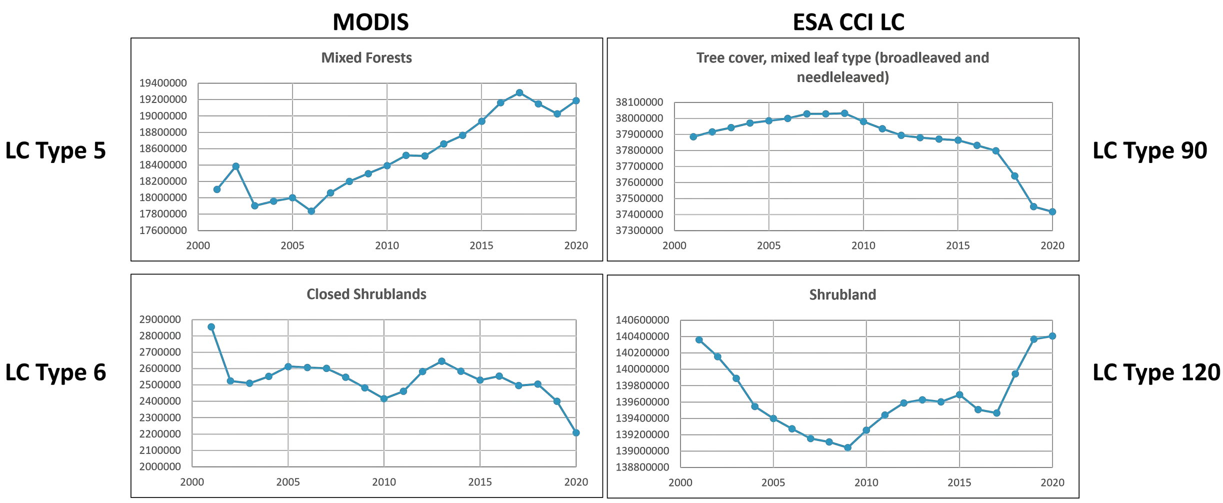

Figure 7.3: Yearly pixel count trends: Comparison of MODIS LC Type 5 and Type 6 with ESA CCI LC.

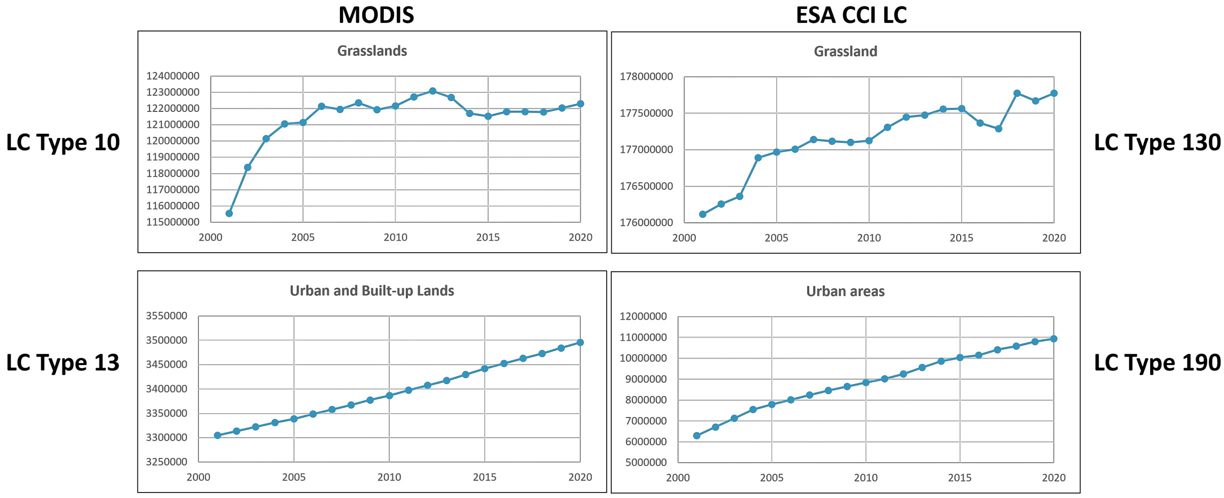

Figure 7.4: Yearly pixel count trends: Comparison of MODIS LC Type 10 and Type 13 with ESA CCI LC.

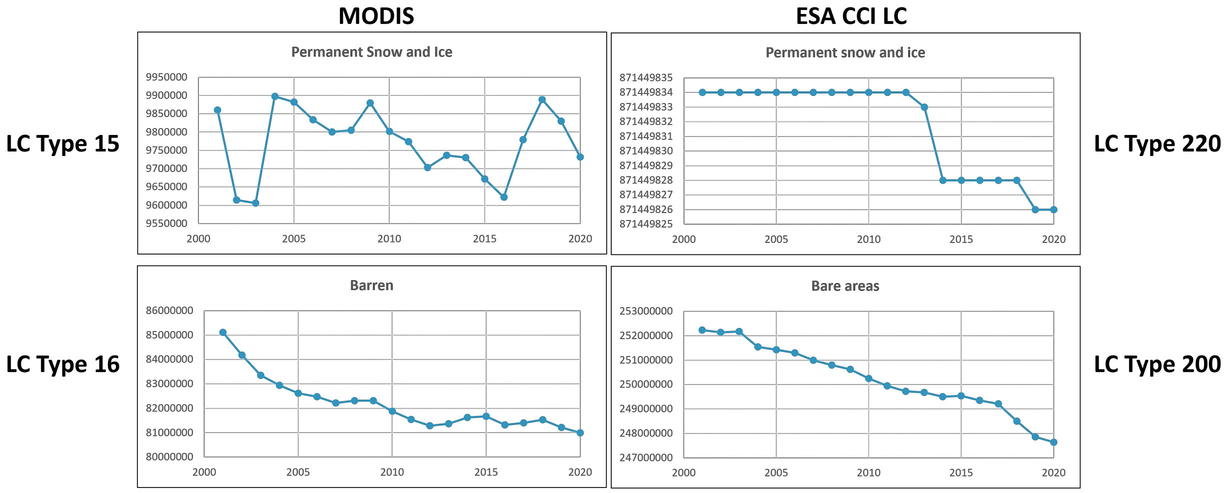

Figure 7.5: Yearly pixel count trends: Comparison of MODIS LC Type 15 and Type 16 with ESA CCI LC.

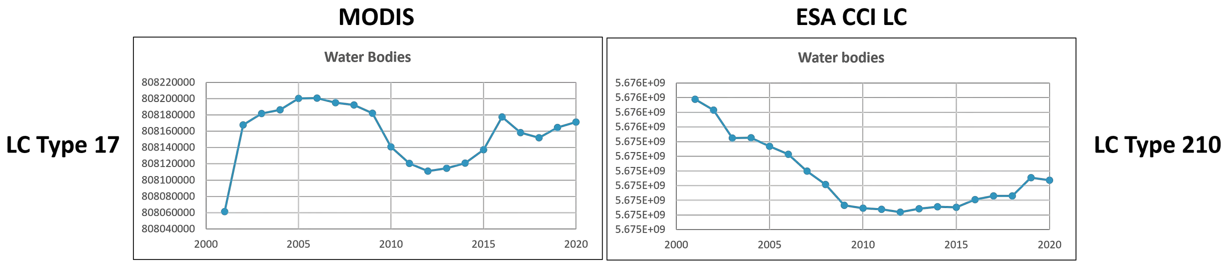

Figure 7.6: Yearly pixel count trends: Comparison of MODIS LC Type 17 with ESA CCI LC.

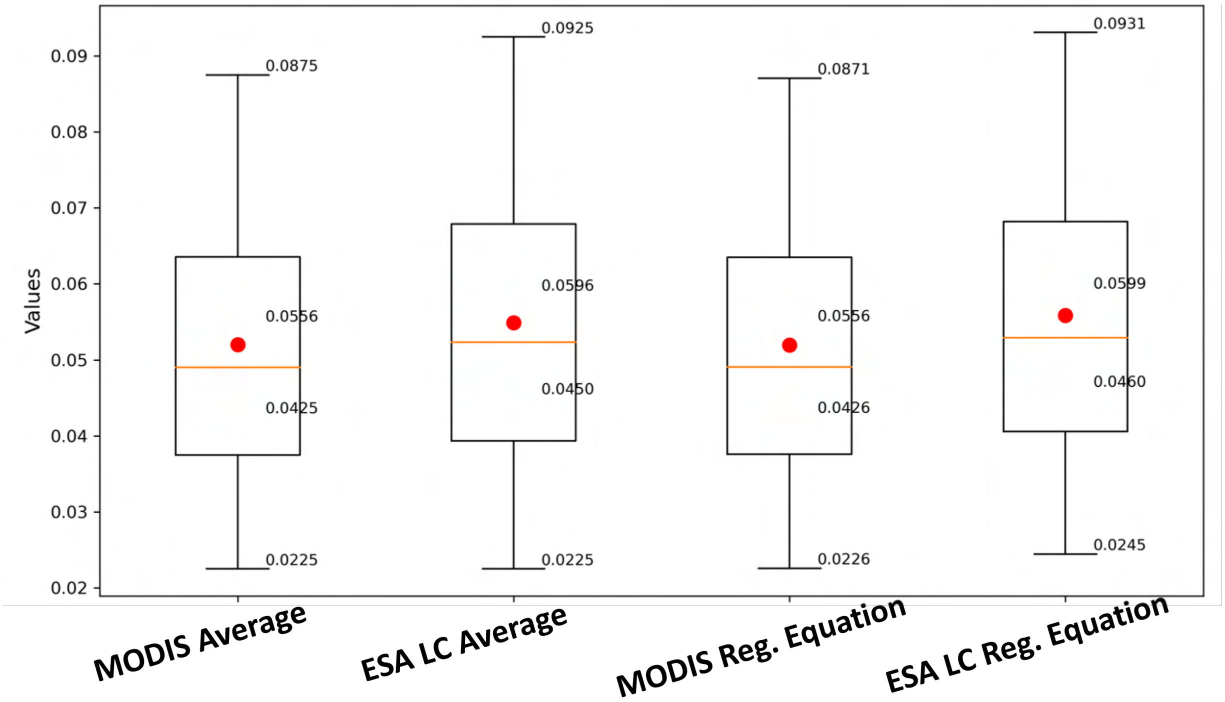

Figure 7.7: Undisturbed areas summary. MODIS and ESA LC average and regression equation (linear trend LST) (changed once 2000 to 2020).

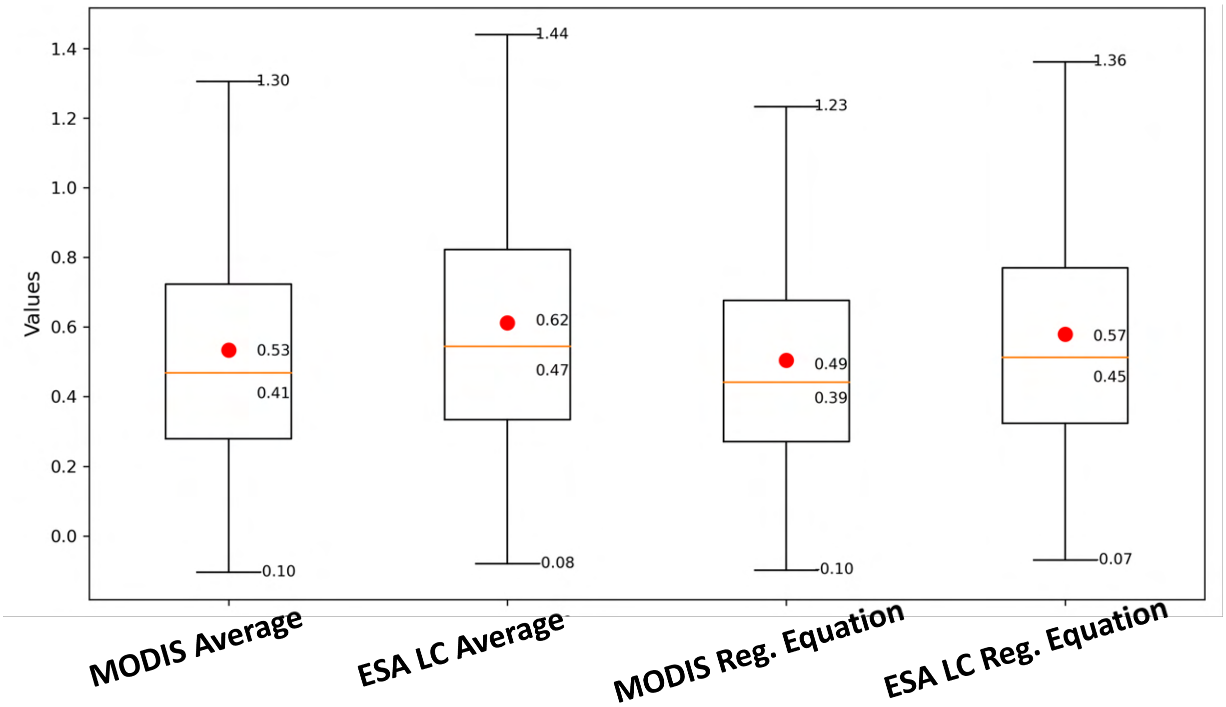

Figure 7.8: Undisturbed Areas Summary. MODIS and ESA LC average and regression equation (Difference of the mean LST) (changed once 2000 to 2020).

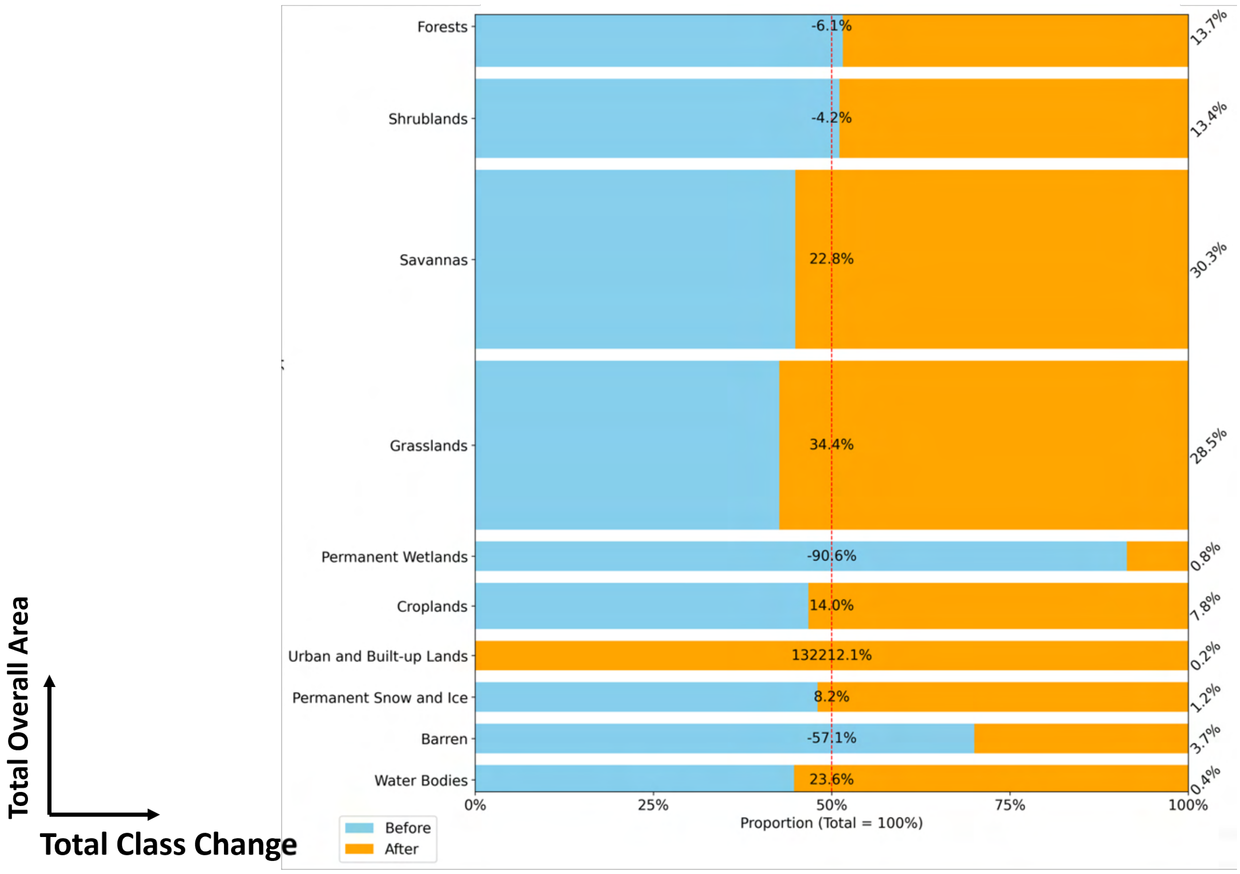

Figure 7.9: Aggregated MODIS LC type 1 global statistics (changed once 2001 to 2020).

	Forests	Shrublands	Savannas	Grasslands	Permanent Wetlands	Croplands	Urban and Built-up Lands	Permanent Snow and Ice	Barren	Water Bodies
Forests	0	8585.25	2403710	67050.5	14897.75	5958.75	34.25	53.75	40.25	778.25
Shrublands	2476.5	0	734070.5	1508163.25	1966	42460	331	186.5	95956.5	354.25
Savannas	2152621.25	357503	0	1344243	56261	285680.5	12051.5	81.5	1198.25	1303.25
Grasslands	34437.75	1257874.25	944110	0	17491.75	992936.25	4454.25	7084	366256.25	2289.75
Permanent Wetlands	148394.75	266330	526762.25	482724.25	0	3469	505.25	561	14318.5	22914.75
Croplands	10356.5	11997.25	555165.25	575589	1957.5	0	12000.5	30	354.5	255.25
Urban and Built-up Lands	0	0	3	19.75	0	0	0	0	0	0
Permanent Snow and Ice	10.25	234	0.75	28530	951.25	1.25	6	0	145929.25	10460
Barren	80.75	379665.5	3904.75	865328.5	26847.5	738	716.5	182914.75	0	30298.25
Water Bodies	560.5	3074.5	4065.5	4734	17823	8.5	1.75	10390.75	14871.25	0

Figure 7.10: Aggregated MODIS LC type 1 transition matrix (changed once 2001 to 2020).

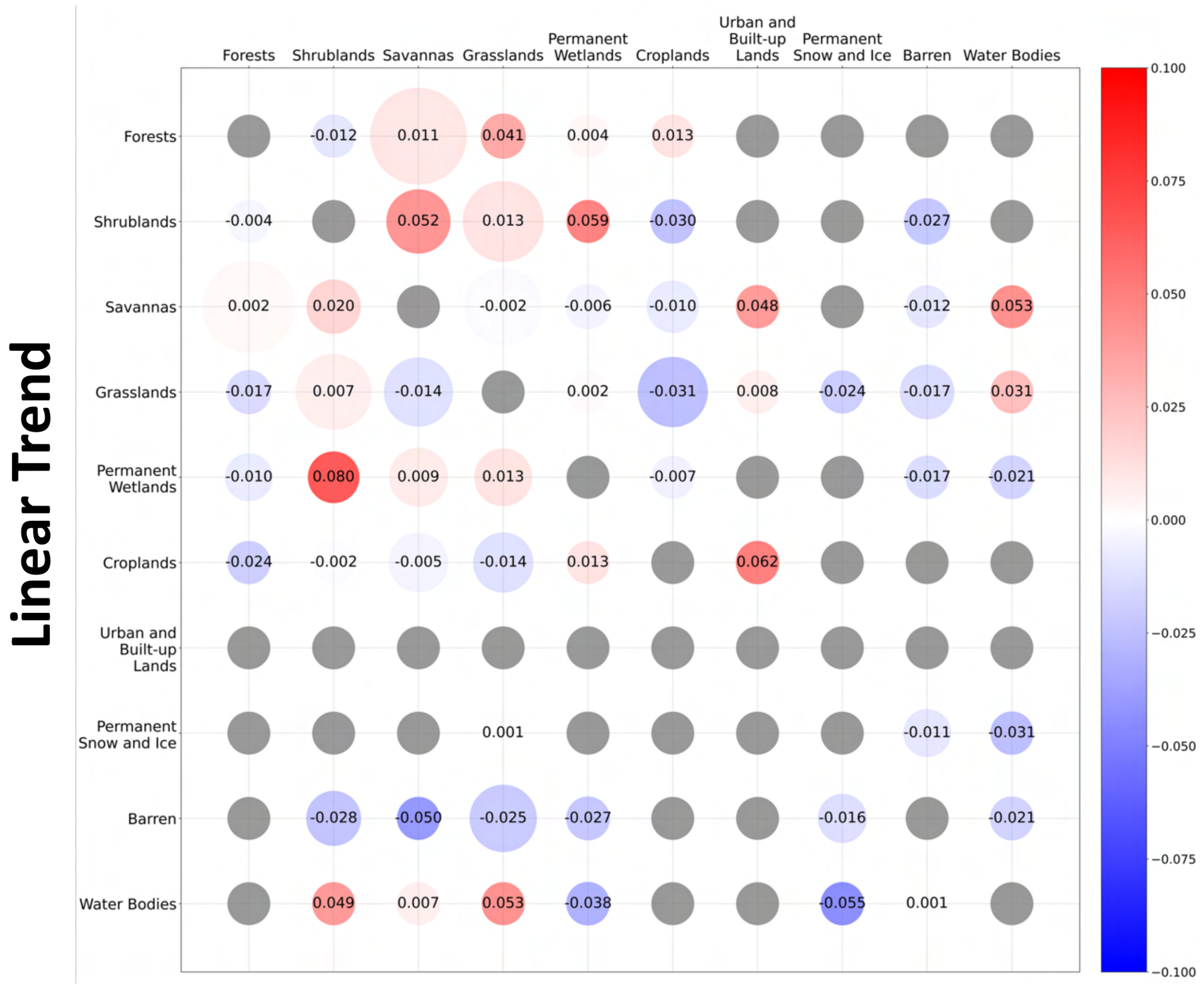

Figure 7.11: Aggregated MODIS LC type 1 - Average linear trend LST transition matrix bubble plot (Changed once 2001 to 2020).

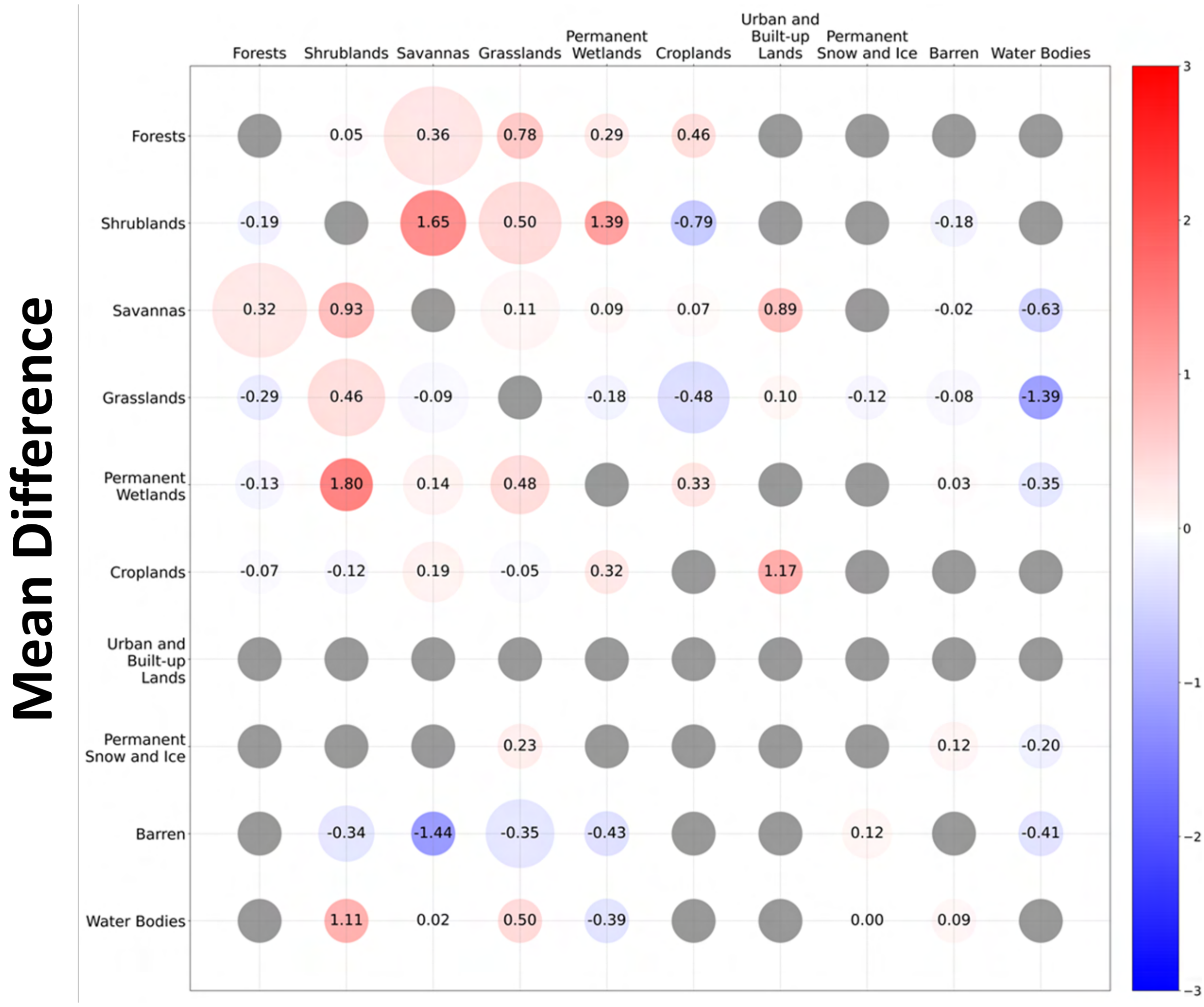

Figure 7.12: Aggregated MODIS LC type 1 - Average mean difference LST transition matrix bubble plot (Changed once 2001 to 2020).

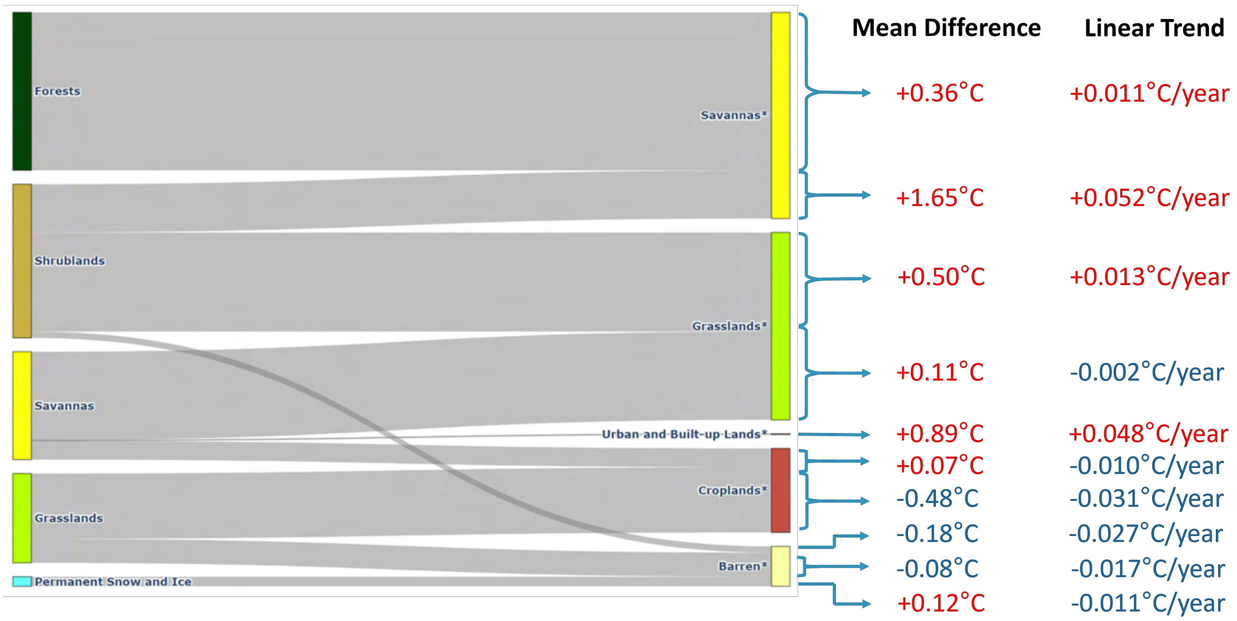

Figure 7.13: Aggregated MODIS LC type 1 and Average LST sankey diagram (Changed once 2001 to 2020).

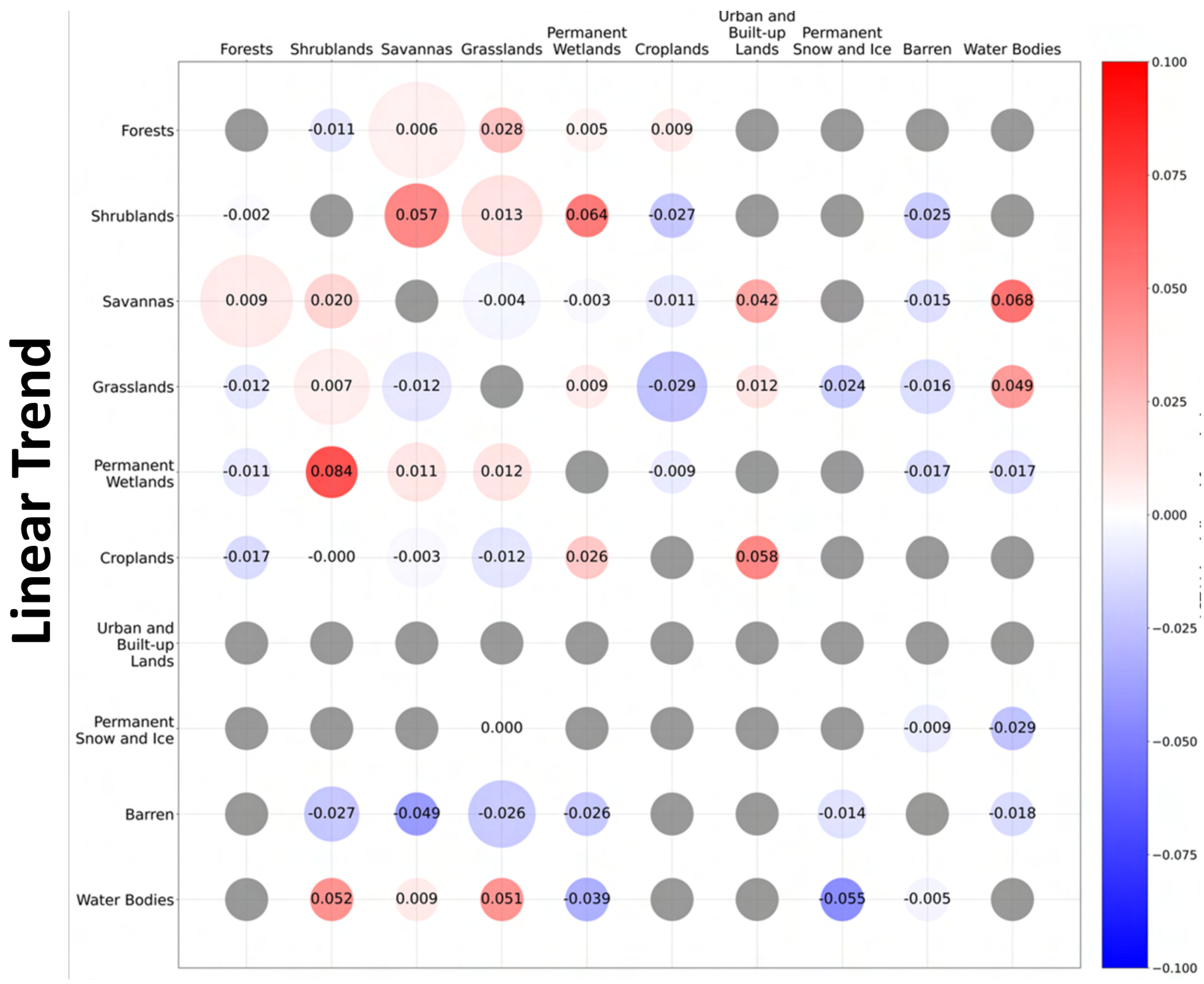

Figure 7.14: Aggregated MODIS LC type 1 - Regression equation linear trend LST transition matrix bubble plot (Changed once 2001 to 2020).

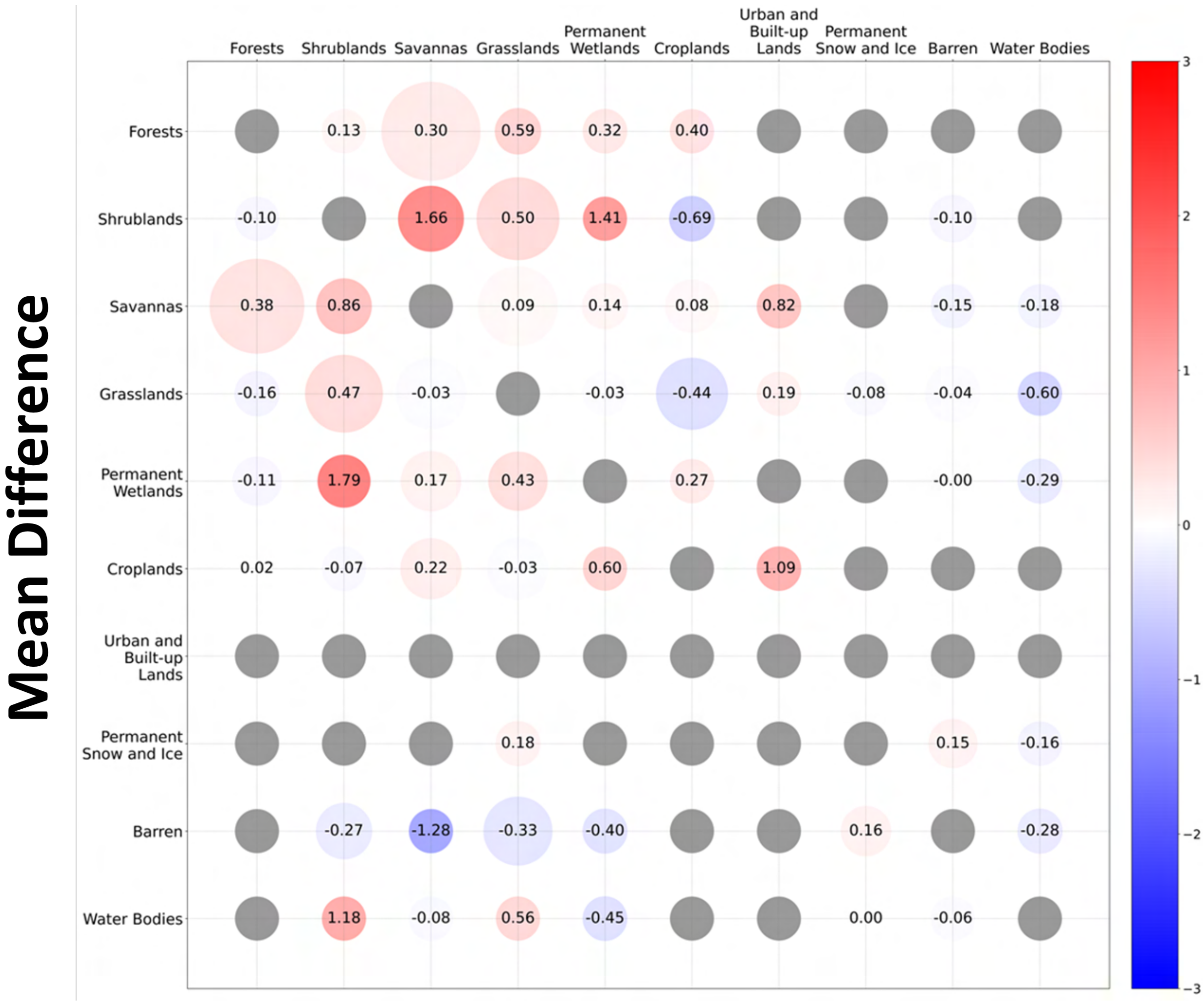

Figure 7.15: Aggregated MODIS LC type 1 - Regression equation mean difference LST transition matrix bubble plot (Changed once 2001 to 2020).

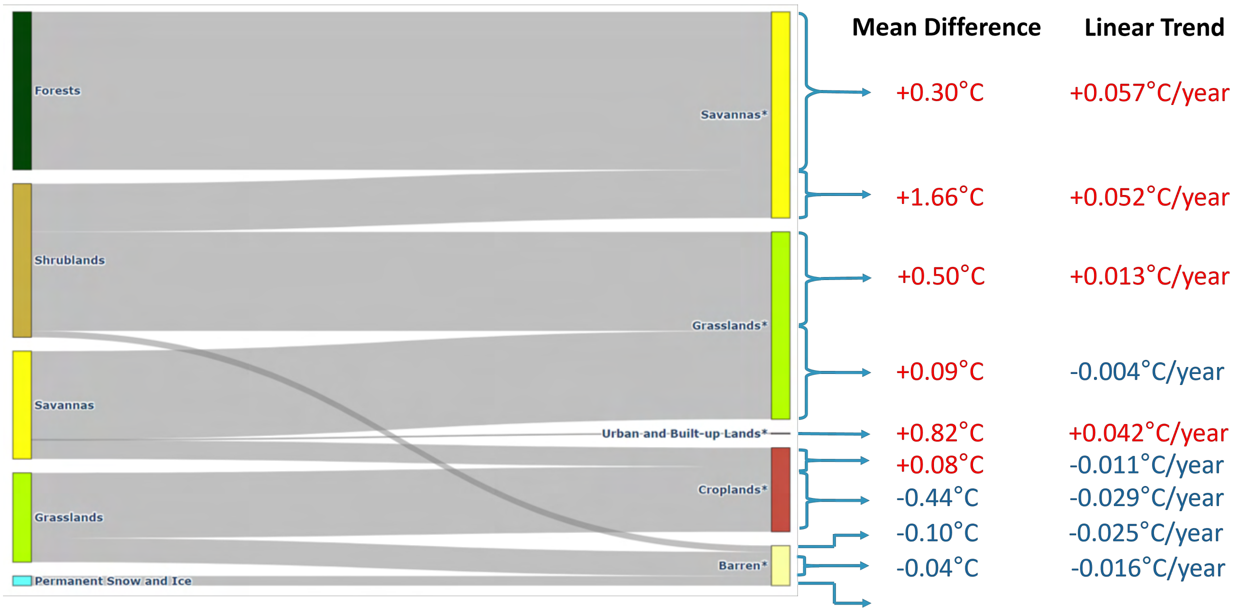

Figure 7.16: Aggregated MODIS LC type 1 and Regression equation LST sankey diagram (Changed once 2001 to 2020).

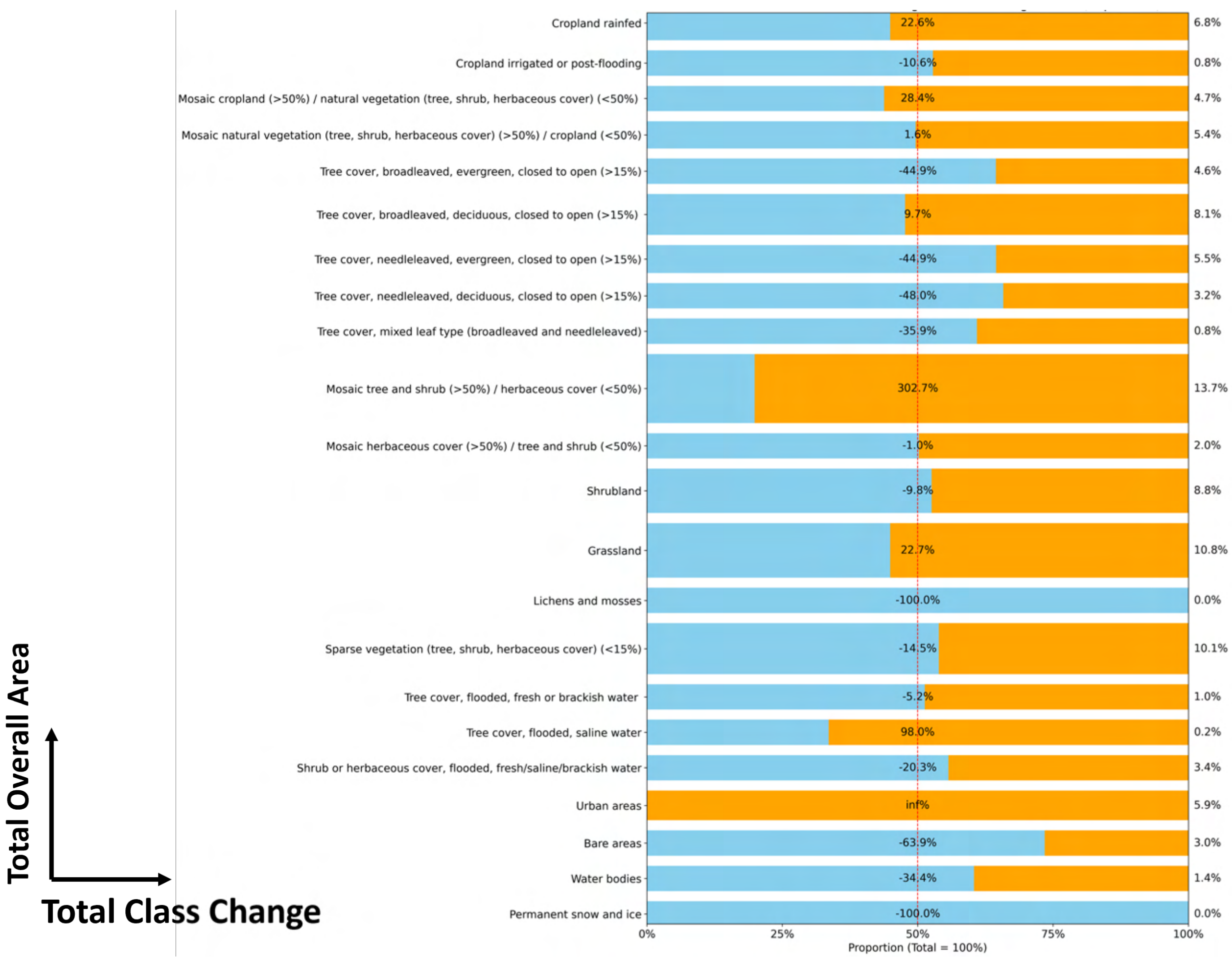

Figure 7.17: ESA CCI LC 1 global statistics (Changed once 2000 to 2020).

	Class_10	Class_20	Class_30	Class_40	Class_50	Class_60	Class_70	Class_80	Class_90	Class_100	Class_110	Class_120	Class_130	Class_140	Class_150	Class_160	Class_170	Class_180	Class_190	Class_200	Class_210	Class_220
Class_10	0	0	0	0	24986.97	66780.81	11172.06	3040.83	3750.57	34499.52	1576.8	12457.98	31906.17	0	4543.11	1952.28	1019.7	297.54	220577	3235.41	4853.25	0
Class_20	0	0	0	0	988.29	3983.94	612.72	201.87	32.76	3458.34	195.93	766.44	2750.13	0	2311.74	51.93	710.37	1.26	52352.73	684.36	1399.14	0
Class_30	0	0	0	0	106812.5	60328.26	9843.84	3910.95	6352.02	30408.39	787.77	10163.25	19054.44	0	2279.16	2454.12	1014.66	190.71	20631.96	1153.17	2045.7	0
Class_40	0	0	0	0	60544.17	139444.6	30671.64	7268.31	8469.81	69503.4	1499.04	10726.74	42461.73	0	6023.88	4132.08	1248.84	477.54	17230.86	2623.5	2198.7	0
Class_50	81698.94	1716.12	176324.6	119161.4	0	14643.9	0	89.82	0	75289.14	4123.35	72488.79	13946.67	0	3735.99	39943.08	897.93	16082.1	2047.68	165.78	11245.68	0
Class_60	88687.8	4948.65	45275.22	75419.73	14255.28	0	0	1.17	0	79208.64	8986.23	167238.6	44308.08	0	3182.31	110.25	1.89	21429.81	6599.52	1288.8	2324.07	0
Class_70	37980.54	1791.54	19701.9	30526.83	0	0	0	0	0	215382.6	20761.65	157237.1	48542.22	0	80519.04	0	0	92359.53	8968.77	18754.29	38166.21	0
Class_80	7404.57	44.82	6065.73	18766.89	129.87	3.06	0	0	0	117205.8	62669.61	154274.2	18611.64	0	14287.5	132.21	13.5	55198.53	595.08	17344.8	1683.45	0
Class_90	11398.59	253.26	3666.24	4638.87	0.36	0	0	0	0	38609.46	1669.23	14313.6	5924.34	0	2861.46	0	0	8171.28	802.17	711.09	759.51	0
Class_100	9875.97	500.04	5431.41	10881.27	17791.02	29569.05	32684.85	34897.68	4162.59	0	11202.03	40690.44	17869.95	0	8862.12	1951.74	107.28	14693.22	15760.26	1399.77	894.24	0
Class_110	11894.22	1850.49	1988.28	4933.26	2554.29	16925.22	24722.19	31418.1	1286.64	33353.91	0	1967.94	0	0	12375.09	734.67	69.03	553.95	2768.13	3969.72	337.41	0
Class_120	98009.28	4437.27	35119.98	29719.62	60143.4	202480.2	51278.94	46781.19	8373.42	133375	4006.98	0	22775.31	0	9637.74	6182.1	933.84	2057.22	22065.66	2515.5	3292.29	0
Class_130	81672.75	18465.48	35802.09	79986.6	9658.17	39761.73	21163.95	27675.9	2651.4	69294.87	0	7432.92	0	0	170006.9	1671.57	245.88	778.41	45203.49	54254.07	6966.63	0
Class_140	0	0	0	0	0	0	0	0	0	0	0	0	0	0	0	0	0	0	11.79	0	0	0
Class_150	67338.45	7524.09	18259.56	26585.01	248.13	5239.89	63956.79	63389.43	2297.16	74964.06	27797.4	5749.29	370471.4	0	0	3169.98	132.48	3350.07	7695.18	83029.77	4361.13	0
Class_160	4252.5	76.68	4722.84	4000.86	40662.81	124.47	0	117.09	0	9106.56	147.33	4670.64	1436.94	0	2639.88	0	119.7	8654.13	486.63	246.24	2867.31	0
Class_170	780.03	242.91	654.93	552.78	964.62	3.6	0	11.43	0	371.7	33.84	284.31	182.16	0	91.71	188.1	0	317.52	689.76	35.28	1428.84	0
Class_180	1685.7	23.58	406.26	1276.92	6407.01	35833.95	143151.6	21690.45	21615.39	55027.17	945.63	3833.55	2217.51	0	1835.46	13728.33	503.28	0	2913.39	205.56	10206.99	0
Class_190	0	0	0	0	0	0	0	0	0	0	0	0	0	0	0	0	0	0	0	0	0	0
Class_200	14841.99	19616.94	1873.71	3361.14	57.24	656.19	1894.32	1865.7	101.34	1889.82	4990.68	587.16	176676.5	0	371935.5	111.33	42.03	11.16	19328.49	0	8475.3	0
Class_210	5708.34	1542.96	976.77	1196.1	3187.71	2309.22	33213.51	4316.85	1002.24	2997.63	846	5658.66	6226.29	0	8066.61	3468.33	6473.16	33116.76	2651.4	34788.78	0	0
Class_220	0	0	0	0	0	0	0	0	0	0	0	0	0	0	0	0	0	0	0.72	0	0	0

Figure 7.18: ESA CCI LC 1 transition matrix (Changed once 2000 to 2020).

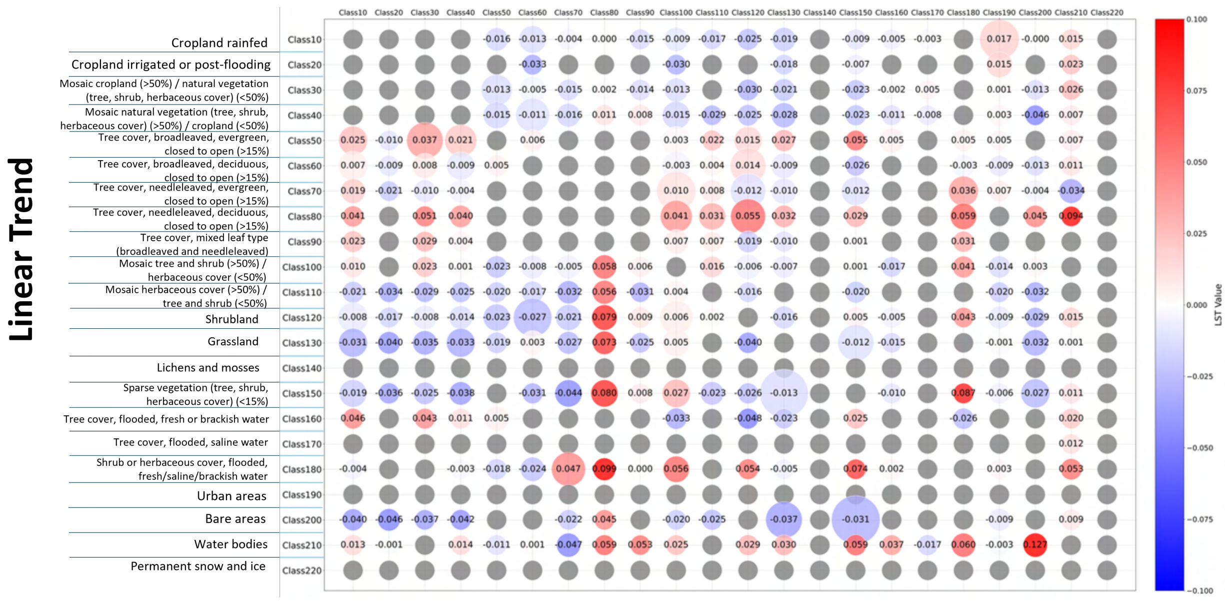

Figure 7.19: ESA CCI LC: average linear trend LST transition matrix bubble plot (Changed once 2000 to 2020).

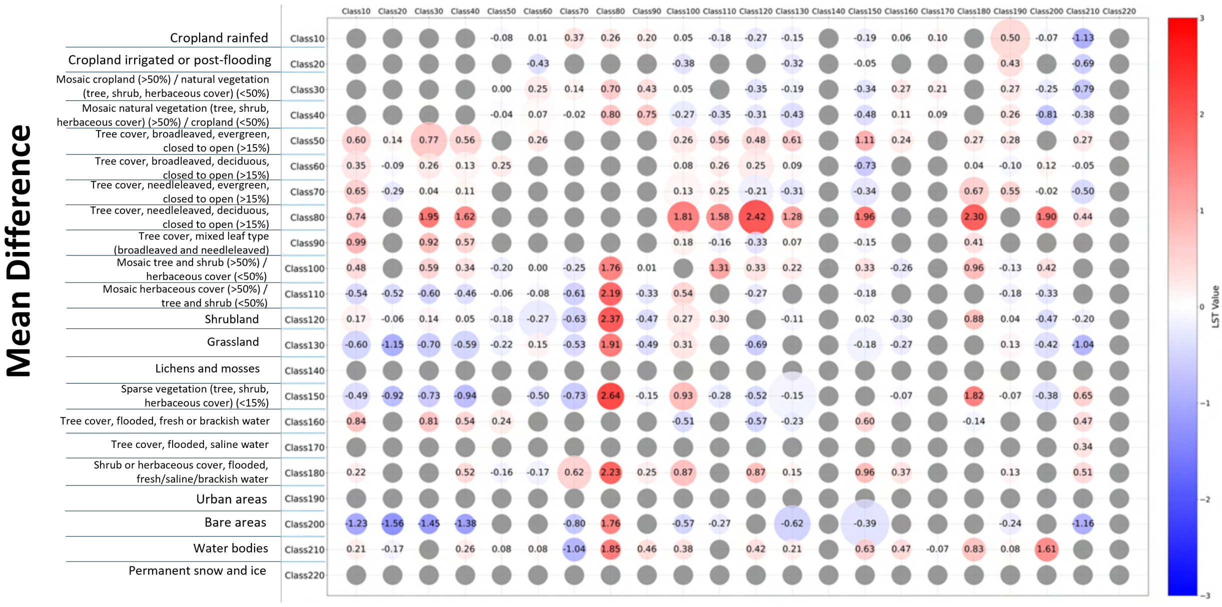

Figure 7.20: ESA CCI LC: average mean difference LST transition matrix bubble plot (Changed once 2000 to 2020).

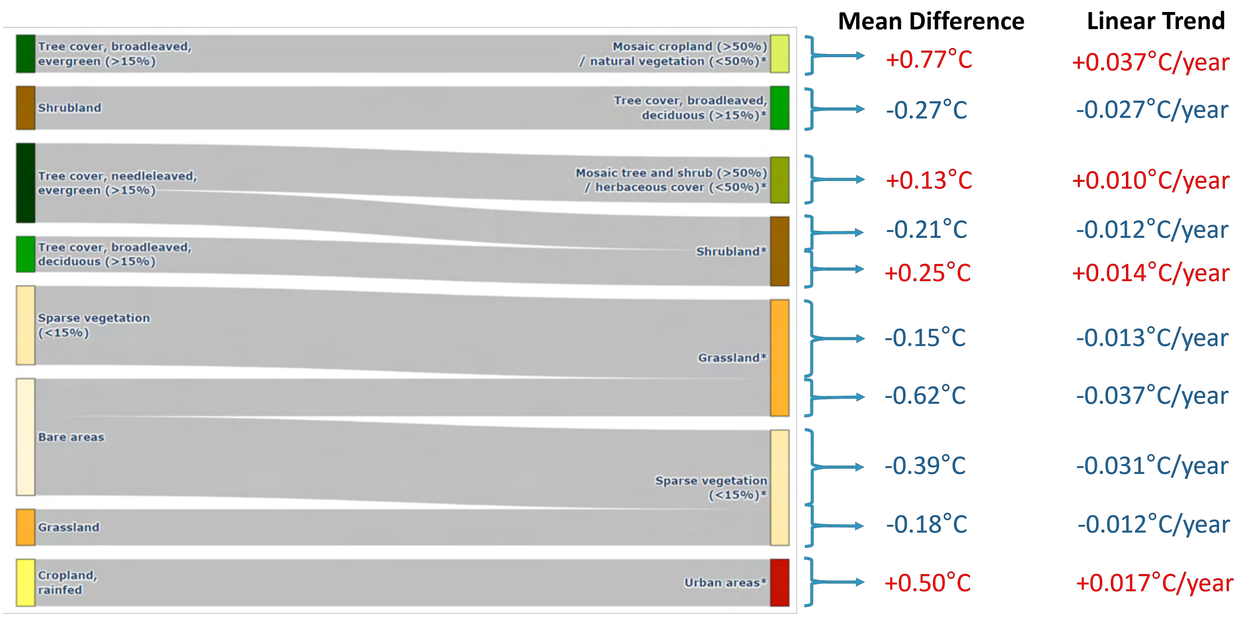

Figure 7.21: ESA CCI LC and average LST sankey diagram (Changed once 2000 to 2020).

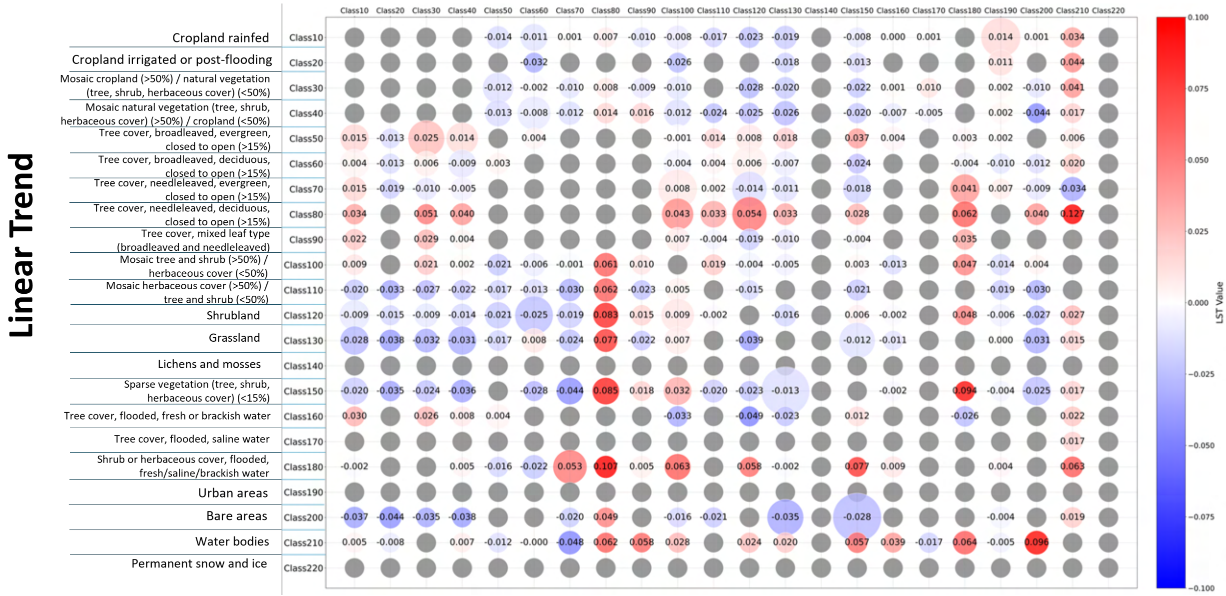

Figure 7.22: ESA CCI LC: Regression equation linear trend LST transition matrix bubble plot (Changed once 2000 to 2020).

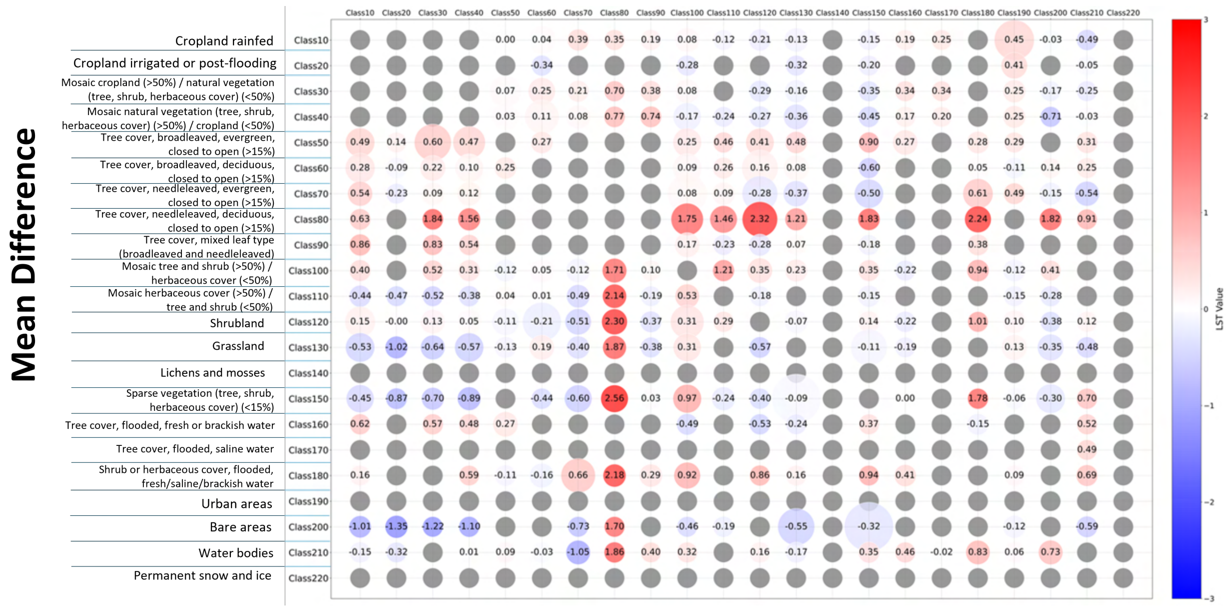

Figure 7.23: ESA CCI LC: Regression equation mean difference LST transition matrix bubble plot (Changed once 2000 to 2020).

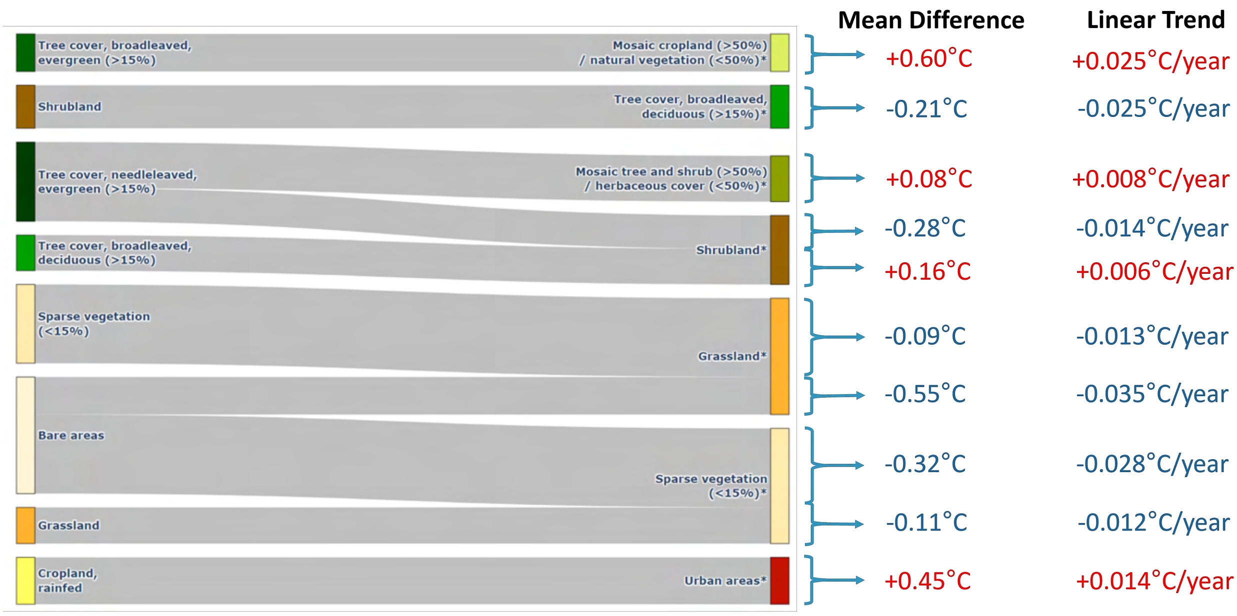

Figure 7.24: ESA CCI LC and Regression equation LST sankey diagram (Changed once 2000 to 2020).

Acknowledgements

I would like to convey my sincere gratitude to Prof. Dr. Hendrik Wulf for suggesting this project and for his invaluable guidance throughout its progression. His support in providing sample studies and scripts, particularly related to MODIS LST products, as well as his assistance in resolving errors encountered during the research, was crucial. Additionally, his insightful suggestions on how to present and visualize the study further enhanced the quality of this work.

I am equally grateful to my co-supervisors, Dr. Jennifer Susan Adams and Prof. Dr. Livia Piermattei. Dr. Adams provided expert guidance and constructive feedback on land surface temperature datasets, while Prof. Dr. Piermattei shared her extensive knowledge and feedback on land cover changes. Both supervisors significantly contributed to improving the presentation and visualization of the study, ensuring its clarity and impact.

I would also like to extend my thanks to my friend Luca Capitano for generously allowing me to use his GEE account which enabled me to simultaneously process multiple scripts which is critical to this research. Additionally, I also deeply appreciate Micaela Dassié for her guidance on administrative procedures and for sharing sample studies that informed and supported my work.

Their collective contributions and encouragement were invaluable to the success of this study, making this challenging but rewarding project an opportunity for growth and a deeper understanding of the subject matter.

Personal Declaration

I hereby declare that the submitted thesis is the result of my own, independent work. All external sources are explicitly acknowledged in the thesis.

Date
January 30, 2025

Location
Zürich

Signature
Lou Lerren Chan Curacha